Chapter 4
Surface-Enhanced Raman Spectroscopy: Principles, Substrates, and Applications

Roberto Pilot, Raffaella Signorini, and Laura Fabris

4.1 Introduction

Historically, the origin of surface-enhanced spectroscopies can be set in the early 1970s [1]. In that period, scientists were trying to measure vibrational spectra from monolayers adsorbed on substrates, due to the important contribution they would have provided to the fields of surface science, electrochemistry, and heterogeneous catalysis. Raman scattering is an intrinsically very weak phenomenon, and at that time, it seemed difficult to achieve monolayer spectra with this technique: however, in 1974, Fleischmann et al. [2] published a paper in which they reported an unexpectedly strong signal from a pyridine monolayer adsorbed on a roughened silver electrode. The authors had roughened the electrode by successive cycles of electrochemical oxidation and reduction, in order to increase the metallic surface area and hence the number of illuminated molecules. Indeed, the increased surface area was the first explanation accepted for the experimental observation by Fleischman et al. [2]. Subsequent investigations in Van Duyne's group showed however that, under some circumstances, the Raman signal increased as the surface roughness decreased. These experiments, along with other considerations, suggested that the roughness alone could not explain the unusually strong Raman signal observed. Two independent papers, published almost simultaneously in 1977, by Jeanmaire and Van Duyne [3] on one side and by Albrecht and Creighton [4] on the other side, pointed out that additional effects should have been invoked to

R. Pilot (✉) • R. Signorini
Consorzio INSTM and Department of Chemical Science, University of Padova, Via Marzolo 1, 35131 Padova, Italy
e-mail: roberto.pilot@unipd.it

L. Fabris
Department of Materials Science and Engineering, Institute for Advanced Materials Devices and Nanotechnology, Rutgers University, 607 Taylor Road, Piscataway, NJ 08854, USA

F.L. Deepak (ed.), *Metal Nanoparticles and Clusters*,
https://doi.org/10.1007/978-3-319-68053-8_4

explain Fleischman's findings: in particular the former attributed the enhancement to an increase of the electromagnetic field at the metallic surface and the latter to the formation of a charge-transfer complex between pyridine and silver. These mechanisms have been thoroughly investigated and confirmed in the following years, becoming known as "electromagnetic enhancement" and "chemical enhancement," respectively. This new phenomenon was called surface-enhanced Raman scattering (SERS). A detailed account of the whole story, told by the protagonist scientists, can be found in Ref. [1, 5].

The discovery of SERS opened up new exciting application perspectives because this spectroscopic technique simultaneously combines fingerprint recognition capabilities, typical of vibrational spectroscopies, with very high sensitivity, due to the amplification effect provided by the metallic surface.

The number of papers per year on SERS (Fig. 4.1a, black line) has increased from 50 publications in 1980 (200 in 2000) to more than 1700 in 2016, corresponding to a 30-fold increase from 1980 (eightfold from 2000). The total number of publications per year (Fig. 4.1d), instead, has risen from about 500k in 1980 (1000k in 2000) to about 2500k in 2016, corresponding to a fivefold increase from 1980 (2.5-fold from 2000): the percentage of publications on SERS has therefore significantly grown over the years, as indicated in Fig. 4.1a (red bars). It is worth mentioning that also other spectroscopies have developed their metal-enhanced counterparts, in particular fluorescence and infrared absorption. The publication trends for surface-enhanced fluorescence (SEF) [6] and surface-enhanced infrared absorption (SEIRA) [7] are shown in Fig. 4.1b, c, respectively: it is clear that they have been remarkably increasing in the last decades, although the number of publications per year on SEF and SEIRA is approximately a 20th of those on SERS. In addition, some papers have been recently published on the surface enhancement of hyper-Raman scattering (HRS) [8], coherent anti-Stokes Raman scattering (CARS) [9, 10], and second harmonic generation (SHG) [11].

In this chapter we shall focus on the most popular of the surface-enhanced spectroscopies (SERSs). Since its discovery, many aspects have been investigated and developed in the literature:

- *From a fundamental point of view*, the chemical and the electromagnetic enhancements have been extensively studied, and important advancements have been achieved [12–14], although some points are still under debate: for example, the diverse forms that can be attributed to the chemical enhancement [15, 16] or the possible relation between the near- and far-field properties of plasmonic substrates [17]. Structure-property studies have been also conducted in order to engineer the most efficient substrate morphology to amplify the Raman signal [14]; issues related to the polarization of the SERS signal have been theoretically tackled and experimentally investigated [18]. It is worth mentioning that in 1997 Nie et al. [19] reported the first claim of single-molecule detection, and since then, several papers have been published on this subject dealing with questions like the following: how to proof the detection of a single molecule? Can the orientation of the single molecule be determined from its SERS spectrum [20]?

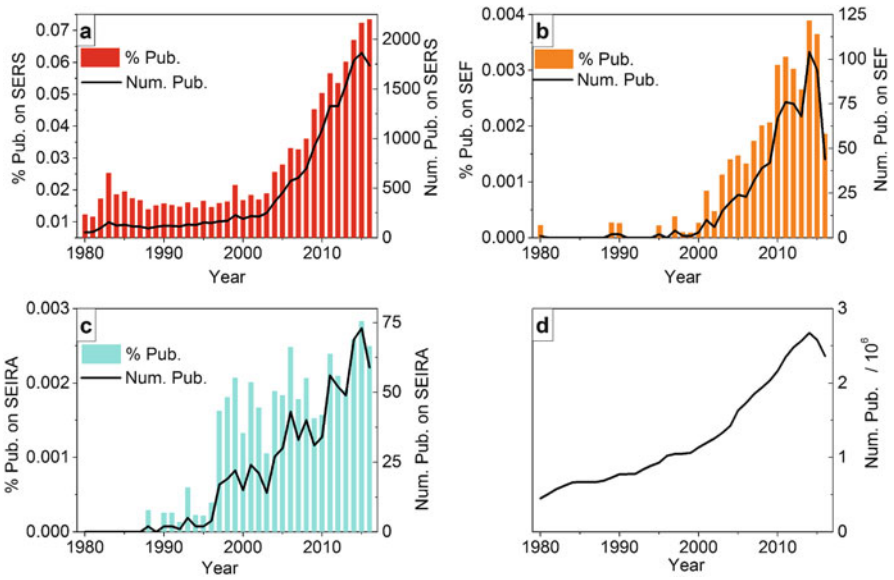

Fig. 4.1 The absolute number and the percentage of publications on SERS, SEF, and SEIRA are reported as a function of the publication year in panels (**a**, **b**, and **c**), respectively. In panel (**d**), the total number of papers published every year is represented. Bibliographic parameters were elaborated from the Scopus database. The search was limited to the period 1980–2016; all subject areas, document types, source titles, and source types were included; the language was limited to English. The papers dealing with SERS, SEF, or SEIRA were identified by selecting suitable search strings in the field "Article Title, Abstract, and Keywords." For the SERS papers, we used the search strings "surface enhanced Raman" in double quotation marks OR "SERS": the combination of these strings searches the sequence of the three words in quotation marks, ignoring punctuation (i.e., hyphens) OR the single word SERS. For SEF papers, we used the strings "surface enhanced fluorescence" OR "metal enhanced fluorescence"; an analogous search with "emission" in place of "fluorescence" did not provide a significant number of papers; the use of the acronyms MEF and SEF led to many results not related to fluorescence and therefore they were not included in the search. For SEIRA we used the strings "surface enhanced infra*red" OR "SEIRA." The total number of papers was identified by selecting the search string "English" in the field "Language." The search was done on January 1, 2017

- *Concerning the fabrication of substrates* with optimal SERS performance, a wealth of nanofabrication methods have been proposed in addition to the original electrochemical roughening: for example, assembling nanoparticles with different shapes and sizes from colloidal synthesis on 2D or 3D structures, electron beam lithography, soft lithography, or template methods [21–23]. Notice also that, in recent years, SERS substrates have become commercially available from some companies or university spin-offs.
- *SERS applications* have spread in many fields, in particular in the field of optical plasmonic sensors [24–31]. For example, SERS has been exploited in the detection of biological species [32–34], chemical warfare agents, toxic industrial chemicals [35–37], pesticides [38–41], and food additives [42] and in

the fields of art preservation [43, 44] and forensic science [45, 46]: importantly, the advancements in the engineering of the substrates, miniaturization, and sensitivity of the equipment are moving SERS toward real-life applications in several of the previously mentioned sectors [24]. Moreover, SERS has been used in spectro-electrochemical studies [47, 48], for example, to elucidate the mechanistic origin of the electro-catalytic properties of silver cathodes during the reduction of benzyl chloride [49]. Gruenke et al. [50] have recently reviewed the very promising use of ultrafast SERS to probe the temporal evolution of excited state systems [51] that are involved, for example, in plasmonically enhanced photocatalytic or photovoltaic processes.

In this book chapter, we shall provide an overview of the Raman effect (Sect. 4.2) and of the origin of the enhancement in SERS (Sect. 4.3). The subsequent sections are dedicated to specific relevant topics, in particular the distance dependence (Sect. 4.4), the definition of hot spots (Sect. 4.5), the near- vs. far-field relation (Sect. 4.6), the materials for SERS (Sect. 4.7), the methods employed for SERS substrate fabrication (Sect. 4.8), and a survey of the applications (Sect. 4.9).

4.2 Brief Introduction on Raman Scattering

When photons interact with matter, they can be scattered either elastically or inelastically. In the first case, incident and scattered photons have the same energy, and this process is often referred to as *Rayleigh scattering*. In the second case instead, the scattered photons emerge with a lower or higher frequency compared to the incident ones, because they lose or gain energy by interaction with the material: these two processes are referred to as *Stokes* and *anti-Stokes* Raman scattering, and they correspond to the interaction of a photon with a molecule in its ground or in its first vibrationally excited state, respectively [12, 52]. Figure 4.2a illustrates these processes by means of molecular energy diagrams. The scattered Raman photons therefore contain information about the vibrational modes of the molecule or material under investigation: the fingerprint provided by a Raman spectrum is specific to the material and can be used as a powerful tool for recognition or structural investigations.The Raman signal can be formally expressed with the following formula:

$$P_{\text{Raman}} = K\, N\, I\sigma_k \tag{4.1}$$

where P_{Raman} is the power read by the detector (for the k-th normal mode), N the number of illuminated molecules, I the intensity of the excitation laser, and σ_k the differential cross section of the k-th normal mode of the molecule. K is a proportionality constant: it accounts for the fraction of photons emitted by the sample that are transformed into electrons by the detector and therefore includes the quantum efficiency of the detector, the transmittance of the spectrograph and

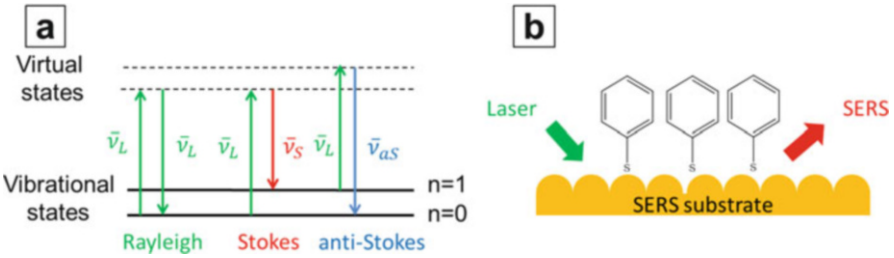

Fig. 4.2 (**a**) Illustration of scattering processes by means of energy diagrams. Horizontal *solid lines* represent the energy levels of a molecule, that is, its ground state ($n = 0$) and its first vibrationally excited state ($n = 1$). The *dashed lines* represent the virtual levels of the molecule. *Upward* and *downward arrows* represent an incident and a scattered photon, respectively. Incident and scattered photons at the laser wavenumber ($\overline{\nu}_L$) are depicted in *green*; scattered photons at the *Stokes* ($\overline{\nu}_S$) and *anti-Stokes* ($\overline{\nu}_{\mathrm{aS}}$) absolute wavenumbers are depicted in *red* and *blue*, respectively. The Raman shift wavenumber of the normal mode k, $\overline{\nu}_k$ is defined as $\overline{\nu}_k = \overline{\nu}_L - \overline{\nu}_S = \overline{\nu}_{\mathrm{aS}} - \overline{\nu}_L$. (**b**) Illustration of the SERS effect: Raman scattering, intrinsically weak, is strongly amplified if the molecules are placed at the surface of a suitably nanostructured metallic substrate

of the collection optics, the collection geometry, and the numerical aperture of the objective.

It is important to notice that scattering occurs with very low efficiency if compared to fluorescence. The fluorescence cross sections typically amount to $\sim 10^{-16}$ cm^2/molecule [12]; the *Rayleigh* and *Stokes* Raman cross sections, on the other hand, are typically around $\sim 10^{-26}$ cm^2/molecule and $\sim 10^{-29}$ cm^2/molecule, respectively [12, 25, 53]. *Stokes* Raman cross sections can reach $\sim 10^{-22}$ cm^2/molecule if the excitation source is resonant with a permitted electronic transition of the molecule [12, 25]. *Anti-Stokes* cross sections (σ_k^{aS}) are remarkably smaller than the *Stokes* ones (σ_k^S) at room temperature as it can be easily inferred from the expression that defines their ratio for the vibrational mode k: $\rho_k^{\mathrm{aS}/S} = \left(\sigma_k^{\mathrm{aS}}/\sigma_k^S\right) = \left(\overline{\nu}_{\mathrm{aS}}/\overline{\nu}_S\right)^4 e^{-(hc\overline{\nu}_k/k_BT)}$, where $\overline{\nu}_{\mathrm{aS}} = \overline{\nu}_L + \overline{\nu}_k$ and $\overline{\nu}_S = \overline{\nu}_L - \overline{\nu}_k$ are *anti-Stokes* and *Stokes* photon absolute wavenumbers, $\overline{\nu}_L$ the excitation laser wavenumber, $\overline{\nu}_k$ the Raman shift wavenumber of the normal mode k, k_B the Boltzmann constant, and T the temperature [12, 52]. At room temperature, for $\overline{\nu}_L \sim 20000$ cm^{-1} (514 nm) and $\overline{\nu}_k = 1000$ cm^{-1},$\rho_k^{\mathrm{aS}/S}$ amounts to about $\sim 10^{-2}$. Due to the remarkable difference in cross sections, only the *Stokes* Raman bands are normally detected and reported in Raman spectra. Typical values of the total (integrated over the whole solid angle of emission) cross sections for different optical processes are summarized in Table 4.1. For the interested readers, the theory of Raman scattering is extensively reported in the book by Long [52] that covers all theoretical aspects of this technique. More practical aspects, related to the instrumentation, can be found in the book by McCreery [54].

The intrinsic low efficiency of Raman scattering can be strongly improved if molecules are placed close to suitably (normally metallic) nanostructured surfaces, in which a plasmonic resonance can be excited: in this case, we talk about surface-

Table 4.1 Typical values of total cross sections for different optical processes

Process	Cross section (cm^2/molecule)	References
Fluorescence	10^{-16}	[12]
Rayleigh scattering	10^{-26}	[53]
Stokes Raman scattering	10^{-29}	[12, 25, 53]
Resonant *Stokes* Raman scattering	10^{-22}	[25]

enhanced Raman scattering (SERS) (Fig. 4.2b). Notice that, despite the much lower cross section of Raman compared to fluorescence, the enhancement achievable in the former ($\sim 10^8$) is much higher than the one achievable in the latter ($\sim 10^3$) [6]. The SERS signal can be expressed as:

$$P_{\mathrm{SERS}} = G_{\mathrm{SERS}}\, P_{\mathrm{Raman}} \tag{4.2}$$

G_{SERS} is called SERS enhancement factor and accounts for the observed increase of signal, due to the presence of the nanostructures: its origin will be described in the next sections. Concerning the phenomenon of plasmonic resonance and the ability of nanostructured materials to localize and intensify light at their surface, we refer the interested readers to some of the many books, reviews, or papers on this subject [12, 31, 55–59].

4.3 Enhancement Mechanisms in SERS

The Raman signal of a molecule on a plasmonic substrate can be enhanced by two different mechanisms: the electromagnetic and the chemical one. The total SERS enhancement (G_{SERS}) can be expressed as the product of the electromagnetic ($G^{\mathrm{Em}}_{\mathrm{SERS}}$) and the chemical ($G^{\mathrm{Chem}}_{\mathrm{SERS}}$) contributions as follows:

$$G_{\mathrm{SERS}} = G^{\mathrm{Em}}_{\mathrm{SERS}} \cdot G^{\mathrm{Chem}}_{\mathrm{SERS}} \tag{4.3}$$

In the following, the origin and the main features of the two contributions are discussed.

4.3.1 Electromagnetic Enhancement

The electromagnetic enhancement comprises two conceptually different steps [12, 60]:

- *Local field enhancement* (or near-field enhancement). The electromagnetic field experienced by the molecule is stronger than the laser field, due to the excitation of surface plasmon resonances in the substrate.
- *Radiation enhancement*. The Raman power radiated by the molecule depends on the environment in which it is embedded: a molecule located in an inhomogeneous environment (like the surface of a metallic substrate that is characterized by the presence of interfaces between different materials) radiates a different amount of energy compared to the same molecule in vacuum or in an homogenous environment.

The theory of electromagnetic enhancement in SERS has been put on firm base and extensively described in the book by Le Ru and Etchegoin [12]; moreover, some aspects, related in particular to the radiation enhancement, are presented in detail in the book by Novotny and Hecht [60]. In the next sections, our aim is to provide a simple picture of the SERS enhancement, on the basis of the theories presented in Ref. [12, 60].

4.3.1.1 Local Field Enhancement

In the classic phenomenological picture, the Raman emission from a molecule excited by a laser can be described by the following expression [12, 52]:

$$\boldsymbol{p}\left(\omega_R\right) = \widehat{\alpha}_R\left(\omega_R, \omega_L\right)\boldsymbol{E}\left(\omega_L\right) \tag{4.4}$$

$\boldsymbol{E}(\omega_L)$ is the electric field of the laser, oscillating at frequency ω_L, $\widehat{\alpha}_R$ is the Raman polarizability tensor of the molecule, and $\boldsymbol{p}(\omega_R)$ is the induced dipole, oscillating at the Raman frequency ω_R. The polarizability is a second-rank tensor that determines the direction and the modulus of $\boldsymbol{p}(\omega_R)$, as a function of $\boldsymbol{E}(\omega_L)$. From the classical theories, it is known that the power radiated by a dipole in vacuum, integrated over all emission directions, (P) is proportional to the square modulus of the dipole itself through the formula [12]:

$$P = \frac{\omega_R^4}{12\pi\varepsilon_0 c^3}\left|\boldsymbol{p}\left(\omega_R\right)\right|^2 = \frac{\omega_R^4}{12\pi\varepsilon_0 c^3}\left|\widehat{\alpha}_R\left(\omega_R, \omega_L\right)\boldsymbol{E}\left(\omega_L\right)\right|^2 \tag{4.5}$$

where ε_0 is the dielectric constant in vacuum and c the speed of light in vacuum. If the molecule is placed near a metallic nanostructure, the local electric field experienced by the molecule ($\boldsymbol{E}_{\mathrm{Loc}}(\omega_L)$) is in general significantly different from the incident one ($\boldsymbol{E}(\omega_L)$), both in terms of intensity and in terms of polarization [55]. Replacing $\boldsymbol{E}(\omega_L)$ with $\boldsymbol{E}_{\mathrm{Loc}}(\omega_L)$ in Eq. (4.5) leads to a modification of the radiated power. The enhancement of the radiated power, due to a stronger excitation of the molecule, is represented by the factor M_{Loc}^Z, as expressed in Eq. (4.6) [12]:

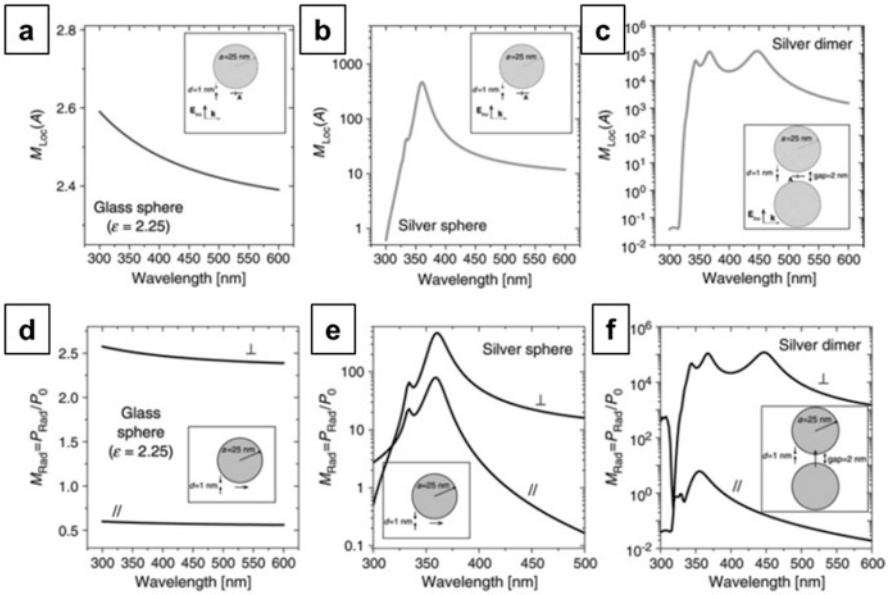

Fig. 4.3 Spectral dependence of the local field enhancement, $M^Z_{\mathrm{Loc}}(\omega_L)$, for a glass sphere (**a**), an Ag sphere (**b**), and a dimer formed by two identical Ag spheres (**c**). $M^Z_{\mathrm{Loc}}(\omega_L)$ is calculated at point A, lying at 1 nm distance from the surface of the single spheres and in the middle of the 2 nm gap of the dimer. The spectral dependence of the radiation enhancement, M_{Rad}, is calculated for a glass sphere (**d**), a Ag sphere (**e**), and a dimer formed by two identical Ag spheres (**f**): M_{Rad} was calculated for a dipole parallel and perpendicular to the surface (Reproduced with permission from Ref. [12])

$$M^Z_{\mathrm{Loc}}(\omega_L) = \frac{|\boldsymbol{E}_{\mathbf{Loc}}(\omega_L)|^2}{|\boldsymbol{E}(\omega_L)|^2} = \left|\widetilde{\boldsymbol{E}}^Z_{\mathrm{Loc}}(\omega_L)\right|^2 \tag{4.6}$$

A unit-less vector, $\widetilde{\boldsymbol{E}}^Z_{\mathrm{Loc}}(\omega_L)$, whose direction and magnitude correspond to the polarization direction and to the enhancement of the local field, respectively, is also introduced. The superscript Z pinpoints the (linear) polarization of the laser that generates the local field.

As an example, we show in Fig. 4.3 the spectral dependence of $M^Z_{\mathrm{Loc}}(\omega_L)$ for two isolated spheres made of glass (a) and silver (b) and for a dimer formed by two identical silver spheres separated by a 2 nm gap (c) [12]. All spheres have a radius of 25 nm. $M^Z_{\mathrm{Loc}}(\omega_L)$ is calculated at 1 nm from the surface, at point A, for all systems considered. Looking at Fig. 4.3, one can notice that the enhancement of the glass sphere is characterized by a small absolute value and a weak spectral dependence; conversely, the silver nanosphere shows much higher values of enhancement and a strong spectral variation. Even higher absolute values of enhancement occur for the dimer.

4.3.1.2 The Radiation Enhancement

The second step of the electromagnetic enhancement process regards the fact that the spontaneous decay rate of an atom or a molecule is not an intrinsic property of the emitting object but also depends on the environment in which it is embedded [60, 61]. This phenomenon was first pointed out by Purcell in 1946 [62], who suggested that the nuclear magnetic transition rates could be modified by placing atoms in cavities. Experimental observations of the environment dependence of the spontaneous emission rate have been provided in several studies. For example, Drexhage et al. reported on the dependence of the emission rate of Eu^{3+} complexes as a function of the distance from a mirror surface [63–65]; Goy et al. investigated the enhancement of the decay rate of sodium Rydberg atoms in a cavity [66]; and Andrew et al. demonstrated that the Förster (non-radiative) energy transfer rate between an Eu^{3+} complex (donor) and an indodicarbocyanine dye (acceptor) depends on the microcavity structure in which they are placed [67].

Spontaneous emission is a quantum mechanical phenomenon that, to be explained, requires a quantized treatment of the matter and of the electromagnetic fields [60]. However, the same phenomenon can be described within a completely classical framework: the equivalence between the classical and the quantum electrodynamics approach and the limits in which it is valid are discussed in Chap. 8 of Ref. [60] and Chap. 4 of Ref. [12]. In the following, we shall use the classical approach to derive the origin of the radiation enhancement. Let's consider a molecule in vacuum that, after the excitation source (the laser) has been turned off, relaxes to the ground state emitting radiation: in the classical picture, this situation can be represented by an undriven harmonically oscillating dipole [60]:

$$\frac{d^2}{dt^2}\boldsymbol{p}(t) + \gamma_0 \frac{d}{dt}\boldsymbol{p}(t) + \omega_0^2 \boldsymbol{p}(t) = 0 \tag{4.7}$$

where $\boldsymbol{p}(t)$ is the molecular dipole moment, ω_0 its natural oscillation frequency, and γ_0 the damping factor. The damping factor originates from the fact that oscillating charges (i.e., the dipole) must emit radiation according to the relation:

$$P(t) = \frac{1}{4\pi\varepsilon_0}\frac{2}{3c^3}\left[\frac{d^2\ |\boldsymbol{p}(t)|}{d\ t^2}\right]^2 \tag{4.8}$$

and hence after some time, the dipole has to come to rest. If the molecule is embedded in an inhomogeneous environment, like the interface between a metallic substrate and a solution (or air), the dipole experiences as a driving force its own emission, which is scattered back by the interfaces surrounding the molecule. In order to account for this effect, Eq. (4.7) has to be modified as:

$$\frac{d^2}{dt^2}\boldsymbol{p}(t) + \gamma_0 \frac{d}{dt}\boldsymbol{p}(t) + \omega_0^2 \boldsymbol{p}(t) = \frac{q^2}{m}\boldsymbol{E}_{\mathrm{SR}}(t) \tag{4.9}$$

where $\boldsymbol{E}_{\mathrm{SR}}(t)$ is the self-reaction field (also called secondary field) and q and m are the electric charge and the mass of the charges that form the dipole. The solutions of this equation are:

$$\boldsymbol{p}(t) = \mathrm{Re}\left\{\boldsymbol{p}_0 e^{-i\omega t} e^{-\gamma t/2}\right\} \qquad \boldsymbol{E}_{\mathrm{SR}}(t) = \mathrm{Re}\left\{\boldsymbol{E}_{\mathrm{SR}-0} e^{-i\omega t} e^{-\gamma t/2}\right\} \tag{4.10}$$

Notice that the dipole and the self-reaction field possess a frequency ω and a damping constant γ different from the natural ones. It can be shown that the ratio between the power radiated by the dipole in vacuum, P_0, and in the inhomogeneous environment, P, can be expressed as [60]:

$$M_{\mathrm{Rad}} = \frac{P}{P_0} = 1 + \frac{6\pi\varepsilon_0}{|\boldsymbol{p}_0|^2}\frac{1}{k^3}\mathrm{Im}\left\{\boldsymbol{p}_0^* \cdot \boldsymbol{E}_{\mathrm{SR}-0}\right\} \tag{4.11}$$

where k is the wavevector of the emitted radiation.

This equation shows that the power radiated by a dipole in an inhomogeneous environment depends on the self-reaction field and hence on the objects surrounding the dipole itself. In vacuum, no self-reaction field would be present and therefore $P = P_0$.

In Fig. 4.3d–f, the enhancement of the radiated power, $M_{\mathrm{Rad}} = \frac{P}{P_0}$, is shown for the same systems for which $M^Z_{\mathrm{Loc}}(\omega_L)$ was calculated in Fig. 4.3a–c [12]: in this case, M_{Rad} is simulated for a dipole oriented parallel and perpendicular to the surface. It is worth highlighting that the radiation enhancement exhibits a spectral dependence that is very similar to the local field enhancement despite the very diverse physical origin of the two phenomena and that the radiation enhancement depends on the orientation of the emitting dipole.

4.3.1.3 Similarities Between Local Field and Radiation Enhancement

A question that spontaneously arises is why the local field enhancement and the radiation enhancement, which originate from two physically different phenomena, show a similar spectral dependence, as clearly evidenced in Fig. 4.3. This similarity is at the base of the widely employed $|E|^4$ approximation, used to express and measure the SERS enhancement factors.

Intuition suggests that $\boldsymbol{E}_{\mathrm{SR}}$ is somehow related to $\boldsymbol{E}_{\mathrm{Loc}}(\omega_L)$. If one considers the typical SERS case in which a molecule is located near a plasmonic substrate, $\boldsymbol{E}_{\mathrm{Loc}}(\omega_L)$ is the field at the molecule position generated by the excitation laser; $\boldsymbol{E}_{\mathrm{SR}}$ is the field at the molecule position generated by the molecule itself, due to the fact that its emission is scattered back by the adjacent interfaces. Clearly $\boldsymbol{E}_{\mathrm{Loc}}(\omega_L)$ and $\boldsymbol{E}_{\mathrm{SR}}$ are not identical: in the first case, the excitation is provided by the laser that can be approximated by a plane wave or a focused plane wave, and in the second case, the excitation is provided by a dipolar-like source residing very close to the plasmonic substrate. Moreover, $\boldsymbol{E}_{\mathrm{Loc}}(\omega_L)$ is the total field at the molecule position;

$\boldsymbol{E}_{SR}$ instead is only the self-reaction (secondary) field. Nevertheless, a qualitative analogy between the local field enhancement and the radiation enhancement can be glimpsed from these simple considerations.

In order to figure out more precisely the similarities between the two phenomena, one may resort to the optical reciprocity theorem (ORT) [12], which allows one to calculate the far-field emission of a dipole, in a defined direction, from the solution of two plane wave excitations, one for each possible detection polarization. Let's consider the following quantities:

- A dipole $\boldsymbol{p}$ located at point S on a metallic surface (sample position) and the electric field $\boldsymbol{E}$ it produces at point D (detector position): $\boldsymbol{p}$ represents the Raman emitter, and $\boldsymbol{E}$ is the electric field it generates at the detector position. Once $\boldsymbol{E}$ is known, the intensity (and hence the power) radiated by the molecule at the detector can be calculated as $I = 1/2\varepsilon_0 c|\boldsymbol{E}|^2$ [60].
- A dummy dipole $\boldsymbol{p}_2$ located at point D (detector) and the electric field $\boldsymbol{E}_2$ it generates at point S (sample).

Although the problem can be treated in a general way, for simplicity, we have restricted it to a backscattering configuration, in which the emissions by the real dipole $\boldsymbol{p}$ and by the dummy dipole $\boldsymbol{p}_2$ occur along the same line but with opposite directions. This is representative of the most commonly adopted experimental configuration, in which the laser excitation and the signal collection are both accomplished through the same microscope objective. The geometrical arrangement is shown in Fig. 4.4. The ORT states that [12]:

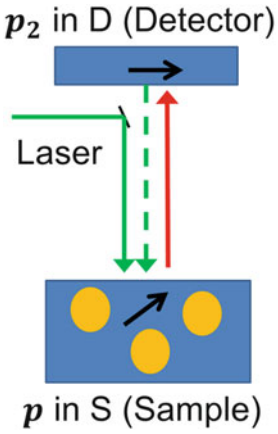

Fig. 4.4 Arrangement of the dipoles in the optical reciprocity theorem (ORT): the Raman emitter $\boldsymbol{p}$ is placed at the sample position (S), surrounded by metallic objects representing the SERS substrate. The dummy dipole $\boldsymbol{p}_2$ is placed at the detector position (D). The emission from the dummy dipole is represented by the *green dashed arrow*; the emission from the Raman emitter occurs along the same line but in opposite direction and is represented by the *solid red arrow*. In the (*backscattering*) experiment, the sample is illuminated by the laser, represented by the *solid green arrow*, and the collection of the Raman signal takes place along the *red arrow*

$$\boldsymbol{p}_2 \cdot \boldsymbol{E} = \boldsymbol{p} \cdot \boldsymbol{E}_2 \tag{4.12}$$

The problem that one wants to solve in SERS is calculating the value of $\boldsymbol{E}$ at the detector, given $\boldsymbol{p}$. It can be shown that:

$$E_{P1} \propto \boldsymbol{p} \cdot \widetilde{\boldsymbol{E}}_{\mathrm{Loc}}^{\mathrm{PW}-P1} \tag{4.13}$$

where $\widetilde{\boldsymbol{E}}_{\mathrm{Loc}}^{\mathrm{PW}-P1}$ is a unit-less vector indicating the polarization direction of the local field generated by $\boldsymbol{p}_2$ at the molecule position; its magnitude is the enhancement of the local field due to the presence of the metallic surface, compared to field that the molecule would experience in vacuum. The superscript PW underlines the fact that, far from the origin, the emission from $\boldsymbol{p}_2$ is treated as a plane wave (PW), polarized along the direction $P1$. E_{P1} is the $P1$ polarized component of $\boldsymbol{E}$. $P1$ hence identifies both the polarization of the radiation emitted by the dipole $\boldsymbol{p}_2$ and the polarization component of the field $\boldsymbol{E}$ generated by $\boldsymbol{p}$ at the detector. The power radiated by the molecule can then be worked out from Eq. (4.13), by summing up the components of $\boldsymbol{E}$ along two perpendicular directions, $P1$ and $P2$:

$$\frac{dP}{d\Omega}(\Omega) = \frac{\omega^4}{32\pi^2\varepsilon_0 c^3}\left|\boldsymbol{p}(\omega_R)\right|^2\left[\left|\boldsymbol{e}_p \cdot \widetilde{\boldsymbol{E}}_{\mathrm{Loc}}^{\mathrm{PW}-P1}(\omega_R)\right|^2 + \left|\boldsymbol{e}_p \cdot \widetilde{\boldsymbol{E}}_{\mathrm{Loc}}^{\mathrm{PW}-P2}(\omega_R)\right|^2\right] \tag{4.14}$$

where Ω is the collection solid angle and $\frac{dP}{d\Omega}$ is the differential radiated power along a direction defined by Ω that in our backscattering hypothesis corresponds to the line joining $\boldsymbol{p}$ and $\boldsymbol{p}_2$. $\boldsymbol{e}_p$ is a versor that defines the direction of $\boldsymbol{p}(\omega_R)$ through the relation $\boldsymbol{p}(\omega_R) = |\boldsymbol{p}(\boldsymbol{\omega_R})|\boldsymbol{e}_p$. Notice that while Eq. (4.5) gives the power radiated by a dipole integrated over all possible directions, Eq. (4.14) instead expresses the radiated power along a specific direction defined by Ω. This equation shows that the power emitted from the molecule $\boldsymbol{p}$ can be expressed as a function of the local field generated at the molecule position by a dummy dipole. However, far from the position at which $\boldsymbol{p}_2$ is located, the dipole emission can well be approximated by a plane wave: the "virtual illumination" provided by the dummy dipole will generate a local field enhancement at the molecule position equivalent to the one generated by a laser polarized along $P1$ with frequency ω_R. The enhancement factor for the radiation part can be expresses as:

$$M_{\mathrm{Loc}}^{P}(\omega_R) = \left|\widetilde{\boldsymbol{E}}_{\mathrm{Loc}}^{\mathrm{PW}-P}(\omega_R)\right|^2 \tag{4.15}$$

The superscript PW, which distinguishes the local field generated by the dummy dipole from the local field generated by the laser, is not specified in the expression of $M_{\mathrm{Loc}}^{P}(\omega_R)$, by virtue of previous considerations; the symbol P, which specifies the polarization of the radiation that generates the local field, is however retained. Therefore, the ORT allowed us to describe the radiation enhancement by making

use of the local field enhancement calculated at the Raman frequency and for two perpendicular excitation polarizations.

4.3.1.4 Derivation of SERS Enhancement Factor for a Single Molecule

By combining the local field and the radiation enhancements, an expression for the single-molecule SERS enhancement factor (G_{SM}), in backscattering configuration, can be worked out [12]:

$$G_{\mathrm{SM}} = G_{\mathrm{SM}}^{\parallel} + G_{\mathrm{SM}}^{\perp} = M_{\mathrm{Loc}}^{Z}(\omega_L)\, M_{\mathrm{Loc}}^{Z}(\omega_R)\, T^{\parallel} + M_{\mathrm{Loc}}^{Z}(\omega_L)\, M_{\mathrm{Loc}}^{Y}(\omega_R)\, T^{\perp} \tag{4.16}$$

G_{SM} is the sum of a parallel $\left(G_{\mathrm{SM}}^{\parallel}\right)$ and a perpendicular contribution $\left(G_{\mathrm{SM}}^{\perp}\right)$: in the parallel contribution, the detected Raman scattering is polarized along Z, as the excitation laser, and in the perpendicular contribution it is polarized along Y; the laser propagates along X. For consistency with the notation in Eq. (4.3), the single-molecule electromagnetic SERS enhancement factor and its parallel and perpendicular components should be written as $G_{\mathrm{SERS-SM}}^{\mathrm{Em}}$, $G_{SERS-\mathrm{SM}}^{\mathrm{Em}-\parallel}$, and $G_{\mathrm{SERS-SM}}^{\mathrm{Em}-\perp}$: for simplicity, however, we shall use the symbols of Eq. (4.16) for the remaining part of Sect. 4.3. The parameter T is the so-called surface selection rule factor and possesses a parallel and a perpendicular component as well:

$$T^{\parallel} = e_R^Z \cdot \widehat{\alpha}_N \cdot e_L^Z \qquad\qquad T^{\perp} = e_R^Y \cdot \widehat{\alpha}_N \cdot e_L^Z \tag{4.17}$$

$\widehat{\alpha}_N$ is the normalized Raman polarizability tensor and differs from $\widehat{\alpha}_R(\omega_R, \omega_L)$ in Eq. (4.4) for a suitable normalization constant that makes it dimensionless, retaining the symmetry properties of the tensor. Its precise definition, not necessary for our discussion, can be found in Ref. [12]. The local field enhancement factors in Eq. (4.16) are summarized in the following for clarity:

$$M_{\mathrm{Loc}}^{Z}(\omega_L) = \left|\widetilde{\boldsymbol{E}}_{\mathrm{Loc}}^{Z}(\omega_L)\right|^2 = \left|\widetilde{E}_{\mathrm{Loc}}^{Z}(\omega_L)\, \boldsymbol{e}_L^Z\right|^2 \tag{4.18}$$

$$M_{\mathrm{Loc}}^{Z}(\omega_R) = \left|\widetilde{\boldsymbol{E}}_{\mathrm{Loc}}^{\mathrm{PW}-Z}(\omega_R)\right|^2 = \left|\widetilde{E}_{\mathrm{Loc}}^{\mathrm{PW}-Z}(\omega_R)\, \boldsymbol{e}_R^Z\right|^2 \tag{4.19}$$

$$M_{\mathrm{Loc}}^{Y}(\omega_R) = \left|\widetilde{\boldsymbol{E}}_{\mathrm{Loc}}^{\mathrm{PW}-Y}(\omega_R)\right|^2 = \left|\widetilde{E}_{\mathrm{Loc}}^{\mathrm{PW}-Y}(\omega_R)\, \boldsymbol{e}_R^Y\right|^2 \tag{4.20}$$

$M_{\mathrm{Loc}}^{Z}(\omega_L)$ is the local field enhancement generated by a laser polarized along Z with frequency ω_L. $\widetilde{E}_{\mathrm{Loc}}^{Z}(\omega_L)$ and $\boldsymbol{e}_L^Z$ are the magnitude and the versor of $\widetilde{\boldsymbol{E}}_{\mathrm{Loc}}^{Z}(\omega_L)$. These quantities were defined in Eq. (4.6).

$M^Z_{\mathrm{Loc}}(\omega_R)$ is the local field enhancement generated by a laser polarized along Z with frequency ω_R. $\widetilde{E}^{\mathrm{PW}-Z}_{\mathrm{Loc}}(\omega_R)$ and $\boldsymbol{e}^Z_R$ are the magnitude and the versor of $\widetilde{\boldsymbol{E}}^{\mathrm{PW}-Z}_{\mathrm{Loc}}(\omega_R)$. These quantities were defined in Eq. (4.15).

$M^Y_{\mathrm{Loc}}(\omega_R)$ is the local field enhancement generated by a laser polarized along Y with frequency ω_R. $\widetilde{E}^{\mathrm{PW}-Y}_{\mathrm{Loc}}(\omega_R)$ and $\boldsymbol{e}^Y_R$ are the magnitude and the versor of $\widetilde{\boldsymbol{E}}^{\mathrm{PW}-Y}_{\mathrm{Loc}}(\omega_R)$. These quantities were defined in Eq. (4.15).

$M^Z_{\mathrm{Loc}}(\omega_L)$ is generated by the laser; $M^Z_{\mathrm{Loc}}(\omega_R)$ and $M^Y_{\mathrm{Loc}}(\omega_R)$ are generated by the virtual problem (i.e., the dummy dipole) but are equivalent to the local fields that would be generated by a laser polarized along Z and along Y, for the considerations in the previous section.

T is called the surface selection rule factor; in fact its magnitude depends on $\widehat{\alpha}_N$ and on the orientation of electric fields generated at the molecule position. It is worth noticing that the laser polarization (Z) is in general different from $\boldsymbol{e}^Z_L$ (due to the boundary conditions at the interface between two media [68]) and from the direction of the induced Raman dipole $\boldsymbol{p} \propto \widehat{\alpha}_N \cdot \boldsymbol{e}^Z_L$ ($\widehat{\alpha}_N$ is a tensor). Therefore, T couples the problems of the local field and radiation enhancements through the Raman polarizability tensor in a not trivial way. It can be demonstrated that $0 \leq T \leq \frac{15}{4}$ [12]. This factor in general does not affect significantly the value of G_{SM}, which normally amounts to several orders of magnitude, unless the orientation of the local fields in Eq. (4.17) combines with the molecular tensor, leading to the unluckily case of $T \sim 0$: this is however a very peculiar case [12].

4.3.1.5 $|E|^4$ Approximation and Its Zero Stokes Shift Limit

The G_{SM} in the commonly adopted E^4 approximation can be written as:

$$G_{\mathrm{SM}}\left(E^4\right) = M^Z_{\mathrm{Loc}}(\omega_L)\, M^Z_{\mathrm{Loc}}(\omega_R) \tag{4.21}$$

Notice that, within this approximation, the total enhancement factor is worked out as the product of two local field enhancement factors, one determined at the laser and the other one at the Raman frequency. In both cases, the source that generates the field is polarized along Z (i.e., like the laser excitation source).This expression closely resembles that of $G^{\parallel}_{\mathrm{SM}}$ in Eq. (4.16).

A comparison between the general expression of G_{SM}, Eq. (4.16), and the approximated one, Eq. (4.21), reveals which conditions have to be met for the E^4 approximation to be valid.

- $T^{\parallel} \sim 1$

The value of $T^{\parallel}$, being in between 0 and $\frac{15}{4}$, is not expected to provide strong contributions, unless very specific combinations of the local field and molecular orientation bring $T^{\parallel}$ near 0

- $G^{\parallel}_{\mathrm{SM}} = M^Z_{\mathrm{Loc}}(\omega_L)\, M^Z_{\mathrm{Loc}}(\omega_R)\, T^{\parallel} \quad \gg \quad G^{\perp}_{\mathrm{SM}} = M^Z_{\mathrm{Loc}}(\omega_L)\, M^Y_{\mathrm{Loc}}(\omega_R)\, T^{\perp}$

Supposing a small effect of $T^{\parallel}$ and $T^{\perp}$, this requirement means that when a sample is illuminated with a laser polarized along Z, the SERS signal measured in parallel configuration should exceed the SERS measured in perpendicular configuration. This is equivalent to having $M^{Z}_{\mathrm{Loc}}(\omega_R) \gg M^{Y}_{\mathrm{Loc}}(\omega_R)$. This condition can be experimentally fulfilled if the SERS experiment is carried out by exciting the sample with a laser polarized along the direction that generates the strongest local field.

In the zero Stokes shift limit, Eq. (4.21) can be further simplified considering $M^{Z}_{\mathrm{Loc}}(\omega_L) \approx M^{Z}_{\mathrm{Loc}}(\omega_R)$ (i.e., the local field enhancement at the laser and Raman frequency are the same):

$$G_{\mathrm{SM}}\left(E^4\right) = \left[M^{Z}_{\mathrm{Loc}}(\omega_L)\right]^2 = \left[\frac{\boldsymbol{E}_{\mathrm{Loc}}(\omega_L)}{\boldsymbol{E}(\omega_L)}\right]^4 \tag{4.22}$$

This expression represents $G_{\mathrm{SM}}(E^4)$ in the zero Stokes shift limit of the E^4 approximation. An average enhancement factor, representative of the enhancement of a substrate, can be defined by averaging the single-molecule one over the allowed molecular orientations and over the surface of the metallic substrate. Indicating the former average with <> and the latter one with {}, the average enhancement can be expressed as:

$$G^{\mathrm{Em}}_{\mathrm{SERS}} = \{< G_{\mathrm{SM}} >\} \tag{4.23}$$

For simplicity of notation, we shall indicate the enhancement factor as G_{SERS} in the following sections, both for the single molecule and for the average case: from the context, it will be clear which of the two we are referring to.

Some papers in the literature show explicitly, by means of experiments, cases in which the E^4 approximation is not appropriate and a more sophisticated treatment, based on Eq. (4.16), is necessary to describe the observed SERS enhancements: due to the nature of the approximations necessary to achieve Eq. (4.21), typically these papers deal with polarized detection of the SERS scattering, including the measurement of depolarization ratios (i.e., $\rho = (I_{\perp}/I_{\parallel})$). For example, Le Ru et al. [69] fabricated an array of oblated gold nanoparticles on ITO by electron beam lithography and functionalized them with rhodamine 6G and crystal violet: the most striking effect they demonstrated is that, if the functionalized sample is illuminated with a laser polarized along the short axis of the nanoparticles, the perpendicular component of the SERS signal is almost eight times stronger than the parallel one, leading to a sort of "polarization inversion." Conversely, excitation along the longest axis of the nanoparticles produced a SERS scattering mainly polarized parallel. Le Ru et al. [18] also showed that, in a partially aggregated Ag colloid in solution, the depolarization ratio of benzenethiol amounts to $\frac{1}{3}$ for all Raman bands, regardless of their symmetry, while in general the depolarization ratio depends on the symmetry of the Raman band [52]. Also Fazio et al. [70] used self-organized gold nanowires, functionalized with methylene blue, to carry out a

complete study of the dependence of the SERS signal on the excitation and on the detection polarization arrangement. The authors interpreted the data with a model that goes beyond the E^4 approximation, based on Eq. (4.16).

4.3.2 Chemical Enhancement

The chemical enhancement originates from a modification of the electronic polarizability of a molecule, caused by its interaction with the surface of a SERS substrate: the molecule can interact either with the bare metal or with a layer of suitable receptors, used to increase the affinity of the substrate toward the molecule of interest [71]. A modification of the polarizability, with respect to the isolated molecule, implies a change of the Raman cross section of the vibrational modes and hence of the corresponding Raman intensities: this fact can be easily realized considering that the Raman cross section is proportional to the first derivative of the polarizability with respect to the vibrational normal mode (Q_k): $P_{\text{Raman}} \propto \sigma_k \propto \frac{\partial \alpha(Q_k,\omega)}{\partial Q_k}$ [52]. In general, the chemical enhancement for the k-th vibrational mode can be formally expressed as the ratio between the Raman cross section of the molecule adsorbed on the substrate (σ_k^{ads}) and of the "free" molecule (σ_k^{free}):

$$G_{\text{SERS}}^{\text{Chem}} = \frac{\sigma_k^{\text{ads}}}{\sigma_k^{\text{free}}} \tag{4.24}$$

The interaction of a molecule with a surface is in general classified on the basis of the adsorption enthalpies involved, that is, on the basis of the strength of the interaction [72]. In physisorption (adsorption enthalpy less negative than −25 kJ/mol), van der Waals forces are responsible for the substrate-molecule interaction: in this case, the small enthalpy change is not sufficient to break bonds, and hence the adsorbed molecule is expected to preserve its identity, with a possible distortion of the electronic cloud. On the other hand, in chemisorption (adsorption enthalpy more negative than −40 kJ/mol), the molecule adsorbs on the surface by forming a chemical bond (usually covalent). This may lead to significant or drastic changes in the electronic structure of the molecule: for example, the point group symmetry can be modified, leading to the appearance of vibrational modes forbidden in the isolated molecule, and new electronic states may arise from the substrate-molecule interaction.

A well documented case of chemical effect involves the formation of a "complex" between the molecule and the metal: this complex can possess an optical absorption, corresponding to a charge transfer (CT) transition from the molecule to the metal or vice versa, which falls in the same spectral region of the excitation laser. Consequently, a strong enhancement of some of the Raman bands can be observed, due to the resonance Raman effect [52]. The occurrence of a CT state requires the proximity in energy of the Fermi level of the metal with the highest

occupied (HOMO) or with the lowest unoccupied molecular orbitals (LUMO) of the molecule: this condition is not so uncommon; in fact the Fermi level of metals lies in between the HOMO and LUMO of many organic molecules [13]. In order to explain in more detail how the formation of a CT state affects the intensity of the Raman signals from the molecule, one can resort to the theories proposed by Lombardi and Birke [13]: the authors developed a formalism, based on the theory of resonant Raman scattering by Albrecht [52], which treats simultaneously the effect of the plasmon, CT, and molecular resonances on the intensity of the Raman bands of the molecule. When the excitation laser is resonant with the plasmon resonance and at least one between the CT and molecular resonances, the dominant term is the following:

$$P_{\mathrm{SERS}} \propto \left|R_{\mathrm{IFK}}(\omega)\right|^2 = \left| \frac{\mu_{KI}\mu_{FK}h_{IF}\langle i|Q_k|f\rangle}{\left((\varepsilon'(\omega)+2\varepsilon_d)^2+\varepsilon''(\omega)^2\right)\left(\omega_{FK}^2-\omega^2+\gamma_{FK}^2\right)\left(\omega_{IK}^2-\omega^2+\gamma_{IK}^2\right)} \right|^2 \quad (4.25)$$

In the numerator of Eq. (4.25), μ_{KI} and μ_{FK} are the transition dipole moments between the electronic states, $|I\rangle$, $|F\rangle$, and $|K\rangle$: they correspond to the ground state, a charge-transfer state, and an excited state localized on the molecule, respectively. The energy diagram of the metal-molecule system is summarized in Fig. 4.5a. $h_{IF} = \left\langle I\left|\frac{\partial V_{eN}}{\partial Q_k}\right|F\right\rangle$ is the Herzberg-Teller coupling parameter, and V_{eN} is the electron–nuclear attraction term in the Hamiltonian, evaluated at the equilibrium nuclear positions. Q_k is the vibrational Raman mode considered; $|i\rangle$ and $|f\rangle$ are the initial and final vibrational states. The numerator identifies the "surface selection rules," that is, the vibrational modes that turn out to be enhanced and, to some extent, their intensity ratio.

In the denominator, $\varepsilon^{'}(\omega)$ and $\varepsilon^{''}(\omega)$ are the real and imaginary part of the dielectric constant of the metal, $\varepsilon(\omega)=\varepsilon^{'}(\omega)+i\varepsilon^{''}(\omega)$; ε_d is the real dielectric constant of the (non-absorbing) surrounding material; ω_{FK} and ω_{IK} are the transition frequencies between the F and K and I and K, respectively; ω is the excitation laser frequency; and γ_{FK} and γ_{IK} are the damping constants. They are related to the bandwidth and hence to the intensities of the resonances: in particular, the intensity of the resonances is proportional to the inverse of their fourth power, γ^{-4}. In the plasmonic resonance, the role of γ is played by $\varepsilon^{''}(\omega)$. The denominator establishes the relative contribution to the SERS signal brought about by the three types of resonances involved: the plasmon, CT, and molecular ones, represented by the first, second, and third factor, respectively.

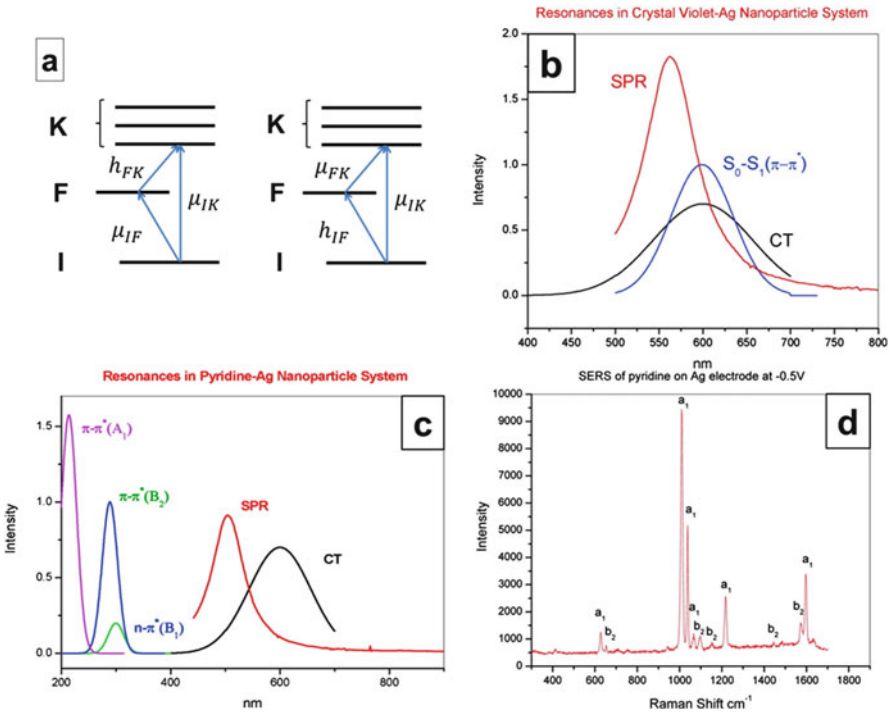

Fig. 4.5 (**a**) Energy-level diagram for the metal-molecule system (Reproduced (adapted) with permission from Ref. [78]). (**b**) Resonances in the crystal violet – silver nanoparticle system (Reproduced with permission from Ref. [13]). (**c**) Resonances in the pyridine – silver nanoparticle system (Reproduced with permission from Ref [13]). (**d**) SERS of pyridine on a silver electrode. The symmetry species of the most enhanced modes (a_1 and b_2) are shown. All other modes are much weaker or not seen (Reproduced with permission from Ref. [78])

4.3.2.1 Contribution of the Plasmonic, Charge-Transfer, and Molecular Resonances

By inspecting the denominator of Eq. (4.25), the following points can be highlighted [13]:

- *The plasmonic resonance* is accounted for by the first term, $((\varepsilon'(\omega)+2\varepsilon_d)^2+\varepsilon''(\omega)^2)$, and becomes resonant when $\varepsilon'(\omega)=-2\varepsilon_d$; for simplicity, this expression refers to the case of a single nanosphere.
  - In this case, in order to figure out for which laser wavelengths the resonance condition is fulfilled, one can in first approximation simply assume that the local field enhancement follows the extinction spectrum of the plasmonic substrate. However, this approach is often not adequate, and more generally, the near-field distribution should be measured experimentally by means of wavelength-scanned SERS (WS-SERS) [73–75], using non-resonant organic

molecules that, in addition, do not give rise to the formation of complexes with the metal.

- *The CT resonance* is accounted for by the second term, $\left(\omega_{FK}^2 - \omega^2 + \gamma_{FK}^2\right)$, and becomes resonant when $\omega_{FK} = \omega$.
  - The possible existence of a CT state can be predicted if estimates of the Fermi level of the metal and of the energy levels of the molecule are available, either theoretically or experimentally. For example, the HOMO and LUMO energies of crystal violet have been measured electrochemically from one-electron oxidation and reduction potentials in solution on silver electrodes, showing that the Fermi level of the metal lies approximately at the same energy as the LUMO of the dye. Hence, by illuminating crystal violet adsorbed on a silver surface with a laser at 633 nm, a molecule-to-metal transition can be excited [76].
  - Charge-transfer resonances can be experimentally identified by measuring G_{SERS} at several excitation wavelengths and then decoupling the contributions from the plasmon and the molecular resonance enhancements. The CT resonance of crystal violet on Au has been evidenced, in Ref [77], by measuring the G_{SERS} profiles of some crystal violet Raman bands on a flat Au surface: the use of a flat gold surface ruled out the presence of plasmon resonances, and symmetry consideration allowed the authors to decouple the CT resonance from the intramolecular electronic resonance.
- *Intramolecular resonances* are represented by the third term, $\left(\omega_{IK}^2 - \omega^2 + \gamma_{IK}^2\right)$, and become resonant when $\omega_{IK} = \omega$.
  - Molecular resonances can be inferred from the absorption spectrum of the molecule.

In Fig. 4.5b, c, the spectral distributions of three resonances involved in the denominator are shown for two widely used organic molecules in SERS, namely, crystal violet and pyridine: the data are experimentally determined by following the strategies discussed in the points above. Figure 4.5b, c allows one to identify in which spectral region each resonance can be excited by the laser. An important point to highlight is that for crystal violet, both a CT and a molecular resonance occur at 633 nm, leading to three simultaneously resonant factors in Eq. (4.25) and hence to a very strong enhancement. This may explain why crystal violet is so common in single-molecule SERS studies.

4.3.2.2 The Surface Selection Rules

By inspecting the numerator of Eq. (4.25), the following points can be highlighted [13]:

- $\langle i | Q_k | f \rangle$ simply indicates the usual selection rule for vibrational spectroscopy $f = i \pm 1$, and hence no overtones are formally predicted by this approach.

- All terms must be nonzero for a mode Q_k to be enhanced. Notice that all terms are connected to each other. In fact given the symmetry of an allowed mode Q_k, this will define the symmetry of the CT state $|F\rangle$ coupled to the ground state through h_{IF}; the transition dipole moment μ_{FK} establishes then the symmetry of the excited molecular state(s) $|K\rangle$ coupled to $|F\rangle$; μ_{KI} indicates that the state(s) $|K\rangle$ coupled to $|F\rangle$ must also be allowed from the ground state $|I\rangle$. Both μ_{KI} and μ_{FK} depend on the geometrical arrangement of the molecule and of the molecule-metal complex on the surface.
- An analysis of the symmetry of the states and of the operators involved leads to the following expression that connects the symmetry species of the allowed vibrational mode, $\Gamma(Q_k)$, and the symmetry of the molecular electronic states $|K\rangle$ allowed from the ground state,Γ_K [78]:

$$\Gamma\left(Q_k\right) = \sum_K \Gamma_K \tag{4.26}$$

The sum over K runs over all allowed molecular states. In order to obtain the expression above, two assumptions are necessary: (a) Only the component of μ_{CT} perpendicular to the surface ($\mu_{\mathrm{CT}}^{\perp}$) has been considered: this is justified with the reasonable assumption that the electric field is oriented mainly perpendicularly to the metallic surface. (b) $\Gamma\left(\mu_{\mathrm{CT}}^{\perp}\right)$ is totally symmetric: this is true for several aromatic heterocyclic organic compounds like pyridine, pyrazine, pyrimidine, and pyridazine that are attached to the metallic surface through an Ag-N bond with the molecular plane perpendicular to the surface [78].

– Equation (4.26) shows that the allowed vibrational modes belong to the same symmetry species of the allowed electronic transitions from the ground state. Notice that since the Raman intensity is proportional to $|\mu_{\mathrm{KI}}|^2$, the relative intensity of the vibrational modes in the SERS spectrum should be dictated by the oscillator strength of the allowed electronic transitions they are coupled to.
– This fact has been verified for all molecules mentioned above [78]. As an example, we show explicitly the case of pyridine: the oscillator strength for the molecular electronic transitions follows the order $A_1 > B_2 > B_1$ (Fig. 4.5c), and the SERS spectrum of pyridine exhibits exactly the same trend in the band intensity $a_1 > b_2 > b_1$ (Fig. 4.5d).

As a final note, it is worth noticing that the CT chemical enhancement can occur not only by interaction of the molecule with a metal but also by interaction of the molecule with a semiconductor [79]. As it will be mentioned in Sect. 4.7, (doped) semiconductors are attracting a strong interest as alternative plasmonic materials and can potentially find use as materials for SERS.

Table 4.2 Approximate maximum values for G_{SERS}^{Chem} and G_{SERS}^{Em}

G_{SERS}	Approx. max. value	Note	References
G_{SERS}^{Chem}	10^2	Atomic scale roughness	[15, 25, 71, 80]
G_{SERS}^{Chem}	10^4	CT resonance	[13]
G_{SERS}^{Em}	10^8	Averaged over the substrate	[20, 25]
G_{SERS}^{Em}	10^{10}	In a hot spot	[81]

4.3.2.3 Comparison with the Electromagnetic Enhancement

From the point of view of the magnitude, the chemical enhancement in the absence of a CT mechanism, normally ascribed to atomic scale roughness [15, 80], is considered to contribute with a maximum factor of 10–10^2 [15, 25, 71, 80]. Higher values, up to 10^3–10^4, can be reached if a CT resonance is involved, as reported by Lombardi et al. [13]. The electromagnetic enhancement is normally accepted to contribute up to 10^7–10^8 if averaged over the surface of a substrate and approximately 10^{10} in hot spots, as it will be shown in Sect. 4.5 [20, 25, 81]. Table 4.2 summarizes these approximate values for the two types of enhancements.

Concerning the distance dependence, the chemical enhancement is considered a short-range effect since it requires physical contact or very close proximity between the substrate and the molecule. The electromagnetic effect instead is considered a long-range effect, since it depends on the decay of the electromagnetic field from the surface that becomes significant after several nm. The distance dependence of the electromagnetic enhancement is discussed in Sect. 4.4.

4.4 Distance Dependence

In the simple case of a metallic sphere, with a diameter much smaller than the wavelength of light (quasi-static approximation), theory shows that G_{SERS}^{Em} follows a $\frac{1}{d^{12}}$ dependence [53]:

$$\frac{G_{SERS}^{Em}(d)}{G_{SERS}^{Em}(0)} = \left[\frac{a}{a+d}\right]^{12} \tag{4.27}$$

a is the radius of the sphere and d the distance of the molecule from the surface of the sphere, as depicted in Fig. 4.6a. Notice that the SERS signal possesses a different distance dependence from G_{SERS}^{Em}, since the surface area, and hence the number of illuminated molecules, scales with r^2: the expected distance dependence of the SERS signal is therefore [82]:

$$\frac{P_{SERS}(d)}{P_{SERS}(0)} = \left[\frac{a}{a+d}\right]^{10} \tag{4.28}$$

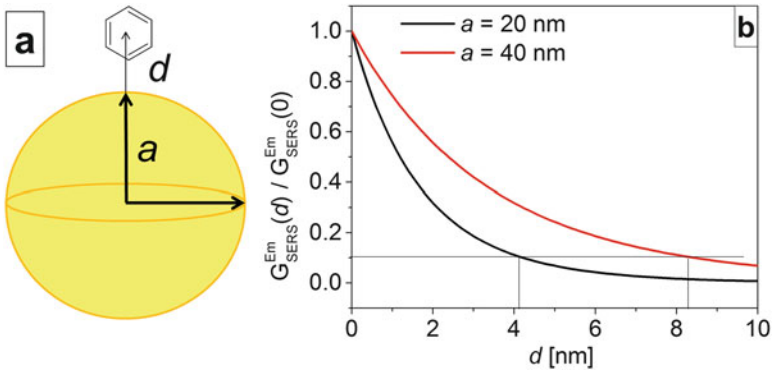

Fig. 4.6 (**a**) Graphical representation of the system studied, in which a molecule is placed at distance d from the surface of a metallic sphere of radius a (Reproduced (adapted) from Ref. [53] with permission). (**b**) G_{SERS}, normalized to the value at the surface, is plotted as a function of d for a sphere with radius $a = 20$ nm (*black line*) and for a sphere with radius $a = 40$ nm (*red line*)

$\frac{G^{Em}_{SERS}(d)}{G^{Em}_{SERS}(0)}$ in Eq. (4.27) has been plotted in Fig. 4.6b for two spheres, with radius $a = 20$ and 40 nm. The enhancement reduces to about 1/10 at a distance of 4 nm (8 nm) from the surface of the 20 nm (40 nm) sphere: this indicates that little enhancement is achieved from molecules a few monolayers away from the surface, making SERS a *surface-selective* technique. On the other hand, as mentioned in Sect. 4.3.2.3, when the electromagnetic enhancement is compared to the chemical one, the first one is often referred to as a "long-range" effect and the second one as a "short-range" effect, since it requires much closer proximity (or contact) between the molecule and the metal.

Several papers in the literature have tackled the distance dependence of SERS. The general approach they use relies on the following points: (a) developing an experimental procedure that allows one to control the spacing between the Raman probe and the metallic surface; (b) measuring G_{SERS} (or P_{SERS}) as a function of the distance and fitting the results with Eq. (4.27) or (4.28) in order to determine the radius of the nanoparticles, a; (c) measuring of the size of the metallic features on the SERS substrate, by means of morphological characterization techniques like atomic force microscopy (AFM) or scanning electron microscopy (SEM); and (d) comparing the nanoparticle radius determined from the fit with the one from the morphological analysis: if the radii obtained with the two methods are consistent, the expected distance dependence is confirmed.

In the following, we summarize the strategies used by several authors in the investigation of the $G^{Em}_{SERS/P_{SERS}}$ dependence on the distance.

Compagnini et al. [83] used self-assembled monolayers (SAMs) of linear alkanethiols with different lengths to modulate the distance between the terminal -CH_3 group of the thiols themselves and the surface of a plasma-roughened silver substrate. $CH_3(CH_2)_nSH$ molecules, with $n = 5, 7, 11, 17$, provided a spacing

variable in between 0.8 and 2.5 nm. The -CH_3 Raman signals (symmetric stretching, asymmetric stretching, rocking) as a function of the distance were fitted with Eq. (4.28): a good fit was obtained for $a = 18$, a value in agreement with the size of the metallic features at the surface of the SERS substrate determined by AFM.

Kennedy et al. [84] similarly to Compagnini et al., used SAMs of linear alkanethiols, with n between 7 and 17, as spacers to tune the distance from a silver foil roughened with nitric acid. The *tert*-butylbenzene was used as a probe of the Raman signal, since its sterical hindrance prevented it from intercalating into the SAM layer. The distance dependence of the SERS signal was investigated in the range 1.6 to 2.8 nm. The value of a, obtained from the fit with Eq. (4.28), turned out to be consistent with the results of AFM measurements.

Kovacs et al. [85] made use of Langmuir-Blodgett (LB) monolayers of arachidic acids as a spacer, deposited on silver islands. The SERS probe was a phthalocyanine monolayer, whose distance from the substrate was modulated between 0.85 nm and 14 nm. Instead of using Eq. (4.27) or (4.28) for the fit, valid for a sphere, the authors used the Gersten-Nitzan model that accounted for the hemispheroidal aspect ratio of the silver islands. Good agreement between the calculated and experimentally observed G_{SERS}, as a function of the distance, was evidenced.

Masango et al. [86] exploited atomic layer deposition (ALD) to deposit monolayers of Al_2O_3 on an SERS substrate, fabricated by evaporation of a silver film over a self-assembled monolayer of polystyrene spheres (Ag-FON). ALD allowed a very precise control of the spacer thickness, which was tuned between 0 and 3 nm, with very small steps (Angstrom resolution). The SERS-active species, trimethyl aluminum (TMA), was deposited on top of the spacer: either the C-H or the Al-(CH_3) symmetric stretches were used to monitor the SERS signal as a function of the distance from the surface. Figure 4.7a shows the trend of the SERS signal as a function of the spacer thickness, and Fig. 4.7b shows the structure of the Ag-FON substrates. The fit of the trace required a short- and a long-range component: $\frac{P_{\mathrm{SERS}}(d)}{P_{\mathrm{SERS}}(0)} = C_1\left[\frac{a_1}{a_1+d}\right]^{10} + C_2\left[\frac{a_2}{a_2+d}\right]^{10}$. This indicated that two morphological features contributed to the SERS signal, one with $a_1 = 1$ nm and $a_2 = 20$ nm. Only the larger one could be recognized with a SEM analysis of the substrate, due to intrinsic measurement limitations.

Other interesting experimental works are, for example, those by Marotta et al. [87] and by Murray et al. [88] who used DNA strands and polymer layers to tune the distance between the Raman probe and the substrate, respectively: the former investigated the distance dependence in the 1–6 nm range and the latter in the 0–12 nm range.

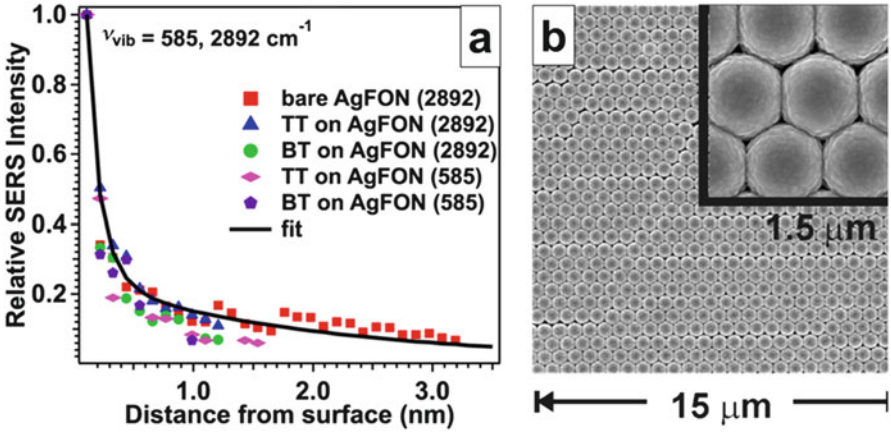

Fig. 4.7 (**a**) Normalized SERS intensity of the symmetric C–H stretch at 2892 cm^{-1} and symmetric Al-CH_3 stretch at 585 cm^{-1} (from TMA), as a function of distance from bare Ag-FON and from Ag-FONs functionalized with toluenethiol (TT) and benzenethiol (BT) SAMs. Thiol Raman signals were used as internal standards to compensate spot-to-spot variations. The black solid line is the fit to the data (Reproduced with permission from Ref. [86]). (**b**) SEM images of the Ag-FON substrate (Reproduced with permission from Ref. [148])

4.5 Definition and Properties of Hot Spots

4.5.1 Definition

Hot spots are in general defined as spatial regions at the surface of metallic substrates where the local field reaches extremely high values compared to the excitation field. From a structural point of view, Kleinman's definition of hot spot says [89] "a junction or close interaction of two or more plasmonic objects where at least one object has a small radius of curvature on the nm scale." Some authors defined hot spots also as very sharp (high curvature) features at the surface of single objects, due to the intense fields that can be localized at their surface [90]: in general, however, the field intensity at the surface of single objects is not as high as in junctions.

4.5.2 Extinction and Enhancement as a Function of the Gap Size

As a case study, we illustrate what happens to the extinction and to $G^{\mathrm{Em}}_{\mathrm{SERS}}$ in a dimer formed by identical silver spheres when the gap size is varied. In this example, studied in Ref. [12], the spheres have radius $a = 25$ nm and are separated by a (variable) gap g; the excitation laser is polarized along the main axis of the dimer

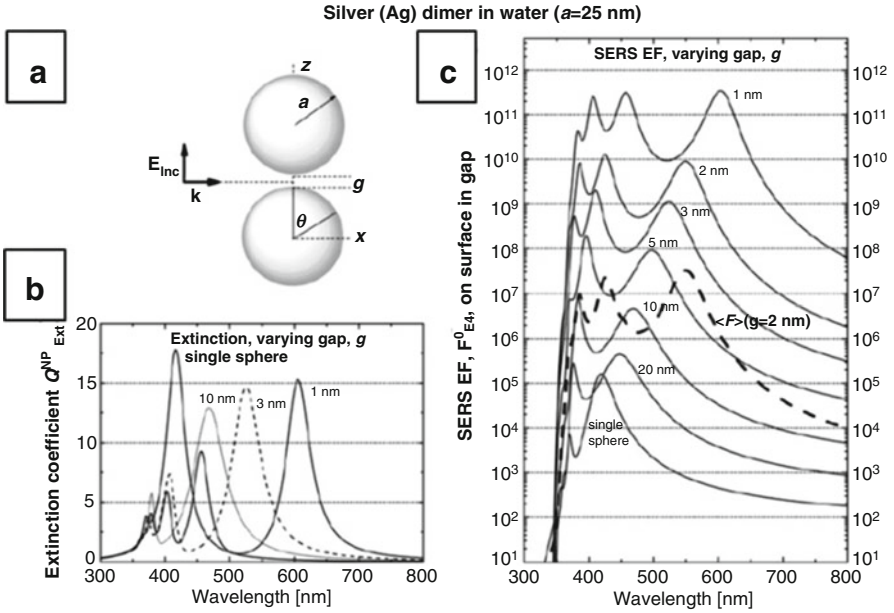

Fig. 4.8 (**a**) Graphical representation of the dimer that has been studied. (**b**) Extinction coefficient of the single sphere and of dimers with different gap sizes. (**c**) G_{SERS} for a single sphere and for dimers with different gap sizes (Reproduced with permission from Ref. [12])

(Z) and propagates along X; the dimer is immersed in water. $G^{\mathrm{Em}}_{\mathrm{SERS}}$ is calculated for a molecule placed at the surface of one of the two spheres, along the Z-axis. Figure 4.8a shows the geometrical arrangement. The following points are worth highlighting from Fig. 4.8b (extinction spectra) and Fig. 4.8c ($G^{\mathrm{Em}}_{\mathrm{SERS}}$ spectra):

Extinction Coefficient Spectra

- The single particle exhibits only one peak at about 420 nm, corresponding to the surface plasmon resonance of the particle.
- In the dimer, a new redshifted resonance appears: its redshift increases reducing the size of the gap. It is due to the dipole-dipole coupling between the spheres, and it is the most relevant for SERS.
- The resonances that are present in the spectra below 400 nm are due to higher-order coupling between the two nanospheres.

Enhancement Factor Spectra

- The resonances present in the extinction spectra are qualitatively present also in the $G^{\mathrm{Em}}_{\mathrm{SERS}}$ spectra.
- The reduction of the gap produces a very strong increase of the enhancement at the hot spot. For a single sphere, $G^{\mathrm{Em}}_{\mathrm{SERS}}$ amounts to about 10^5; for a dimer with $g = 10$ nm, it amounts to $\sim 5 \cdot 10^6$; and for $g = 1$, it amounts to $\sim 5 \cdot 10^{11}$. These

considerations highlight the importance of hot spots in the enhancement of the SERS signal.

  - A question that may arise is whether different geometrical configurations or larger aggregates could even further enhance the signal: in this respect, Moskovits commented that the dimer configuration already accounts for most of the additional enhancement achievable upon aggregation [16], leaving maybe space for an order of magnitude improvement in aggregates with optimized geometry and size.
  - The increase of enhancement upon aggregation is a very general behavior almost always encountered: however, in few systems, a limited increase or even a decrease of the enhancement is observed when nanoparticles are brought close to each other. These systems are hollow nanoparticles in which a reduction of the inner field upon interaction is not compensated by the interparticle field increase [75, 91].
  - The increase of $G_{\mathrm{SERS}}^{\mathrm{Em}}$ that can be achieved by narrowing the gap is limited due to the emergence, at $g < 1$ nm, of quantum mechanical effects like electron tunneling [92].

- The enhancement averaged over the surface of the whole dimer with $g = 2$ nm (dashed line in Fig. 4.8c) is about 300 times smaller than the enhancement at the hot spot.

  - This illustrates clearly that most of the signal comes from the hot spot rather than from the rest of the nanoparticle surface. More precisely, it can be demonstrated that in a 2 nm gap dimer, 80% of the SERS signal is generated by 0.64% of the molecules, assuming uniform coverage of the surface [18].

Comparison Between Extinction and Enhancement Spectra

- Although, as already mentioned, the position of the resonances present in the extinction coefficient spectra are qualitatively reproduced in the G_{SERS} spectra, there is no relation between the magnitude of the extinction and the magnitude of the enhancement. This can be easily realized, for example, noting that the extinction coefficients of the single sphere and of the 1 nm gap dimer are almost equal: on the other hand, the G_{SERS} goes from $\sim 10^5$ for the former to $\sim 5 \cdot 10^{11}$ for the latter.

4.5.3 SERS Enhancement Distribution on a Substrate

The distribution of the enhancement on a SERS substrate is in general very inhomogeneous, with a small number of very active regions and large areas exhibiting only a moderate enhancement. This topic was investigated experimentally by Fang et al. [93], who carried out a very clever study on a silver film over nanosphere (Ag-FON) SERS substrate [80], functionalized with a monolayer of benzenethiol. The authors exploited two effects: a) when illuminated by a laser, molecules may

undergo photobleaching if the intensity they experience is larger than a certain damage threshold, and b) molecules on the substrate are exposed to different near-field intensities, depending on how strong the enhancement is in the spatial regions where they are located. The authors used a pulsed laser to induce photobleaching, and its intensity was gradually increased in several steps. At low pulsed laser intensity, only molecules residing in the hottest spots were burned out; increasing the intensity, a larger number of molecules were burned out, leading to a reduction of the probed Raman signal. At every step, a weak continuous wave (CW) laser was used to probe the Raman signal of the non-bleached benzenethiol molecules, through their C-H stretching signal around 3000 cm^{-1}. This experimental procedure allowed the authors to quantify the probability distribution of the enhancement, assuming for it a power law dependence. It is clear from the data in Ref. [93] that the SERS substrate exhibited a very strong enhancement heterogeneity: the most striking finding is that only 0.01% of the molecules, to which correspond an enhancement $>10^9$, account for almost 25% of the SERS signal. This implies that with sub-monolayer coverage, or when the analyte-substrate interaction is dynamic (e.g., in solution the analyte may adsorb and desorb continuously from the surface), very large fluctuations in the signal and in the enhancement are possible [89].

4.6 Near- Versus Far-Field Properties

A relevant question, both from a fundamental and a practical standpoint, regards the possible relation between the optical far-field and near-field responses of metal nanostructures. The possibility of predicting the spectral region in which the SERS substrate is mostly efficient, on the basis of its extinction/scattering/absorption spectra, would be of great advantage for the experimentalists, since the far-field properties are much easier to determine than the spectral distribution of G_{SERS}: indeed, measuring the G_{SERS} profile, with a sufficient number of points, requires the use of a specially designed experiment, not so common in the literature, in which tunable laser sources and a triple spectrograph are employed (wavelength-scanned SERS (WS-SERS)) [73, 75].

Unfortunately, it is generally accepted that far-field spectra normally do not provide a good indication of spectral regions in which the local field is more intense [14, 81]. In the following, we want to show some examples from the literature in which this topic has been investigated and discussed.

In isolated metal nanoparticles of sufficient small size, Messinger et al. [94] demonstrated, by means of theoretical simulations, that the extinction/absorption spectrum and the local field enhancement qualitatively exhibit a similar spectral dependence.

In ordered ensembles of (weakly interacting) identical objects, correlation between the extinction and the G_{SERS} profile was demonstrated by McFarland et al. [73] and by Félidj et al. [95]: the former studied an hexagonal array of nanoparticles (fabricated by nanosphere lithography), and the latter studied an array

of nanorods (fabricated by electron beam lithography). McFarland et al. [73] also proved that the G_{SERS} profile maximum (plotted as a function of the excitation wavelength) falls at a slightly higher energy compared to the extinction maximum. Assuming that the near-field enhancement follows the extinction spectrum, the blueshift is explained by the fact that the G_{SERS} is proportional to the product $|\boldsymbol{E}_{\mathrm{Loc}}(\omega_L)|^2|\boldsymbol{E}_{\mathrm{Loc}}(\omega_R)|^2$, rather than to $|\boldsymbol{E}_{\mathrm{Loc}}(\omega_L)|^4$ (see Eq. 4.21): since $\omega_R < \omega_L$, the product $|\boldsymbol{E}_{\mathrm{Loc}}(\omega_L)|^2|\boldsymbol{E}_{\mathrm{Loc}}(\omega_R)|^2$ is maximized when the extinction peak (λ_{ext}) lies approximately halfway in between the excitation laser (λ_L) and the Raman band of the molecule with which the substrate was functionalized (λ_R): $\lambda_L < \lambda_{\mathrm{ext}} < \lambda_R$. McFarland demonstrated also that the shift between the G_{SERS} and the extinction peaks depends on the frequency of the Raman band (ω_R) used to work out the G_{SERS} profile, and the lower the Raman shift of the band, the lower the blueshift observed between the extinction and the G_{SERS} profiles. Figure 4.9 shows the relation between the extinction and the near-field spectra for McFarland's array of nanotriangles. This rule is however not of general validity. For example, Guillot et al. [96] studied arrays of gold nanocylinders in which the extinction maximum was varied by modifying the nanocylinder diameter, keeping constant their height and spacing; the spacing among cylinders was chosen large enough to avoid near-field coupling. The authors fabricated several arrays of nanocylinders by EBL, with diameters ranging from 80 to 580 nm, and functionalized them with trans-1,2-bis (4-pyridyl)ethylene (BPE). The G_{SERS} were measured at two excitation wavelengths, 633 and 785 nm, referring to the 1200 cm^{-1} band of BPE. They found that the G_{SERS} at λ_L=633 nm (λ_R = 685 nm for the BPE band) was highest for nanocylinders with diameter of about 130 nm, whose extinction peaked at $\lambda_{\mathrm{ext}} \sim 650$ nm: this result was in agreement with the relation $\lambda_L < \lambda_{\mathrm{ext}} < \lambda_R$ previously found by McFarland. However, at λ_L=785 nm excitation (λ_R = 867 nm for the BPE band), the maximum enhancement was found for nanocylinders with diameters of about 220 nm, whose extinction peak was at $\lambda_{\mathrm{ext}} \sim 750$ nm, hence with $\lambda_{\mathrm{ext}} < \lambda_L < \lambda_R$.

In strongly coupled systems, more striking differences between the far- and near-field spectra are found, with respect to the previously described plasmonic substrates. A first example has been already discussed in Sect. 4.5, where the calculated extinction and enhancement spectra of dimers of Ag nanospheres showed no appreciable relation: those considerations have been further discussed in detail in Ref. [81]. In another work, Kleinman et al. [17] showed experimentally and theoretically that for single dimers and trimers of Au nanoparticles (coated in BPE as a test molecule and encapsulated in silica shells), the scattering spectrum and the G_{SERS} profile are strongly uncorrelated, the first one lying up to 200 nm in the blue compared to the second one (see Fig. 4.10). D'Andrea et al. [97] showed that on randomly distributed Au nanoparticles on a SiO_2 substrate, fabricated by electron beam evaporation, the G_{SERS} profile reaches a maximum above 750 nm whereas extinction and scattering peak at about 620 nm and about 750 nm, respectively. This would indicate a good correlation, for this type of samples, between the near-field dispersion and the scattering spectrum, rather than with the extinction one.

Colloidal solutions of metal nanoparticles typically exhibit completely uncorrelated near- and far-field spectra [98–103], with the peak of the G_{SERS} profile strongly

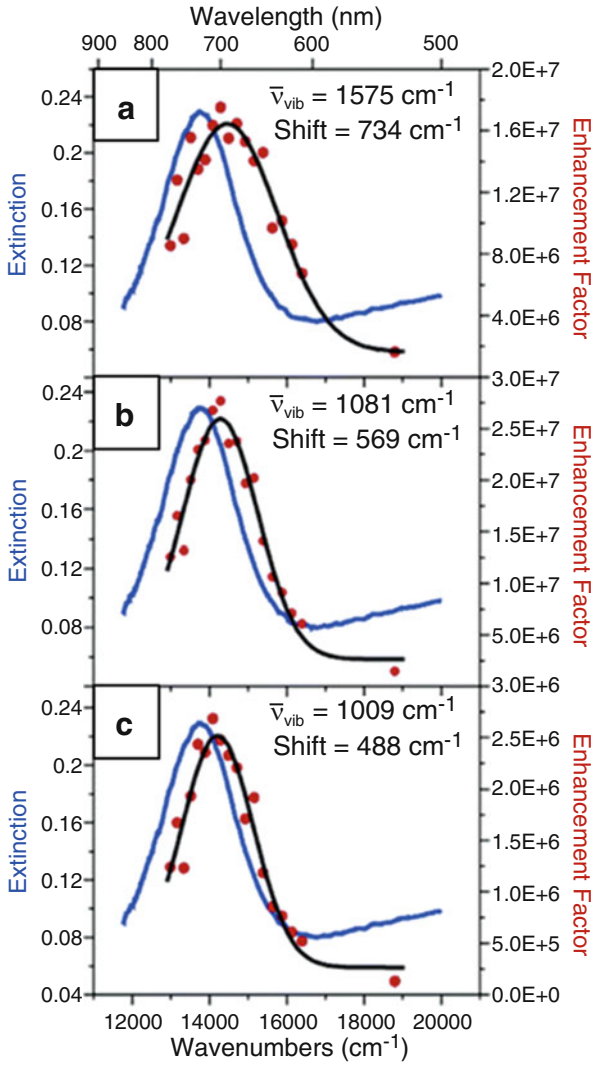

Fig. 4.9 Extinction spectrum (*blue line*) and G_{SERS} wavelength dispersion (experimental points *red dots* and fit *black line*) for the nanotriangle array. From top to bottom, G_{SERS} is calculated with the benzenethiol Raman bands at 1575 cm^{-1} (**a**), 1081 cm^{-1} (**b**), and 1009 cm^{-1} (**c**). The corresponding shifts between the maxima of the extinction and G_{SERS} spectra are 734 cm^{-1}, 569 cm^{-1}, and 488 cm^{-1} (Reproduced with permission from Ref. [73])

redshifted with respect to extinction. This shift arises from the presence in solution of nanoparticle aggregates. Only a small fraction of the nanoparticles in solution is aggregated; hence, the extinction spectrum does not change significantly; however, due to the far better Raman-enhancing capability of aggregates compared to isolated nanoparticles, the SERS signal from the solution is completely dominated by the

contribution from the aggregates. This effect was highlighted in Sect. 4.5 and by Moskovits in Ref. [16].

Further studies on this subject are, for example, the paper by Colas et al. on arrays of nanocylinders [104] and the paper by Zuloaga et al. [105] who used an analytical model, based on a damped harmonic oscillator description of the plasmon, to explain the shift of the near-field maximum, with respect to the far-field one, in metallic nanoparticles.

4.7 Materials for SERS

In order to evaluate the suitability of a material to the fabrication of SERS substrates, we resort to the expression of the electric field that is generated inside a sphere, in the quasi-static approximation, when excited from an external source [60]:

$$E_{\text{in}} = \frac{3\varepsilon_d}{\varepsilon(\omega) + 2\varepsilon_d} E_0 \tag{4.29}$$

$\varepsilon(\omega) = \varepsilon'(\omega) + i\varepsilon''(\omega)$ is the complex dielectric constant of the material that forms the nanoparticle, and ε_d is the real dielectric constant of the (non-absorbing) material in which the nanoparticle is immersed.

When an electric field is applied to a material, positive and negative charges are displaced in opposite directions, leading to a polarization of the material itself.

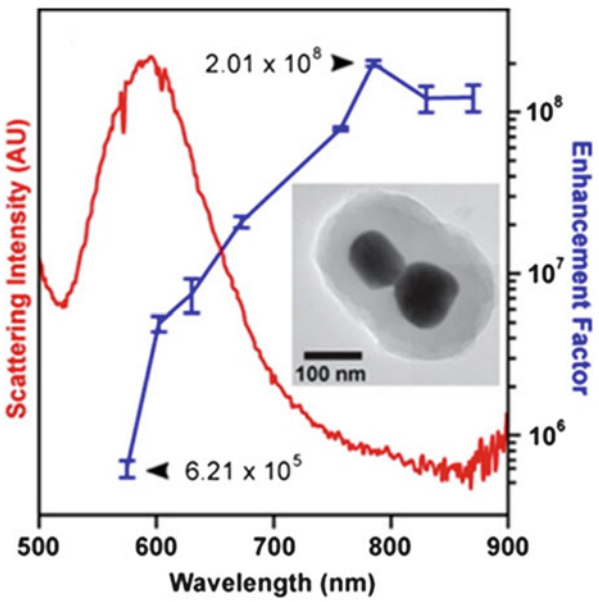

Fig. 4.10 Scattering spectrum (*red line*) and G_{SERS} wavelength dispersion (*blue line*) for the single dimer in the inset (Reproduced with permission from Ref. [17])

The strength of the polarization is represented by the real part, $\varepsilon^{'}(\omega)$, whereas the dissipation processes occurring in the material under the action of the electric field are represented by the imaginary part, $\varepsilon^{''}(\omega)$. Both conduction (free) and bound electrons contribute to the dissipation processes. Conduction electron losses are due to electron-electron scattering, electron–phonon scattering, and scattering of electrons at the surface and at the interface between grain boundaries or with lattice defects. Bound electron losses are due to interband transitions, in which the absorption of photons promotes electrons to higher empty bands [106]. Equation (4.29) shows that E_{in} is very large when the denominator is close to zero (resonance condition). This requirement is fulfilled when $\varepsilon^{'}(\omega) = -2\varepsilon_d$, leading to the following expression for E_{in}:

$$E_{\text{in}} = \frac{3\varepsilon_d}{i\varepsilon''(\omega)} E_0 \tag{4.30}$$

Therefore, to achieve a strong intensification of the field, the dielectric constant of the material that forms the nanoparticle must comply with the two following conditions:

- The real part has to be negative, in order to satisfy the resonance condition $\varepsilon^{'}(\omega) = -2\varepsilon_d$.
- The imaginary part should be small, in order to maximize the electric field in Eq. (4.30).

These features are normally simultaneously encountered in metals, at optical or near-infrared frequencies, as it can be realized by inspecting the expression of their dielectric constant. According to the Drude model, which treats the conduction electrons as a free electron gas, it can be written as [106, 107]:

$$\varepsilon(\omega) = 1 - \frac{\omega_p^2}{\omega(\omega + i\Gamma)} \tag{4.31}$$

The expressions for the real and imaginary parts are the following:

$$\varepsilon'(\omega) = 1 - \frac{\omega_p^2}{\omega^2 + \Gamma^2} \qquad \varepsilon''(\omega) = \frac{\omega_p^2 \Gamma}{\omega(\omega^2 + \Gamma^2)} \tag{4.32}$$

$\omega_p = \sqrt{\frac{ne^2}{m^* \varepsilon_0}}$ is the plasma frequency, n is the density of the conduction electrons, and m^* is their effective optical mass. Γ is the total damping rate that includes all loss mechanisms for conduction electrons mentioned above. From the expression of the real part, it is clear that $\varepsilon^{'}(\omega) < 0$ for $\omega < \omega_p$ and $\varepsilon^{'}(\omega) > 0$ for $\omega > \omega_p$. The plasma frequency for many metals falls in the UV: for example, ω_p for copper, gold, silver, and aluminum is 8.7 eV (142 nm), 8.9 eV (139 nm), 9.2 eV (134 nm), and 12.7 eV (98 nm), respectively [106]. On the other hand, standard dielectrics have $\varepsilon^{'}(\omega) \sim 1 - 10$. This shows that metals, but, in general, not dielectrics, are good

candidates to satisfy the resonance condition of Eq. (4.29) in the visible and infrared spectral regions.

Notice that the Drude model does not account for interband effects: they play an important role in the optical response of the metal when they overlap with the spectral region in which the plasmonic resonance is excited. In the case of silver, the threshold for interband transitions is at 4 eV (310 nm) [108]; therefore, they do not overlap with the plasmonic resonance of silver nanoparticles, located at about 420 nm (for a typical colloid of nanoparticles in water). Conversely, the threshold for Au and Cu is located at about 2 eV (620 nm) [108], partially overlapped with the plasmonic resonance that falls in the range 2–2.5 eV (620–500 nm): this results in a redshift and in a broadening of the plasmonic resonance for Au and Cu, more pronounced for the latter [108]. For aluminum the threshold is at 1.5 eV (800 nm) [106, 108]. It is possible to define quality factors for the plasmon resonance, in order to compare the performance of several materials in a certain frequency range. Quality factors will in general depend both on $\varepsilon^{'}(\omega)$ and on $\varepsilon^{''}(\omega)$, since the former is related to the polarizability and the latter to the losses of the material [106]. For the case of spherical nanoparticles, the following definition can be used:

$$Q_{\mathrm{LSPR}}(\omega) = \frac{-\varepsilon'(\omega)}{\varepsilon''(\omega)} \tag{4.33}$$

Notice that for particles with different shapes, or for surface plasmon polaritons, different definitions are normally adopted [106].

In Fig. 4.11, the real (a) and imaginary (b) parts of the dielectric constant, and the $Q_{\mathrm{LSPR}}(\omega)$ factor (c), are reported for the most important metals used in SERS: the dielectric constants of Ag, Au, and Cu are taken from Ref. [109], and the dielectric constant of Al is taken from Ref. [110]. In addition, Fig. 4.11d summarizes the advisable frequency range of some metals. The following points should be highlighted:

- Metals exhibit a negative dielectric constant in a wide range, allowing the resonance condition $\varepsilon^{'}(\omega) = -2\varepsilon_d$ to be matched in the visible or infrared part of the spectrum (Fig. 4.11a).
- Considering Ag, Au, and Cu, the metal showing the lowest losses in the visible is silver, mainly due to the fact that its interband transitions fall higher in energy compared to the other two materials. Above 600 nm, however, the differences between Ag and the other two metals are remarkably reduced. It is also worth noticing that Al is a good material for SERS with excitation in the ultraviolet (UV), where it maintains a negative $\varepsilon^{'}(\omega)$ and a reasonably low $\varepsilon^{''}(\omega)$ (Fig. 4.11b).
- The values of $Q_{\mathrm{LSPR}}(\omega)$ (Fig. 4.11c) confirm the previous considerations based on the analysis of the imaginary part. The diagram in Fig. 4.11d summarizes the spectral regions in which metals are expected to perform better for SERS: the regions are identified as those in which Q_{LSPR} is above a desired value, set to 5. Results from this analysis are consistent with those presented in Ref. [24].

In addition to the above considerations, based on the capability of efficiently amplifying the electric field, also other features should be taken into account in the use of these materials for SERS: for example, the easiness to work with them, the susceptibility toward oxidation, the stability in the environment in which they are used, and the biocompatibility. Silver and gold cover the vast majority of the present literature because they are air stable; Cu and Al are instead more reactive [24]. The use of Cu in SERS is discussed in Ref. [111, 112] and the use of Al in Ref. [113–115].

Finally, we would like to mention that not only metals but also other materials are currently being studied as alternative plasmonic materials: more specifically, we refer to doped semiconductors as reviewed by Boltasseva et al. [106, 116]. In addition, the use in SERS applications of some dielectric materials, like oxides and chalcogenides, has been extensively discussed by Alessandri et al. in Ref. [117].

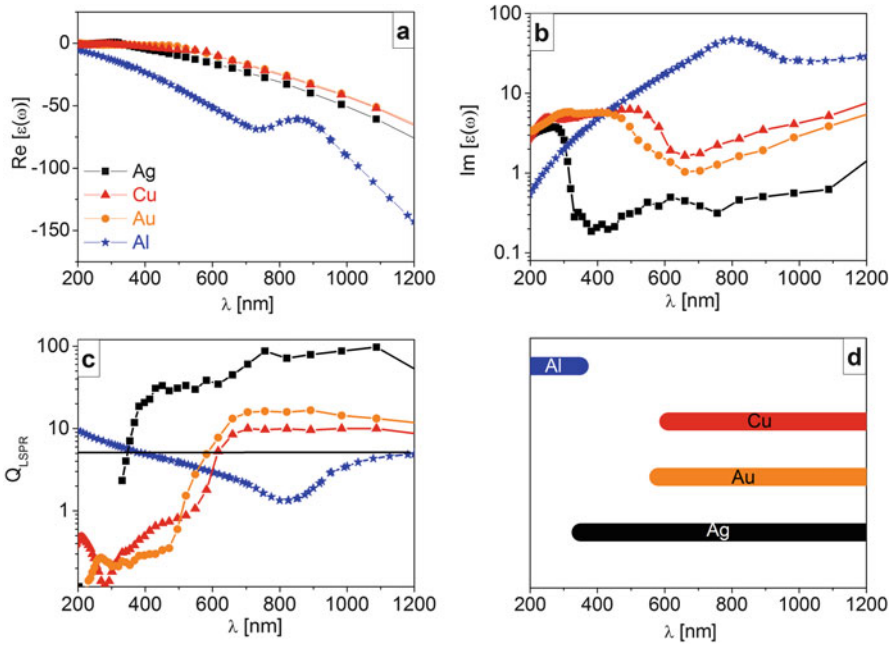

Fig. 4.11 Real part of the dielectric constant (**a**), imaginary part of the dielectric constant (**b**), and quality factor Q_{LSPR} (**c**) for Ag (*black*), Au (*orange*), Cu (*red*), and Al (*blue*), plotted as a function of the wavelength. In panel (**d**), a diagram summarizing the spectral regions in which $Q_{LSPR} > 5$ is reported. The same color code is used in all panels to identify the metals (the figure in panel **d** is inspired from Ref. [24])

4.8 Fabrication of SERS Substrates

The fabrication and optimization of SERS substrates play a crucial role in the development of this technique in several research fields. From an application standpoint, it is important to establish the criteria that a substrate should possess to be considered a "good" SERS substrate. In this respect, we refer to the parameters reported by Natan [118]:

1. Spot to spot reproducibility, <20%
2. Substrate to substrate repeatability, <20%
3. High enhancement factor, $>10^5$
4. Shelf-life stability, a few months conserved in a nonoxidizing atmosphere
5. Large area, a few mm^2
6. Low cost of production

The desired values for parameters 1–3 are taken from Natan's paper [118]; the desired values for parameters 4–5 refer to the typical ones reported for SERS substrates that are currently commercially available.

It is worth highlighting that G_{SERS} is a good indicator of the performance of the substrate; however, the reported values should always be considered with some care for at least two reasons:

1. In the determination of G_{SERS}, the most critical step is the normalization by the number of illuminated molecules on the substrate: an erroneous or a conceptually different evaluation (for instance, one can count only molecules residing in the hot spots or all molecules illuminated in the laser spot) may lead to wide discrepancies in the reported values, making therefore difficult a direct comparison among substrates [119].
2. Considering analytical applications, G_{SERS} is related to the limit of detection, but not in a straightforward way. For example, one may consider two substrates, one with a low density of extremely efficient hot spots and another one that has a large density of hot spots, but with a lower efficiency. If the G_{SERS} value reported is calculated normalizing by the number of molecules present in the hot spots, the first one will provide a higher G_{SERS}. However, the signal-to-noise ratio could be more favorable in the second one, where the higher density of hot spots overcompensates for their lower efficiency.

As a general consideration, it is worth reminding the so-called SERS uncertainty principle [118, 120]:

$$\text{Reproducibility} \quad X \quad G_{SERS} \sim \text{Constant}$$

The principle says that the greater G_{SERS}, the lower the reproducibility of a substrate: therefore, substrates with very high enhancements bring along an intrinsic difficulty in replicating their structure in a reproducible way. This observation originates from the fact that very high enhancements require either very small gaps among metallic

structures or very sharp surface features, in the order of few nm. Such small features can be fabricated, for example, bringing close to contact nanoparticles prepared by colloidal chemistry (bottom-up strategy), but the price to pay is the lack of precise control of the substrate morphology: this in turn causes inhomogeneity issues in large-area substrates and difficulties in replicating identical substrates. Conversely, lithographic methods (top-down strategy) allow a very good control of the morphology, both from point to point on the substrate and from substrate to substrate, but at the present state, 1–2 nm gaps are hardly achievable. Therefore, in order to optimize the performance of a substrate for applications, a compromise between reproducibility and enhancement has to be met [120].

In the following, we shall provide a description of the main fabrication methods and some specific examples of substrates, with a brief discussion of their pros and cons. The methods will be classified in three different categories:

- *Bottom-up methods*: the structure of interest is created by assembling smaller building blocks together.
- *Top-down methods*: the structure of interest is cut out from a bulk material, by removing the material until the desired shape is finally obtained.
- *Template methods*: they fall in between bottom-up and top-down methods; in fact the growth of the template is normally a bottom-up procedure; the deposition of the metal and the partial or total removal of the template are normally a top-down procedure.

Due to the enormous amount of SERS substrates published in the last decades, a detailed review of the whole field would be intractable: therefore, we also refer the interested readers to some excellent reviews [21, 121–133] that, with different focuses, tackle this subject.

4.8.1 Bottom-Up Methods

4.8.1.1 Electrochemical Roughening

This is the first method that was used to prepare SERS-active substrates [1, 2]. It is based on the application of oxidation-reduction cycles (ORC) at metallic electrodes: this procedure causes dissolution of the metal from the electrode to the solution (oxidation) and reduction of the metal ions or complexes from the solution to the surface (reduction), leading to a roughening of the electrode. The SERS performance is optimized by varying the electrochemical parameters [131].

A recent variation of this method is the use of the silver-coated grooves contained in commercial digital versatile disks (DVDs) as electrodes for the electrochemical deposition of nanoparticles and dendrites [132] (see Fig. 4.12).

ORC can produce large-area substrates in a rather cheap way, and G_{SERS} can range in between 10^4 and 10^6; this method has some difficulty in producing uniform

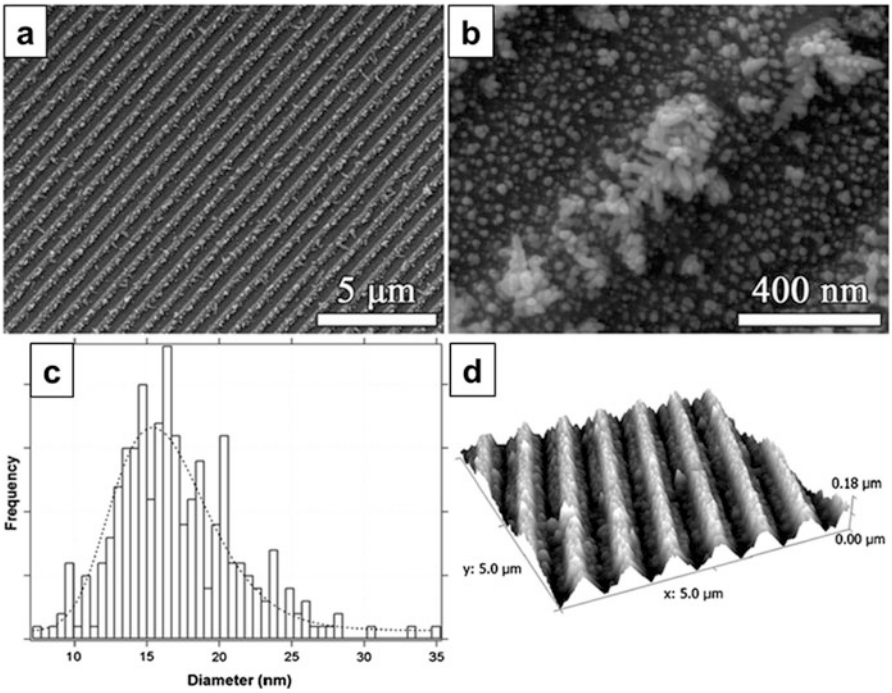

Fig. 4.12 Large-scale (**a**) and close-up (**b**) SEM images of Ag nanoparticles electrochemically deposited on the inner silver surface of a DVD. Distribution of the diameters of the silver nanoparticles within the grooves (**c**) and AFM image of the sample (**d**) (Reproduced with permission from Ref. [132])

surfaces; the fabrication cost is low [133]. Giallongo reported for DVD-based substrate areas ~1 cm^2 and G_{SERS} ~10^5 [132].

4.8.1.2 Assembly of Nanostructures on a Surface

This method was originally developed by Natan et al. [134–137] in 1995 and consists in two steps. First, a solid substrate like silicon, glass, quartz, or indium tin oxide (ITO) is functionalized with a bifunctional molecule able to graft covalently to the substrate and possessing pendant functional groups, typically $-NH_2$, $-SH$, and $-CN$. To this aim, 3-(trimethoxysilyl)propylamine (APTMS) is very often used. In the second step, the functionalized substrate is immersed in a solution containing colloidal nanoparticles: nanoparticles are immobilized at the surface by the pendant groups, forming a bidimensional array. The attachment of the nanoparticles is very strong and de facto irreversible: thiols in solution do not detach them from the surface. Moreover, the background Raman signal from the bifunctional molecule

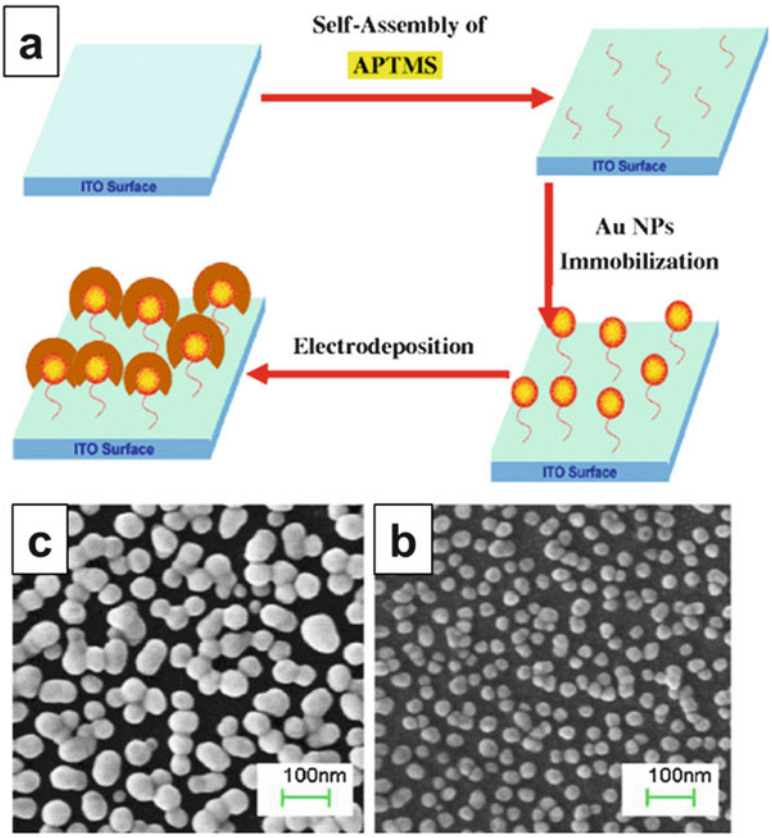

Fig. 4.13 Illustration of the steps involved in the fabrication of SERS substrates by assembly of nanostructures on a surface (**a**); SEM images of the substrate before (**b**) and after (**c**) electrodeposition (Reproduced with permission from Ref. [133])

is very weak due to its low cross section and to the fact that it is placed under the nanoparticles and not in between, where most of the enhancement occurs.

In a recent variation of the method, the deposited nanoparticles can be chemically or electrochemically grown in order to reduce the nanoparticle spacing [133]. This method is illustrated in Fig. 4.13.

Nowadays, a large variety of methods have been proposed to assemble nanoparticles on a surface. In this respect, we mention the reviews by Betz et al. [123] and by Polavarapu et al. [23], which focus on the fabrication of low-cost substrates. Betz et al. [123] describe the deposition of nanoparticle inks on silicon, glass, or paper by means of ink-jet and screen printing technologies; in addition, they also discuss the use of the spontaneous reduction of Ag and Au salts at the surface of suitable materials (galvanic displacement), as a viable method for substrate fabrication.

Polavarapu et al. [23] describe several strategies to impregnate nanoparticles on flexible supports like filter paper, freestanding nanofibers, elastomers, and plastics.

These methods can be used to produce large-area substrates ($\sim cm^2$) [135], with $G_{SERS} \sim 10^4$, as reported by Natan et al. [134].

4.8.1.3 Laser Direct Writing

This method uses a pulsed laser to reduce a silver precursor on a surface, generating Ag nanoparticles that make the surface SERS active. Xu et al. [138] described the application of laser direct writing (LDR) for the fabrication of a SERS substrate at the bottom of a microfluidic channel: the silver precursor (a solution with $AgNO_3$, trisodium citrate, and ammonia), inside the micro-fluidic channel, was irradiated with a femtosecond laser focused through the objective of a microscope. The SERS substrate was written by scanning the laser spot position in the micro-fluidic channel. Figure 4.14 illustrates the procedure.

Analogous strategies were used to write 3D structures by two-photon photoreduction of an Au precursor [139] and to convert an AgO_x thin film, deposited on a glass substrate, into aggregated Ag nanoparticles by means of a femtosecond laser [140].

The main advantage of this method is that the substrate can be directly written where necessary; concerning G_{SERS}, Xu et al. reported a value of about 10^8 [138], Izquierdo-Lorenzo et al. reported about 10^6 for the 3D microstructures [139], and Tseng et al. reported about 10^8 for the aggregated Ag nanostructures [140].

4.8.2 Template Methods

4.8.2.1 Anodic Aluminum Oxide Template

Anodic aluminum oxide (AAO) is a self-organized structure, possessing a closed packed array of hexagonal cells: uniformly sized cylindrical channels are present at the center of every cell [141]. This template can be used to fabricate a regular array of vertically aligned nanorods. The whole fabrication process is summarized in Fig. 4.15 and consists of several steps [142]: (a) polishing of the substrate; (b) electrochemical anodization, which produces the close-packed hexagonal array of nanopores; (c) pore opening, which consists in a controlled etching of the honeycomb structure, in order to tune the barrier between the pores; (d) electrochemical deposition of a metal inside the pores; (e) etching the upper part of the AAO structure, in order to expose (partly or completely) the metallic rods; and (f) the hexagonal array of vertically aligned nanorods is obtained: it is characterized by the parameters S, D, and W that are the center-to-center distance between nanoparticles, the nanoparticle diameter, and the interparticle gap, respectively. Importantly for SERS, the gap between the pores is tunable and can be varied between 5 and 25 nm.

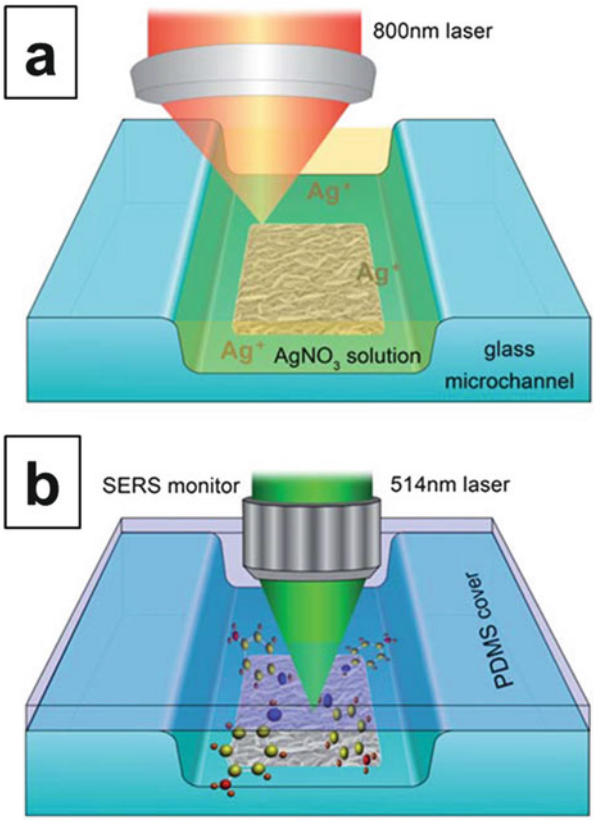

Fig. 4.14 (**a**) A femtosecond laser is used to write the SERS substrate at the bottom of a microfluidic channel by reduction of a silver precursor. (**b**) The SERS substrate is used to monitor the presence of analytes in the microfluidic channel (Reproduced with permission from Ref. [138])

The nature of the metal to be deposited in the pores can be easily chosen, and the production cost is rather low.

These substrates are fabricated and discussed, for example, in the papers by Giallongo et al. [143], Jeong et al. [144], Das et al. [145], and Toccafondi et al. [146]. The AAO template method is suitable for the fabrication of large-area substrates (200 mm^2 in Ref. [143]); concerning the SERS enhancement, Das reported a G_{SERS} $\sim 10^3$–10^4 [145] and Giallongo [143] and Wang [142] measured G_{SERS} $\sim 10^4$ and $\sim 10^5$, respectively.

4.8.2.2 Nanosphere Lithography

Nanosphere lithography (NSL) is a fabrication method that has been thoroughly developed and popularized by Haynes [147] and that allows one to produce periodic

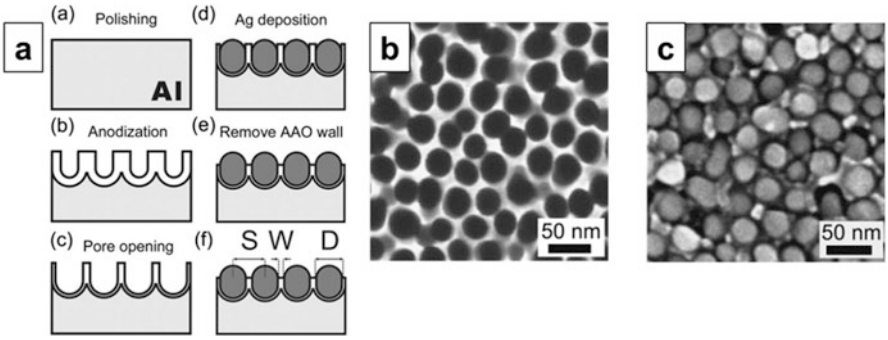

Fig. 4.15 (**a**) Sketch of the steps involved in the fabrication of the AAO substrates. Top-view SEM image of an AAO substrate with D = 25 nm and W = 5 nm, before (**b**) and after (**c**) the growth of Ag nanoparticles (Reproduced with permission from Ref. [142])

arrays of metallic nanostructures on surfaces. The first step is the deposition of a single layer of silica or latex nanospheres on an appropriate surface: under controlled experimental conditions, the nanospheres self-organize into a hexagonal close-packed structure. This array possesses triangular void spaces, in turn arranged in a hexagonal pattern, corresponding to the interstices among three neighboring nanoparticles and can be used as a mask to produce two types of substrates [22, 82]:

- *Metal films over nanospheres (M-FON)*. In this case, a metal layer (∼200 nm) is deposited directly onto the nanosphere mask [80, 148].
- *Hexagonal array of nanotriangles*. A layer of about 15–100 nm of metal is deposited on the mask: the removal of the mask generates a periodic, hexagonal array of nanotriangles [73].

In Fig. 4.16, the fabrication procedure is summarized. Nanotriangles exhibit a well-defined surface plasmon resonance that can be determined by the extinction spectrum. M-FONs instead present a broader and less defined spectrum that can be measured in diffuse reflectance: their SERS activity mainly originates from the roughness of the deposited metal film [1, 80, 149]. The near- and far-field optical response of nanotriangle arrays can be tuned from the visible to the NIR by varying several experimental parameters like the size of the polystyrene spheres, the thickness of the metal, and the angle of metal deposition; annealing can also be used to reshape the nanotriangles into more roundish nanoparticles.

Reported G_{SERS} are around 10^6–10^7 [73, 74] for nanotriangles and around 10^6 for Au-FON [150]. This procedure yields large-area patterned substrates (order of cm^2): the typical area of the ordered domains extends up to several hundreds of μm^2 [74]. A disadvantage is that the fabrication processes are very sensitive to the experimental conditions, which should be therefore strictly controlled.

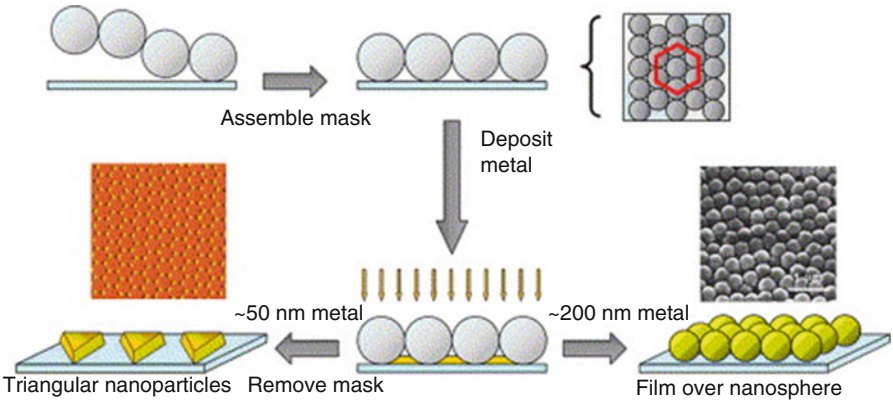

Fig. 4.16 Steps involved in the fabrication of nanotriangle arrays and metal films over nanosphere substrates (Reproduced with permission from Ref. [149])

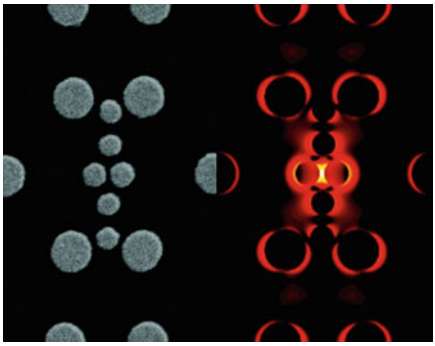

Fig. 4.17 SEM image (*left*) and near-field simulations (*right*) of genetically engineered SERS substrates (Reproduced with permission from Ref. [151])

4.8.3 Top-Down Methods

4.8.3.1 Electron Beam Lithography

In electron beam lithography (EBL), a tightly focused electron beam is scanned across a radiation-sensitive polymer (resist), making it either more or less soluble in a developer solution. The exposed or non-exposed polymer can then be selectively removed to generate nanostructures with a well-controlled geometry and sub-20 nm resolution. The subsequent deposition of metal allows the fabrication of a plasmonic-active substrate [22].

For example, Forestiere et al. [151] designed a metallic nanoparticle array with large enhancement, by making use of simulations based on a genetic algorithm. The optimization procedure was experimentally validated by fabricating the substrate with EBL and testing the enhancement by SERS. The reported values of G_{SERS} were in the range 10^4–10^5; a SEM image of the genetic nanoarray and of the simulated field intensity is reported in Fig. 4.17.

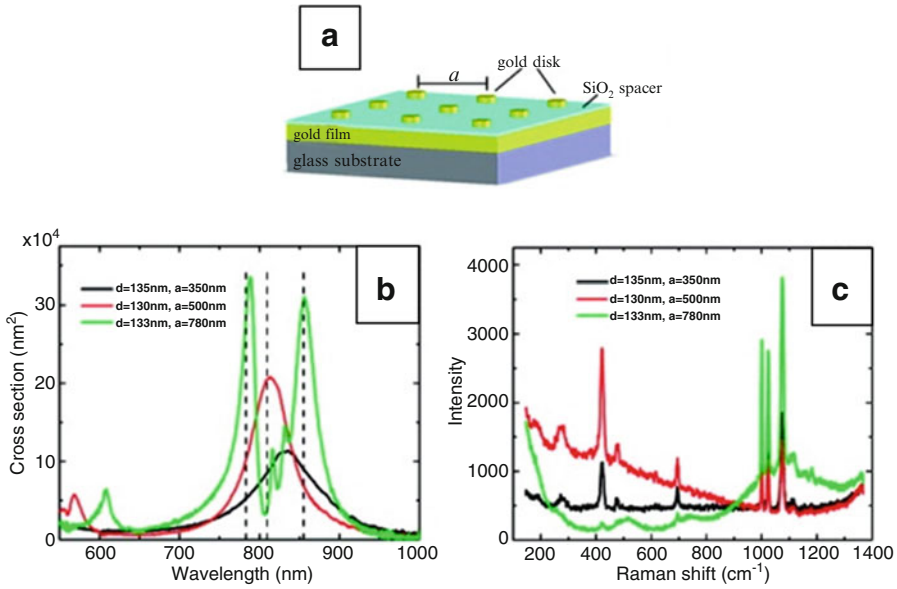

Fig. 4.18 Illustration of the gold disk array (**a**), extinction cross section (**b**), and SERS spectra (**c**) of substrates with different diameters (*d*) and periodicity (*a*) (Reproduced with permission from Ref. [160])

Another example is the engineering of a substrate in order to optimize the enhancement of both the laser and the Raman scattering frequencies [152]. Chu et al. optimized by simulations, and fabricated by EBL, a substrate formed by three layers: a 100-nm-thick gold film, a SiO_2 spacer, and a square gold disk array (Fig. 4.18a); the array period (*a*) and the diameter of the disks (*d*) were varied to optimize the enhancement of the structure. In Fig. 4.18, a sketch of the substrates, the extinction spectra measured for different combinations of *d* and *a*, and the corresponding SERS spectra are shown. Figure 4.18 evidences that the array resonant both at the laser and at the Raman wavelengths (green line in Fig. 4.18b) is the one that exhibits the largest SERS signal (green line in Fig. 4.18c), with a reported G_{SERS} of about 10^8.

Other examples comprise the fabrication of arrays of nanocylinders [104], nanoslits [30], nanoparticles [69, 95], nanoparticle cluster arrays [153], and plasmonic nanofocusing structures [154].

The main advantage of EBL is the possibility of fabricating ordered, homogeneous, and repeatable substrates in which the shape and size of the features can be finely controlled. EBL is very useful to establish structure-property relations since it allows one to fabricate substrates designed and optimized by theoretical calculation. The main disadvantage of EBL is the serial writing process that makes this technique unfavorable for the fabrication of large-area and low-cost substrates. Moreover, it is difficult to routinely obtain gaps below 10 nm [22].

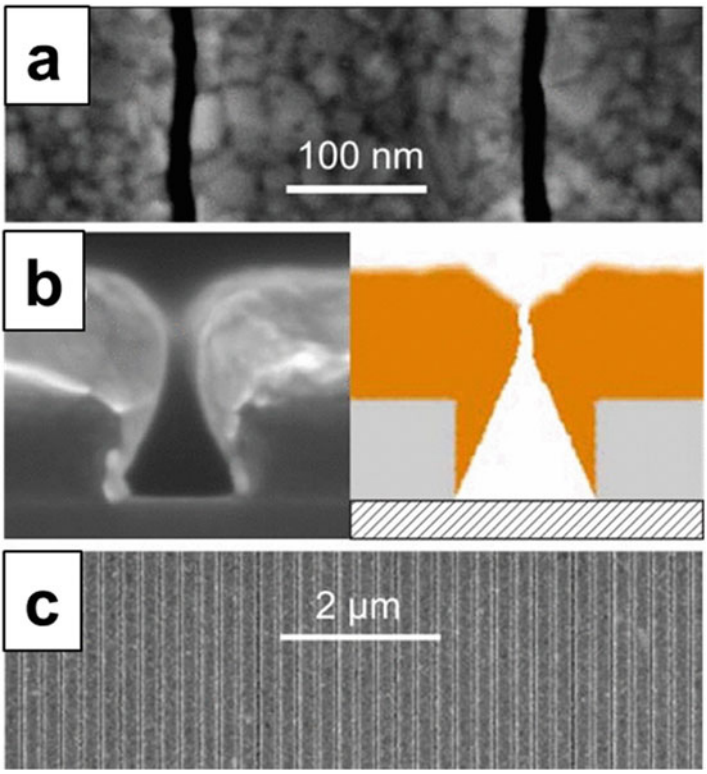

Fig. 4.19 (**a**, **c**) Top-view SEM image of the gold nanogap array. (**b**) Cross-sectional view of a cleaved array (*left*) and comparison with ballistic simulations (*right*) (Reproduced with permission from Ref. [155])

4.8.3.2 Extreme Ultraviolet Interference Lithography

In extreme ultraviolet interference lithography (EUV-IL), the steps followed are similar to the ones already described for EBL, except for the fact that the pattern on the photoresist is written by exploiting the interference of coherent synchrotron light beams ($\lambda = 13.5$ nm) [155].

Siegfried et al. [155] reported on the fabrication of substrates with an area larger than 1 mm^2, gap sizes around 10 nm, and G_{SERS} of about 10^6. In Fig. 4.19, the top view of the substrate is shown in A and C; in B the cross-sectional view of the gap, about 13 nm wide, is shown. Although interference lithography is a well-established method for nanofabrication, the use of synchrotron radiation, in order to improve resolution, is of course a very peculiar aspect. The gap size that can be achieved is in this case comparable to the one of EBL, with the advantage that larger areas can be patterned.

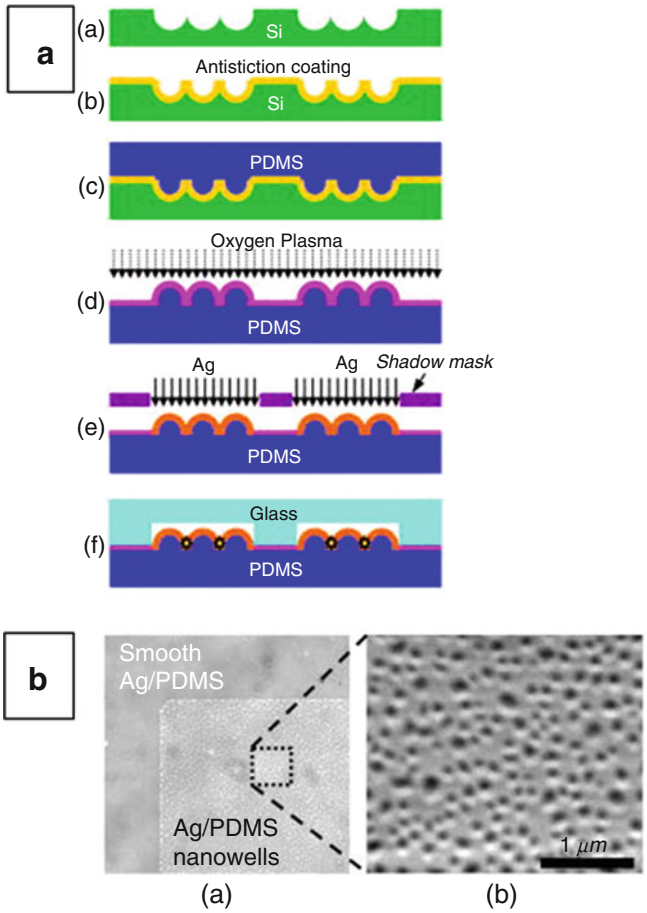

Fig. 4.20 (**a**) Illustration of the steps involved in the fabrication of a nanowell substrate by soft lithography. (**b**) SEM image of the Ag layer (Reproduced with permission from Ref. [160])

4.8.3.3 Soft Lithography

Another method that can be used to fabricate SERS substrates encompasses the use of the so-called soft lithography methods [156–158]. They use elastomeric stamps, molds, and conformable photomasks for patterning two- and three-dimensional structures with minimum feature sizes on the nanometer scale.

An example of fabrication of SERS substrates by soft lithography is illustrated in Fig. 4.20a, from Ref. [159]. The following steps are involved: (a) fabrication of a master (nanopillar array) with conventional lithography and etching methods on silicon, (b) antistiction coating of the master mold, (c) soft lithography of the nanowells with polydimethylsiloxane (PDMS), (d) oxygen plasma treatment of the surface, (e) deposition of an Ag layer through a shadow mask (shown in Fig.

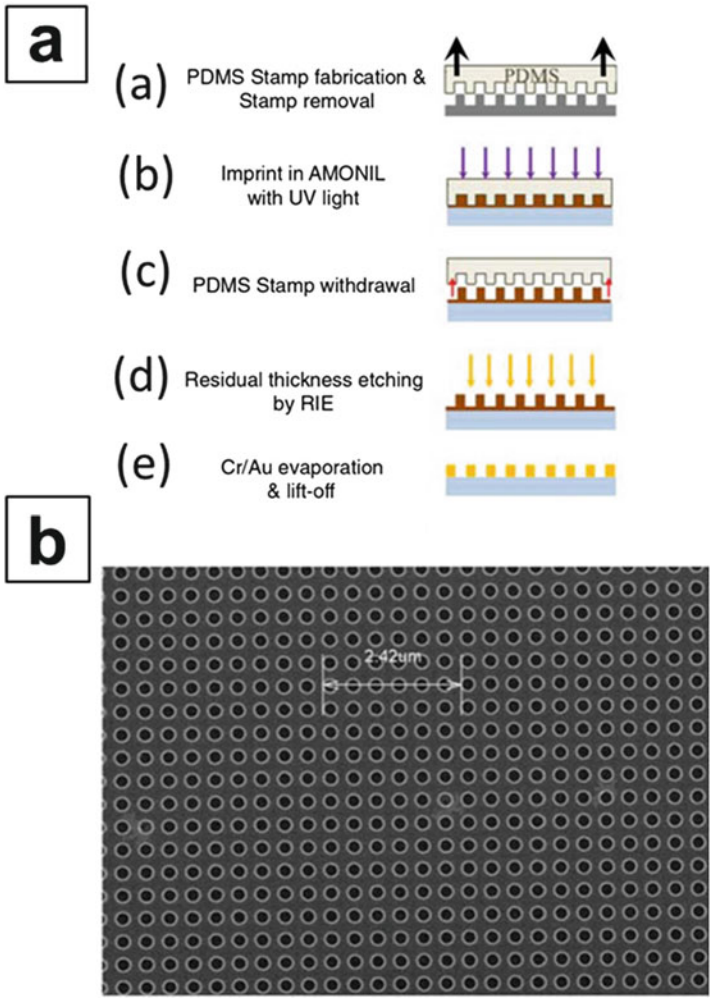

Fig. 4.21 (**a**) Steps involved in the fabrication of SERS substrates by soft lithography. (**b**) SEM image of the silicon master mold (Reproduced from Ref. [160] (open access))

4.20b), and (f) integration of the substrate in the glass microfluidic channels. The microfluidic integrated SERS substrate was tested for the detection of rhodamine 6G and adenosine.

In another interesting example, Cottat et al. [160] used soft UV nanoimprint lithography to fabricate SERS substrates: the steps involved are illustrated in Fig. 4.21a. A master mold was fabricated by writing a pattern on poly(methyl methacrylate) (PMMA) by EBL and transferring it on silicon by reactive-ion etching (RIE): a SEM image of the master mold is represented in Fig. 4.21b. Subsequently, (a) a PDMS stamp was created from the master; (b) the PDMS stamp was used

to imprint the pattern on the AMONIL resist (AMO GmbH, Aachen, Germany), subsequently polymerized by UV exposure; (c) the PDMS stamp was removed; (d) the residual AMONIL at the basis of the holes was eliminated by RIE; and (e) a metal layer of Cr was deposited as an adhesion layer, and then the Au layer was deposited to produce the array of metallic nanocylinders. Other examples can be found in the papers by Picciolini et al. [161] and Kahraman et al. [162].

Soft lithography can produce large-area substrates (up to cm^2) [158], at a low cost of production. The G_{SERS} reported by Cottat et al. [160] for an array of nanocylinders is about $3 \cdot 10^7$; Piccioli et al. [161], for a polymer nanopillar array, covered with Au nanoparticles, reported G_{SERS} of about 10^4; Liu et al. [159] and Kahraman et al. [162] measured G_{SERS} of about 10^7 and 10^6 for a nanowell and a nanovoid array, respectively [21].

4.9 Applications

The research area in which SERS has found the largest number of applications is the area of sensing, which comprises very different fields like medicine, forensic science, environmental monitoring, and art preservation. We highlight that this broad range of applications has significantly benefited from the realization of portable Raman spectrometers that can be used not only in laboratory but also in real field assays. Miniaturization and portability of Raman instruments have been pursued, together with the testing of new substrates for sensing, to reduce the cost, increase the speed of analysis, simplify the operation, and realize the applications of analytical measurements in real field other than in the traditional laboratory. It is also worth mentioning that an important problem in analytical SERS applications is the decomposition of molecules at the surface of the substrates (due to overheating or catalytic activity of the substrates themselves) that results in the formation of carbonaceous materials. They are characterized by broad Raman bands at about 1350 cm^{-1} (D band), 1580 cm^{-1} (G band), and 1500 cm^{-1} (amorphous carbon) [163] that often appear in the spectra as fluctuating contributions difficult to identify and subtract [164]. Some strategies that can be used to minimize such effects are, for instance, raster scanning the laser spot on the sample, using large-area laser spots and finding the best trade-off between the laser intensity and the integration time [123, 128, 165].

The goal of this section is to provide a clear overview of the fields in which SERS sensing is widely employed and to identify potential new areas of research that could benefit from the high sensitivity, selectivity, multiplexing power, and simplicity of use that this technique enables. Several highly focused reviews are also available [24, 166–168], and the readers are encouraged to refer to them for more in-depth details. Before we delve into the various applications, it is important to specify that two fundamental approaches to SERS sensing platforms exist, namely, the direct and the indirect (in some cases known as *sandwich*): they are illustrated in Fig. 4.22. Direct sensing is based on the ability of the substrate

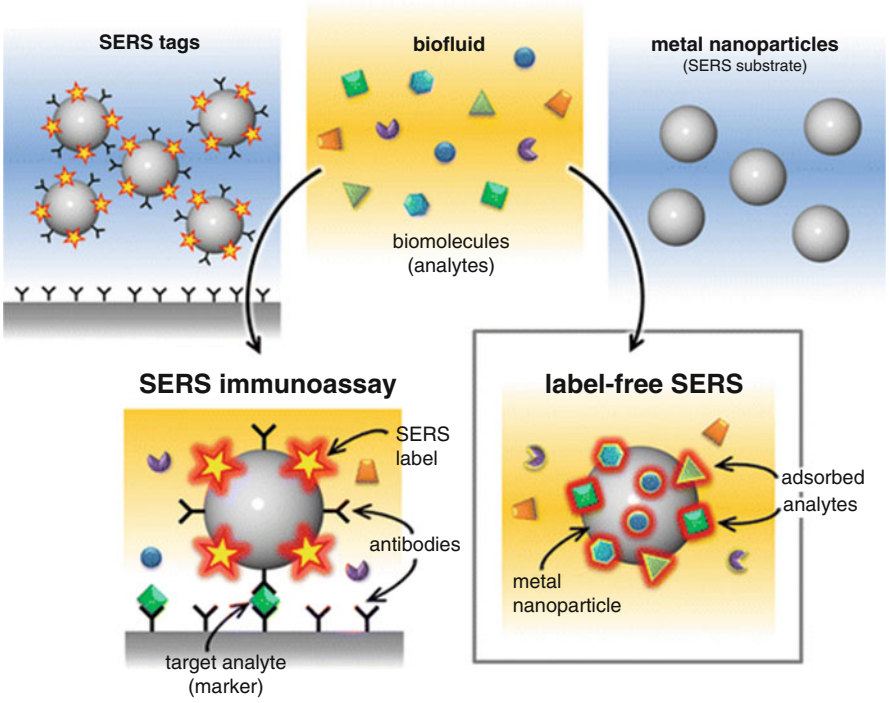

Fig. 4.22 Direct and indirect scheme of detection for SERS. In the direct protocol, the SERS signal originates from all analytes which adsorb on the substrate. In the indirect protocol, the signal originates from the labels on a SERS tag specifically bound to the target analyte (Reproduced with permission from Ref. [168])

to detect the presence of analytes by directly recognizing fingerprinting modes that can be assigned to the molecular structure of the molecule sought. These platforms, easy to use and generally providing high G_{SERS} [169], are however limited to the identification of simple analytes with high Raman cross sections. Analytes that can be readily identified with these platforms are, for instance, small molecules, explosives, or contaminants. Complex biomolecules on the other hand, such as proteins or long oligonucleotide strands, cannot in general be unequivocally identified following direct protocols and require indirect methods. In an indirect platform [170], the SERS substrate is functionalized with a targeting moiety, such as an antibody, an aptamer, or a complementary DNA or RNA strand, whose role is to selectively recognize and capture the analyte. Detection of the analyte will then be carried out with secondary SERS tagging moieties (i.e., SERS tags) [171] or by virtue of the enhancement of the SERS signal of a reporter molecule bound to the targeting moiety [172]. If cleverly designed, both methods can provide high sensitivity (down to attomolar concentrations) and selectivity. Both of them, however, suffer from matrix effects that arise in the presence of complex mixtures, such as biological fluids (blood, saliva, or urine) or cell membranes (made of

Raman-active phospholipids [25] and studded with numerous proteins). In these cases, the user needs to critically determine whether a direct or indirect approach is more suitable. For instance, if using a direct approach, it is important to determine if all the molecules in the matrix can be identified or if a targeted, sandwich approach is necessary to isolate only the analyte out of the mixture. On the other hand, in using an indirect method, one should determine whether the added complexity intrinsic to the sandwich architecture, the added costs, and the increased performance time are justified in cases of not-too-complex matrices whose Raman resonances can be clearly isolated from those of the analytes.

In the following sections, we shall illustrate several fields of application of SERS, with specific examples, focusing on the direct detection protocols.

4.9.1 Chemical Warfare Agents and Explosives

The identification of chemical warfare agents (CWAs) and explosives is nowadays a crucial issue for homeland security: the possibility of detecting chemical contaminants quickly and on-site is essential to allow a prompt activation of appropriate emergency responses, such as decontamination or administration of an antidote.

The SERS detection of 2-chloroethyl ethyl sulfide (CEES), a simulant for HD mustard (2,2 dichloroethyl sulfide), has been carried out by using Ag SERS substrates fabricated by NSL, as described in Ref. [35]. SERS spectra of CEES have been measured with a field-portable spectrometer at concentrations well below hazardous levels, after a 24-h exposure of the sample and with a 5-s acquisition time. SERS has also been used for the sensitive detection of femtomolar quantities of two nerve gases, VX and tabun, in water, using substrates consisting of flexible gold-covered Si nanopillars realized by lithographic methods. VX and tabun have been revealed with detection limits of ∼13 and ∼670 femtomolar, respectively [173].

The chemical vapor signature emanating from buried TNT-based landmines, 2,4-dinitrotoluene (DNT), has been detected by using gold SERS substrates prepared by electrochemical roughening [36]. DNT was detected at concentration levels of about 5 ppb, (using acquisition times of 30 s) on a fieldable system. Groundwater monitoring of explosives is also a relevant topic, especially in proximity of military ammunition sites. In this context, Xu et al. [174] have studied the detection of DNT from the liquid phase. As a SERS substrate, the authors used triangular gold nanoprisms, fabricated via a modified seed-mediated method and decorated with cyclodextrins (CDs). In order to improve the performance of the substrate, the distance between the explosive molecule and the metallic surface was controlled using short alkyl chains. Besides, the cavity diameter of CD (0.78 nm) was chosen to match the DNT size (0.7 nm). The hydrophobic CD cavity was selective to the molecular structure of the explosive agent. For example, CD did not capture the picric acid; nitrobenzene instead, affine to the cavity, could be detected. The detection limit was quantified at the sub-ppb level for DNT. Further studies on the detection of explosives can be found in a recent review [175].

4.9.2 Environmental Analysis of Pollutants

The environmental analysis and monitoring are strictly related to the individuation of small traces of pollutants (such as polyatomic anions, heavy metal ions, and organic compounds) present in the atmosphere or in the water of soil, rivers, and lakes [176, 177].

Polyatomic anions like perchlorate, chromate, dichromate, cyanide, nitrate, sulfate, and phosphate are contaminants that can impact the local ecosystem, groundwater, and human health. The presence in aqueous environments of nitrate and sulfate anions has been studied using Ag and Au plasmonic substrates coated with cationic thiols, like cysteamine hydrochloride and dimethylaminoethanethiol hydrochloride, in order to increase the affinity of the analyte to the SERS substrate surface: nitrate and sulfate have been detected at levels of 10 ppm and 100 ppm, respectively [178]. In another paper, cationic thiol-coated SERS substrates have been tested also to detect perchlorate, chromate, dichromate, and cyanide, obtaining detection limits in the ppb–ppm concentration range [179]; the lowest level of sensitivity could be obtained only through a pre-concentration process based on a bifunctional anion-exchange resin [180]. Since the adsorption of anions onto the cationic coatings has been shown to be an instantaneous and reversible process, this technology is attractive for continuous and real-time monitoring of these anionic species.

Heavy metal compounds, such as CdSe, ZnO, and HgS [181], have been detected using SERS inkjet-printed substrates, designed and employed by Eshkeiti et al. [181], while arsenic species in water were detected by Du et al. in real groundwater samples using a portable Fe_3O_4@Ag sensor with limits of detection as low as 10 μg/L [182]. Other important ions, such as Cr(VI) [183] and uranyl [184], were recently identified in water using SERS. Uranyl, in particular, is of particular interest as its presence is indicative of radioactive residues in the ground or water.

Besides the heavy metal contaminants, certain small molecules pose significant threat to human and animal health. One category of such pollutants is that of aromatic molecules, such as naphthalene. A quantitative SERS sensor for the detection of naphthalene in water was developed by Peron et al. [185]. In their method, the authors functionalized quartz substrates with polystyrene beads coated by gold nanoparticles and were able to detect the aromatic molecule quantitatively in the range of 1–20 ppm. Polycyclic aromatic molecules were instead detected in the gas phase by Fery and coworkers [186], who used poly-N-isopropylacrylamide (p-NIPAM)-coated gold nanostars deposited on a glass slide to detect various aromatic hydrocarbons in gas. Camden and coworkers focused instead on the identification of hydrazine, a molecule that, despite being commonly used in various industrial processes, can be lethally dangerous to the kidneys, liver, and central nervous system after acute exposure [187].

4.9.3 Art Preservation

In the field of art preservation, it is of paramount importance to achieve the ultrasensitive detection of natural and synthetic dyestuffs. The identification of specific colorants can be of benefit for the long-term preservation of artworks, and in addition, it can unveil their historical context and eventual forgeries. Moreover, the nondestructive nature of Raman spectroscopy and its very high sensitivity minimize the quantity of material that might be necessary to uptake from artworks for analysis: this makes SERS an ideal tool in art preservation, as illustrated in the following examples.

The successful detection of small amounts of biomolecules in aged and complex matrices, like archeological objects, faded pastels, and glaze layers in paintings, has been reported in Ref. [44, 188]. Silver island films and Ag-FONs were used as SERS substrates. Sample uptake, for SERS experiments, was kept at minimum, in the sub-μg to pg range: Raman spectra were recorded starting from samples as small as a single grain of pigment or a micrometer fragment of a dyed fiber, as reported in Fig. 4.23. The identification of dyes in pigments was accomplished by comparing the experimental spectrum with the spectra reported in a dedicated database [24, 44].

Recently, also tip-enhanced Raman spectroscopy (TERS) has been tested as a spectroscopic tool for the compositional characterization of colorants in artworks in situ, directly on historical materials, with a minimally invasive procedure [189]. TERS is a powerful technique that combines the sensitivity of SERS and the precise spatial control and resolution of scanning probe microscopy via a nanometer-scale noble metal scanning tip. A properly designed AFM-TERS instrument has been used to identify the presence of iron gall ink on a single paper fiber belonging to a nineteenth-century historical manuscript (Fig. 4.24). TERS allowed a fast and nondestructive analysis, avoiding any damage or photodegradation to the dyed paper.

Further studies can be found in specialized reviews on this subject [190, 191]. They illustrate, from different standpoints, advancements in the instrumentation, sampling procedures, and analytical protocols. They also discuss how issues like the analysis of irreplaceable objects (quasi-nondestructive sampling), spatial resolution, examination of insoluble compounds, and resolution of dye mixtures have been practically solved. A number of examples, regarding the determination of the original constituent materials, degradation, or conservation products in artworks, are provided as well.

4.9.4 Food Contaminants

The analysis of food by SERS is carried out by both the producer's and the consumer's sides. On one hand, producers are concerned with the quality of their product and are required to follow specific prescriptive standards before introduction

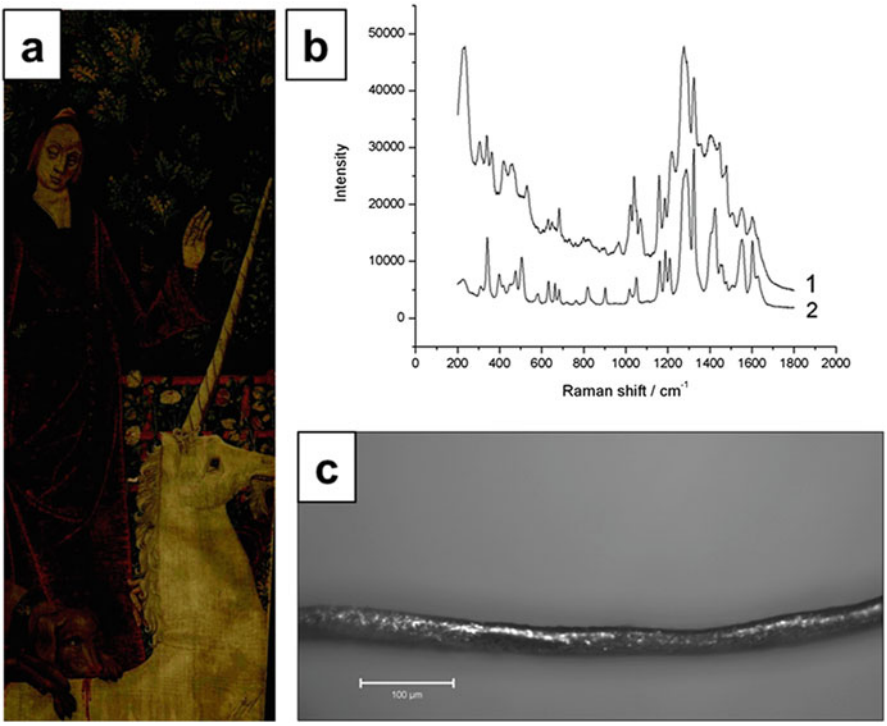

Fig. 4.23 (**a**) A sixteenth-century Netherlandish tapestry ("The maiden's companion signals to the hunters," from "The hunt of the unicorn" series; South Netherlandish, ca. 1495–1505. The Metropolitan Museum of Art, 38.51,1.2; Gift of John D. Rockefeller, Jr., 1937). (**b**) Raman spectra, recorded by focusing the laser beam on the wool fiber covered with silver (*line 1*), demonstrating the presence of alizarin (*line 2*). (**c**) Single wool fiber was removed from tapestry to be analyzed (Reproduced with permission from Ref. [44])

to the market. For instance, in order to respect the standards in vegetable oil quality and ensure that the lipids in the oil are still of good quality after processing, the amount of α-tocopherol cannot fall below certain thresholds. Lu and coworkers used molecularly imprinted polymers (MIPs) to study four types of vegetable oil for the identification of α-tocopherol in less than 15 min [192]. On the other hand, consumers are also interested in determining the quality of the food they eat and the absence of residual pesticides and want to ensure that illegal additives (such as melamine in infant formula) are not present. Therefore, it is clear that the SERS analytical community has been very active in the identification of sensing protocols for the detection of various relevant analytes.

Substrates constituted by vertically aligned nanorods with inter-nanoparticle gaps of ca. 0.8 nm were employed by Xiong and coworkers for the detection of plasticizers and melamine in orange juice with 0.9 fM limit of detection (LOD), a

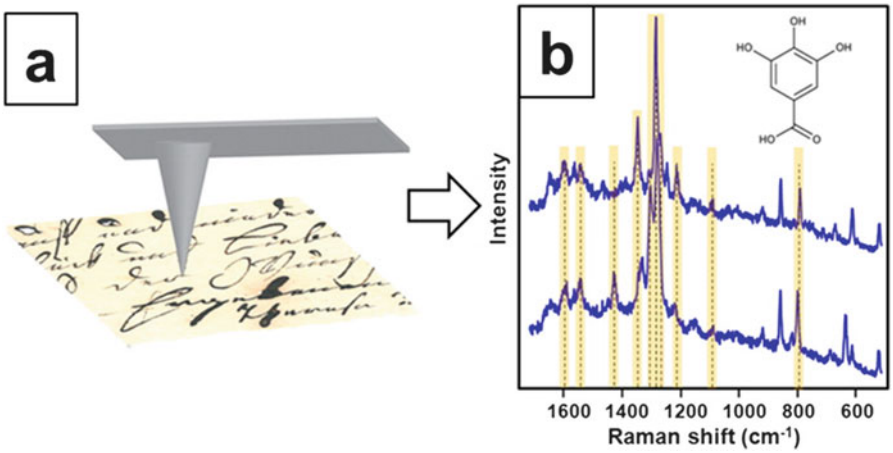

Fig. 4.24 (**a**) Micrograph of a nineteenth-century historical paper, analyzed with a TERS probe. (**b**) TER spectra of an iron gall ink spot, acquired using $\lambda_{exc} = 532$ nm, $t_{acq} = 4$ s, and $P_{exc} \approx 0.36$ mW. Structure of the gallic acid (3,4,5-trihydroxy-benzoic acid): reacting with Fe(III), it forms gall iron ink (Reproduced with permission from Ref. [189])

value that is significantly lower than the limits of 6 ppb prescribed in the United States [193].

Gold nanoparticles assembled via the use of thiolated polyethylene glycol (SH-PEG) have been used by Zhou et al. to identify various food pesticides in traces (10^{-10} M) [194], while Hu and coworkers used a gold nanoparticle-decorated polymer to pre-concentrate and identify residual pesticides in orange peels [195]. In a recent study, Zhu et al. [196] determined the presence of food colorants, namely, lemon yellow and sunset yellow, at the concentration of about 10^{-5} M: the authors fabricated the SERS substrate by depositing silver nanoparticles on a filter paper and functionalizing them with a charged electrolyte. Polystyrene/Ag nanoparticles have been used as SERS substrates for the sensitive detection of low levels of two organophosphorus pesticides, paraoxon and sumithion, in solution. These pesticides have been detected in the low nM range, reaching a LOD of 96 nM (0.026 ppm) and 34 nM (0.011 ppm), respectively, with an acquisition time of about 600 s [197]. In a different work, silver nanoparticles have been deposited on commercially available low-cost filter paper in a large scale and utilized for the detection of thiram and paraoxon residues at various peels [198]. Paper substrates were also used to collect pesticide residues by simply swabbing the paper substrate across a wide-area surface of peels (Fig. 4.25). Measurements performed on thiram and paraoxon residues at various peels (such as apples, bananas, and tomatoes) showed a detection limit of 7.2 ng/cm^2 and 0.23 μg/cm^2, respectively. Hu et al. [199] described the SERS detection of methyl parathion in water, with a limit of detection of 1 nM, using an ordered array of multi-shell spheroidal nanoparticles as a SERS substrate.

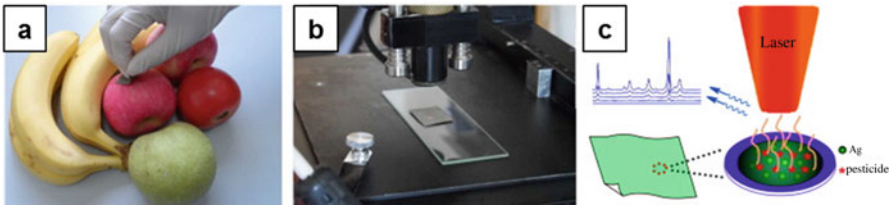

Fig. 4.25 (**a**) Sample collection process of pesticides at a peel with an Ag nanoparticle-decorated filter paper. (**b**) Detection with a portable Raman system. (**c**) Schematic drawing for the detection of pesticides with SERS technique (Reproduced with permission from Ref. [198])

4.9.5 Biomolecules

The detection of molecules of biological nature, i.e., biomolecules, is carried out with sensing platforms generally known as *biosensors*. SERS-based biosensors have been the focus of intense research for quite some time, and it is perhaps their rapid growth over the past decade the factor that has made it possible for SERS to become as relevant as it is now. In the following paragraphs, we will provide a brief overview of the most common targets, but the interested readers should refer to more in-depth reviews [25, 166, 200]. The most important targets in SERS biodetection are oligonucleotides, proteins, and other small molecule metabolites. In general, besides few exceptions, biodetection is carried out following the indirect approach, in which the SERS substrate is functionalized with a targeting moiety, such as an aptamer, antibody, or single-stranded oligonucleotide, which is responsible for recognition and capture of the analyte. Following analyte capture, the substrate is exposed to a solution of a secondary reporter, often a plasmonic nanoparticle functionalized with a Raman-active molecule. The secondary reporter, also known as SERS tag, also carries an additional recognition moiety, capable to bind to the target molecule in a sandwich fashion. If the target is present and identified, the location in which it has been captured will appear bright in a SERS map, similar to what is observed in fluorescent DNA microarrays. Logically, numerous variations exist to this proposed scheme; however, all of them have in common (1) the use of a targeting moiety specific for the target and (2) one or more Raman reporter molecules that *light up* in a SERS map as an indication of target recognition. In general, SERS biosensors have linear dynamic ranges of up to five orders of magnitude in concentration, are designed for *signal on* recognition, and should not necessitate target labeling.

4.9.5.1 Oligonucleotides

Oligonucleotide detection is one of the most traditional applications of SERS biosensors. The large majority of them are carried out without target labeling, but until recently, they could not identify the individual nucleotides in the sequence, due to the complexity of the signals and limited cross sections. Historically, DNA

and RNA detection have been carried out by functionalizing the SERS substrate with single-stranded oligonucleotides (i.e., capture strands), to which the target molecule (i.e., target strand) would hybridize. The hybridization would then be recognized because of changes in substrate charge [201] or because of the presence on the capture strand of a tail sequence of at least three to five bases that could then hybridize to a third fluorescently labeled oligonucleotide bound to a gold nanoparticle, also known as the A-B-C recognition scheme [202]. Starting from these early works, oligonucleotide detection has improved significantly, leading to sensing schemes for the multiplexed detection of oligonucleotides with LODs of 10 pM [203] or lower.

Currently, after the quantum mechanical understanding of the factors influencing the resonant Raman bands typical of individual nucleobases [204] and the first identification and assignment of these resonances in short microRNAs [205], several publications focusing on the direct SERS-based identification of unlabeled oligonucleotides have appeared [206, 207]. However, due to the complexity of the signals collected, the majority of them limit their investigation to the identification of the fingerprinting signatures of the various bases and cannot achieve direct detection of base sequence in long oligonucleotides via SERS. The goal of the next years will be to understand how this identification can be achieved.

4.9.5.2 Proteins

Proteins are ubiquitous molecules that are important for various activities of the organism, from immune response to DNA replication. They can be large (e.g., immunoglobulin) or small (e.g., thrombin), but they all have in common the fact that they can be recognized and captured by specific antibodies. Recently, it has been understood that proteins present unique, electrostatically charged pockets, called epitopes, which can bind special oligonucleotides, called aptamers, with high selectivity and specificity, and binding constants that surpass those of antibodies. Therefore, in SERS biosensing schemes for proteins, the use of antibodies and aptamers as recognition moieties has started to become evenly distributed, also spurred by the fact that aptamers are overall cheaper and more resistant to manipulation. Based on the concept of ELISA, several years ago, the first SERS-based ELISA immunosensor for thrombin was demonstrated, with LODs surpassing those of commercially available kits [208]. After that, several SERS sensing schemes have appeared, all having in common the sandwich construct and the use of SERS tags. Some of them were implemented to be used for lab-on-chip applications via 3D barcoding and attomolar LODs [209] or to be employed in microfluidic devices for the detection of the hepatitis B antigen [210]. These sensing platforms, especially when used in complex matrices, are plagued by opsonization, that is, the rapid and unavoidable formation of a nonspecifically bound layer of proteins on the substrate, leading to false-positive results. Recently, Yu and coworkers [211] have developed a stealth surface modification of SERS substrates to reduce the number of nonspecific binding events and increase the overall sensitivity and selectivity of the assay. To

further enhance the signal, Fan and coworkers have instead focused on increasing the number of *hot spots* on the substrate, by developing the nano-rolling-circle amplification strategy [212]. Owing to this approach, they were able to increase the LODs of their platform to reach the zeptomolar concentration level. In addition to the detection of whole proteins, substrates for the identification of their components, amino acids, and peptides have also been designed and implemented, but they are much less common [213–215].

4.9.5.3 Viruses and Bacteria

As a straightforward, albeit quite complex extension from what just described, substrates for the detection of viruses and bacteria, or, more precisely, for the identification of their distinctive genetic signatures or proteinaceous components, have appeared.

Viruses are characterized primarily by their genome, based on either DNA or RNA, and by a capsid, a proteic shell coded for by the virus, which is studded with specific proteins that have the role of specifically targeting their host cells. Some of the viruses are surrounded by a lipid bilayer called envelope that facilitates penetration via budding. Therefore, when aiming toward virus identification, one can focus on both oligonucleotides and proteins, often following sensing schemes that are quite similar to those seen in biosensors. In general, the majority of the approaches choose to identify the whole virus, thus employing aptamers or antibodies for capture or attempting to distinguish various viruses or strains by detecting variation in the peak pattern obtained via direct detection. For instance, Dluhy and coworkers were able to directly detect via SERS the binding of nucleoproteins for influenza and RSV to their specific aptamers bound to a gold nanorod-based substrate by identifying the novel spectral features arising after protein capture by the aptamer [216]. Ray and coworkers used instead a graphene oxide-based probe to detect HIV DNA at the femtomolar level without labeling [217]. Overall however, while these and other approaches have started to become effective in the identification of viruses [218, 219], this field is still far from becoming effectively applicable for prevention and diagnosis.

Similar to that of viruses, the detection of bacteria and other microorganisms is still at its infancy. In general, sensors for the detection of bacteria aim at identification in either blood or food. ELISA-analogue bioassays for the detection of *Streptococcus suis* II were developed by Luo and coworkers [220], who employed thorny gold nanoparticles in conjunction to a muramidase-released protein antibody and immuno-SERS tags to achieve detection limits of 0.1 pg mL^{-1}, which were validated in pig serum samples. Culture-free analysis of bacteria in human blood was instead achieved by Wang and coworkers [221], who designed a SERS substrate in which vancomycin (Van)-coated silver nanoparticle arrays were employed for both sample concentration and identification and enabled the discrimination between Van-susceptible and Van-resistant *Enterococcus*. The use of antibiotics to coat the SERS substrate was also exploited by Waluk and coworkers, who were

able to identify in blood a panel of bacteria by recognition of fingerprinting bands characterizing their structure [222]. As also stressed by the authors, and despite the progress in bacteria identification brought forward by the need of detecting food and water contamination [223–225], still significant work needs to be done in this context, especially to generate bacterial SERS databases to render these measurements more universally applicable.

4.9.6 Medical Applications

Perhaps the most difficult community for SERS to penetrate, yet the most promising for the impact that the technique could bring in the future, is medicine. The two main applications that, despite only at the proof-of-concept stage, have made the most progress are the detection of metabolites and biomarkers in blood or physiological solutions and the study of cell properties in diseases, primarily cancer. Substrates have been recently developed for the study of biomarkers in blood and other relevant solutions, also at low concentration [226, 227]. Among the biomarkers of interest, healthy, [228] drug-induced, [229, 230], and diseased markers have been targeted [231–233]. Despite conceptualized to identify different targets, all these sensing schemes have in common the understanding that they need to be simple to use, to clearly deconvolve the response of the target from the background signal of the matrix, to require minimal to no sample preparation, and to be usable in various physiological matrices such as blood, saliva, or urine.

One step forward from the detection of biomarkers is the study of cells. Although various approaches have been developed toward cell imaging in SERS [171], we will focus here only on the approaches in which *direct* study of cells and cell membranes has been enabled via cleverly designed substrates. For instance, Dante and coworkers developed a substrate based on thin nanoporous alumina for single-cell study [234], while Manikandan et al. employed gold nanohexagons to study cancer cells and cancer stem cells. While their assignment is quite tentative, due to the complexity of the SERS signals originating from whole cells, they were able to discriminate between breast normal cells, breast cancer cells, and breast cancer stem cells [235]. Improving upon these results, Sasso and coworkers were recently able to clearly assign bands from lipids and proteins in red blood cells, clearly distinguishing between peaks originating from the two membrane components [236]. Despite focusing on red blood cells, this work is clearly simplifying the efforts of those interested in the direct, label-free, SERS study of cells. Looking into current hot topics in cancer, we can clearly mark the effort toward understanding of circulating tumor cells (CTCs) [237]. CTCs are cells that have detached from their original tumor site, undergone epithelial-to-mesenchymal transition becoming highly mobile and aggressive, and entered the blood and lymphatic system to migrate to a new distant microenvironment. Once there, they will resettle causing metastasis. Because of their importance, several groups have been focusing on understanding their properties and dynamics, but these efforts have been severely impacted in their

outcomes by the limited numbers of CTCs available in blood. An alternative that has recently become important is the study of exosomes, vesicles that are excreted by the diseased cells and carry all their biomarkers. For instance, Wachsmann-Hogiu and coworkers have developed a 3D nanobowl SERS platform for the detection of exosomes from SKOV3 cell lines, and were able to monitor the composition and rupture of their membrane, and their content, over time [238]. The study of apoptotic cells using SERS has also been demonstrated [239]. Although less common and often challenging, the study of tissues via direct SERS methods is also possible [240]. In their 2014 work, Kajimura and coworkers were able to directly image the distinguishing features of brain ischemic cells employing gold nanoparticles grown on nanoarrays of transparent boehmite. By mapping the ischemic core and the contralateral control areas, they found that by following the adenine ring vibrations, the demarcation of ischemic tissues could be effectively achieved.

4.9.7 Therapeutic Drugs

For personalized therapeutic approaches in several diseases and for cancer treatment, ultrasensitive detection of drugs in low quantity is extremely important. Few studies reported on the SERS determination of widely used anticancer drugs, sunitinib, paclitaxel, and irinotecan [241–245], three commonly used antineoplastic drugs, and of SN-38 (the metabolite of irinotecan) [34, 246] with limits of detection of 20–70 ng. Yuen et al. reported the quantification of paclitaxel down to the 10^{-2} nM range using gold/polystyrene substrates and 785 nm laser excitation [242]. The quantification of doxorubicin and mitoxantrone, two bright Raman-active chemotherapy drugs, was also reported with excitation at 488 nm [241, 243] and 633 nm [244, 245], respectively. Also the detection and quantification of the acetylsalicylic acid in commercial tablets have been recently demonstrated by using filter paper coated with silver nanoparticles as a SERS substrate [247]. This method allowed to quantify the acetylsalicylic acid at low concentration levels (in the range 0.1–1 mM), a value comparable to the HPLC method.

4.9.8 Forensic Science and Illicit Drugs

The first nonacademic setting that has early on learned to appreciate the advantages of SERS is the forensics community. The detection of illicit drugs and the identification of fingerprints, with limited to no possibility of false positives, have emerged over a decade ago as an area of investigation in which SERS and SERS substrates could bring significant advantages.

One of the most traditional types of illicit drugs is opium. Opium is at the basis of the manufacture of some of the most common painkillers, such as morphine and codeine. However, opium addiction has plagued society early on, starting

during the Greek and Roman times and reaching its peak worldwide diffusion at the beginning of the twentieth century. As opium is often converted into heroin to facilitate smuggling, its trade is at the basis of concerning international narcotrafficking activities and the focus of constant monitoring by authorities. Therefore, the early identification of opium and opiate derivatives has been the goal of forensic identification for quite some time. Recently, Moskovits and coworkers have shown that SERS can be effectively used to identify papaverine, a fundamental component of the opium poppy that, while being negligible in the final product, if detected on a suspect, is a clear indication that the person has been handling poppy seeds [248]. Detection of heroin and cocaine at the ng scale has been instead demonstrated by White and Yu [249] who have developed a lateral-flow dipstick SERS substrate capable of easily collecting the analyte molecules over a large area and concentrating them in a precisely focused area for quantitative identification with high repeatability.

Implicit with the purpose of forensics is the fact that all the analyses need to be carried out simply and, in some instances, on-site, making it necessary to develop sensing approaches that are portable and rugged. Liu and coworkers have designed and developed a portable kit for the identification of drugs in human urine [250], based on substrates prepared via assembly of gold nanorod arrays. They detected several analytes at the ppm level despite the complex matrix. Cheng and coworkers, by assembling gold nanocubes on flexible substrates, identified benzocaine at the ppb level with excellent correlation between SERS peak intensity and concentration [251]. This concentration level is well below the concentration of benzocaine in the saliva of overdosed individuals. By stamping their nanocube array on a banknote, they were also able to detect the drug at a concentration of 1 $\mu g/cm^2$, which is of extreme relevance for positive identification of cash involved in the drug trade. The use of coins as actual substrates for the amplification of Raman signals has been cleverly exploited by Goodacre and coworkers [252], who were able to detect three drugs, namely, 4-methylmethcathinone, 5,6-methylenedioxy-2-aminoindane, and 3,4-methylenedioxy-N-methylamphetamine, which, despite being technically legal, can cause serious side effects if taken in wrong dosage and should therefore be closely monitored.

The detection of trace amounts of methamphetamine in drinking water has been recently tested using silver nanomushroom arrays and a handheld Raman spectrometer: with this system, a limit of detection of 0.5 mg/L has been obtained [253]. Different drug classes such as barbiturates, opiates, amphetamines, and benzodiazepines have also been identified by SERS, exploiting their affinity toward human serum albumin. Limits of detection were in the range of 90–400 ng/ml for all drugs.

SERS has also been tested to detect and identify artificial hair dyes in situ, using gold nanorods as plasmonic enhancers. The possibility of recognizing the hair dye (and its commercial brand) provides valuable information that can be exploited in forensic investigations [254].

Further studies are summarized in the reviews by Ryder et al. [255] and by Muehlethaler et al. [256]. The first one reports the detection of small molecules,

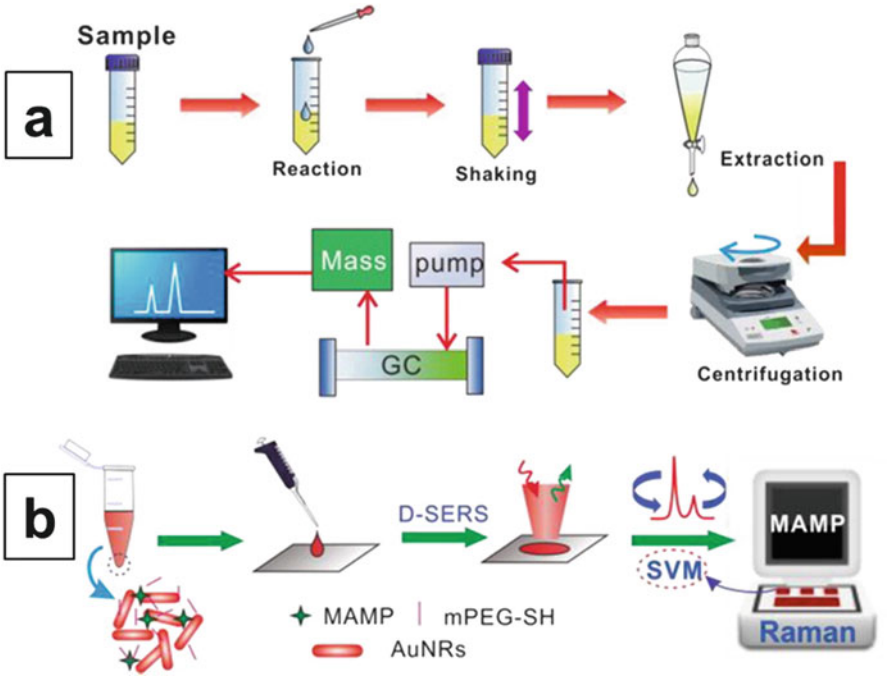

Fig. 4.26 Drug detection in urine. (**a**) Standard GC/MS procedure, based on the analyte extraction, and (**b**) SERS procedure. The Raman analyte is mixed with colloidal nanoparticles, and hot spots are generated through the addition of an external agent that induces particle aggregation prior to the SERS measurements; SVM is a support vector machine, used for accurate identification of drugs in human urine (Reproduced with permission from Ref. [257])

drugs, narcotics, and amino acids. The second, and more recent one, reports a wide range of applications to forensic science, concerning questioned document examination, fiber analysis, and detection of drugs, together with the investigation of biological materials, like blood or bodily fluids and DNA. The review also clearly illustrates how to perform the detection of extraneous molecules present in these complex matrixes and how to compare the traditional analytical methods (like gas chromatography/mass spectroscopy (GC-MS) detection) with SERS (Fig. 4.26) [257].

4.9.9 Novel Applications

Looking forward, some new and interesting avenues of research have started to become relevant. SERS substrates that can perform multiple functions or that can be employed to study subjects of historical provenance should be considered in order to facilitate the broad understanding of SERS and its relevance. For instance,

SERS substrates that nondestructively analyze artworks employing NIR excitation [258] or, similarly, substrates designed to study pH in the NIR [259] have appeared. While the first example is relevant for their role in the preservation of art heritage, both share the fact that can be employed in the NIR. The use of NIR radiation for excitation has been so far greatly underestimated due to technological difficulties in achieving performing detectors; however, slow but steady progress in this area warrants a more in-depth focus on these applications, which are advantageous compared to those employing higher-energy lasers as they do not lead to heat-induced sample damage [260]. Finally, and perhaps most interestingly, are those SERS substrates that can monitor catalytic intermediates and can thus facilitate our understanding of catalytic mechanisms. For instance, Yang and coworkers focused on the detection of water splitting reaction intermediates [261], while Bao et al. studied in situ the photocatalytic decomposition of organic pollutants in the environment [262]. Substrates that simultaneously enable catalysis and detection are also intriguing. Chen and coworkers reported, for example, on arrays of AgS_2 microrods that can act as substrates for photocatalytic degradation of organic dyes and SERS detection of the reaction intermediates [263], while Cao et al. achieved similar results functionalizing AgCl membranes with porous Au-Ag alloy particles [264]. To bring their substrate one step closer to real-life applications, Jiang and coworkers opted instead for Pt-coated ultrathin gold nanowire substrates that can be employed *in operando* for monitoring reactions such as *p*-nitrothiophenol reduction [265]. Overall, these approaches make a strong case for further studying and improving SERS platforms. Importantly, however, one should never exclusively focus on the application alone; the understanding of the fundamental rules applying to each individual scenario is also extremely important and sits at the basis of all the various applications we have described above.

4.10 Conclusions

The origin of surface-enhanced spectroscopies dates back to the early 1970s, when scientists observed an unusually strong Raman signal from pyridine molecules adsorbed on roughened silver electrodes. A few years later, two independent papers explained this observation on the basis of what are nowadays known as "electromagnetic enhancement" and "chemical enhancement". Since then, surface-enhanced Raman scattering has triggered lots of interest in the scientific community as witnessed by the remarkable increase in the percentage of publications dedicated to this topic, in particular from year 2000. Surface enhancement effects have been exploited also to improve the signal from other optical spectroscopies, in particular fluorescence and IR absorption, even though the lion's share is still up to SERS.

In the course of this chapter, we have focused on SERS, exploring in particular the following aspects:

- The physical origin of the electromagnetic and the chemical enhancements, the derivation of the widely employed $|E|^4$ approximation, and the concept of hot spots and its role in SERS.
- The materials and the strategies adopted to fabricate solid substrates, sorting them out in three principal categories: bottom-up, top-down, and template methods.
- The sensoristic applications of SERS, in particular those that exploit a direct detection protocol, in which analytes are directly recognized from the fingerprinting modes of their spectra, rather than from the band of a Raman reporter molecule: examples have been reported for chemical warfare agents, environmental pollutants, food contaminants, biomolecules, etc.

Overall, over the years, SERS has evolved to become a technique with great potential of further development. In particular, currently most of the publications are devoted to the fabrication of cost-effective substrates with optimized performances and to the implementation of the technique in a very wide range of analytical or sensoristic applications. Notably, the development of SERS has been profiting from recent technical advances in the instrumentation (that has led to the commercialization of portable Raman spectrometers) and from the fabrication of good-quality SERS substrates (commercialized by some companies or university spin-offs). Owing to these aspects, SERS has started transitioning from the academic laboratories to the real-life world, where it now needs to find its niche of application among the analytical methods that are currently routinely used.

Acknowledgments We gratefully thank the Italian Ministero dell'Università e della Ricerca (MIUR) for financial support through the PRIN project "New aspects of resonance energy transfer in organized media: dynamical effects and optical control" (Prot. 2012T9XHH7).

References

1. C.L. Haynes, C.R. Yonzon, X. Zhang, R.P. Van Duyne, Surface-enhanced Raman sensors: Early history and the development of sensors for quantitative biowarfare agent and glucose detection. J. Raman Spectrosc. **36**, 471–484 (2005). https://doi.org/10.1002/jrs.1376
2. M. Fleischmann, P.J. Hendra, A.J. McQuillan, Raman spectra of pyridine adsorbed at a silver electrode. Chem. Phys. Lett. **26**, 163–166 (1974). https://doi.org/10.1016/0009-2614(74)85388-1
3. D.L. Jeanmaire, R.P. Van Duyne, Surface Raman spectroelectrochemistry. J. Electroanal. Chem. Interfacial Electrochem. **84**, 1–20 (1977). https://doi.org/10.1016/S0022-0728(77)80224-6
4. Albrecht et al., Anomalously intense Raman spectra of pyridine at a silver electrode. JACS **99**, 5215–5217 (1977). https://doi.org/10.1021/ja00457a071
5. P. Hendra, M. Fleischmann, P. Hendra, J. McQuillan, A.J. Mcquillan, THE DISCOVERY OF SERS: An idiosyncratic account from a vibrational spectroscopist. Analyst **141**, 4996–4999 (2016). https://doi.org/10.1039/C6AN90055K
6. J.R. Lakowicz, Radiative decay engineering: Biophysical and biomedical applications. Anal. Biochem. **298**, 1–24 (2001). https://doi.org/10.1006/abio.2001.5377
7. F. Neubrech, C. Huck, et al. Surface-enhanced infrared spectroscopy using resonant nanoantennas. Chem. Rev. **117**(7), 5110–5145 (2017)

8. M. Gühlke, Z. Heiner, J. Kneipp, Surface-enhanced Raman and surface-enhanced hyper-Raman scattering of thiol-functionalized carotene. J. Phys. Chem. C (2016). https://doi.org/10.1021/acs.jpcc.6b01895
9. C. Steuwe, C.F. Kaminski, J.J. Baumberg, S. Mahajan, Surface enhanced coherent anti-Stokes Raman scattering on nanostructured gold surfaces. Nano Lett. **11**, 5339–5343 (2011). https://doi.org/10.1021/nl202875w
10. T. Ichimura, N. Hayazawa, M. Hashimoto, Y. Inouye, S. Kawata, Local enhancement of coherent anti-Stokes Raman scattering by isolated gold nanoparticles. J. Raman Spectrosc. **34**, 651–654 (2003). https://doi.org/10.1002/jrs.1047
11. G.F. Walsh, L. Dal Negro, Enhanced second harmonic generation by photonic-plasmonic Fano-type coupling in nanoplasmonic arrays. Nano Lett. **13**, 3111–3117 (2013). https://doi.org/10.1021/nl401037n
12. E.C. Le Ru, P.G. Etchegoin, *Principles of Surface Enhanced Raman Spectroscopy* (Elsevier, Amsterdam, 2009)
13. J.R. Lombardi, R.L. Birke, A unified view of surface-enhanced Raman scattering. Acc. Chem. Res. **42**, 734–742 (2009). https://doi.org/10.1021/ar800249y
14. M. Moskovits, Persistent misconceptions regarding SERS. Phys. Chem. Chem. Phys. **15**, 5301 (2013). https://doi.org/10.1039/c2cp44030j
15. A. Otto, The "chemical" (electronic) contribution to surface-enhanced Raman scattering. J. Raman Spectrosc. **36**, 497–509 (2005). https://doi.org/10.1002/jrs.1355
16. M. Moskovits, Surface-enhanced Raman spectroscopy: A brief retrospective. J. Raman Spectrosc. **36**, 485–496 (2005). https://doi.org/10.1002/jrs.1362
17. S.L. Kleinman, B. Sharma, M.G. Blaber, A.I. Henry, N. Valley, R.G. Freeman, M.J. Natan, G.C. Schatz, R.P. Van Duyne, Structure enhancement factor relationships in single gold nanoantennas by surface-enhanced Raman excitation spectroscopy. J. Am. Chem. Soc. **135**, 301–308 (2013). https://doi.org/10.1021/ja309300d
18. E.C. Le Ru, M. Meyer, E. Blackie, P.G. Etchegoin, Advanced aspects of electromagnetic SERS enhancement factors at a hot spot. J. Raman Spectrosc. **39**, 1127–1134 (2008). https://doi.org/10.1002/jrs
19. S. Nie, S.R. Emory, Probing single molecules and single nanoparticles by surface-enhanced Raman scattering. Science **275**, 1102–1106 (1997). https://doi.org/10.1126/science.275.5303.1102
20. P.G. Etchegoin, E.C. Le Ru, A perspective on single molecule SERS: Current status and future challenges. Phys. Chem. Chem. Phys. **10**, 6079 (2008). https://doi.org/10.1039/b809196j
21. M. Fan, G.F.S. Andrade, A.G. Brolo, A review on the fabrication of substrates for surface enhanced Raman spectroscopy and their applications in analytical chemistry. Anal. Chim. Acta **693**, 7–25 (2011). https://doi.org/10.1016/j.aca.2011.03.002
22. M. Stewart, C.R. Anderton, L.B. Thompson, J. Maria, S.K. Gray, J.A. Rogers, R.G. Nuzzo, Nanostructured plasmonic sensors. Chem. Rev. **108**, 494–521 (2008). https://doi.org/10.1021/cr068126n
23. L. Polavarapu, L.M. Liz-Marzán, Towards low-cost flexible substrates for nanoplasmonic sensing. Phys. Chem. Chem. Phys. **15**, 5288 (2013). https://doi.org/10.1039/c2cp43642f
24. B. Sharma, R.R. Frontiera, A.-I. Henry, E. Ringe, R.P. Van Duyne, SERS: Materials, applications, and the future. Mater. Today **15**, 16–25 (2012). https://doi.org/10.1016/S1369-7021(12)70017-2
25. K.C. Bantz, A.F. Meyer, N.J. Wittenberg, H. Im, O. Kurtuluş, S.H. Lee, N.C. Lindquist, O. S-H, C.L. Haynes, Recent progress in SERS biosensing. Phys. Chem. Chem. Phys. **13**, 11551 (2011). https://doi.org/10.1039/c0cp01841d
26. R. Petry, M. Schmitt, J. Popp, Raman spectroscopy-a prospective tool in the life sciences. Chem. Phys. Chem. **4**, 14–30 (2003). https://doi.org/10.1002/cphc.200390004
27. X.-M. Qian, S.M. Nie, Single-molecule and single-nanoparticle SERS: From fundamental mechanisms to biomedical applications. Chem. Soc. Rev. **37**, 912 (2008). https://doi.org/10.1039/b708839f

28. X. Qian, X.-H. Peng, D.O. Ansari, Q. Yin-Goen, G.Z. Chen, D.M. Shin, L. Yang, A.N. Young, M.D. Wang, S. Nie, In vivo tumor targeting and spectroscopic detection with surface-enhanced Raman nanoparticle tags. Nat. Biotechnol. **26**, 83–90 (2008). https://doi.org/10.1038/nbt1377
29. S. Schlücker, Surface-enhanced Raman spectroscopy: Concepts and chemical applications. Angew. Chem. Int. Ed. **53**, 4756–4795 (2014). https://doi.org/10.1002/anie.201205748
30. F. Romanato, R. Pilot, M. Massari, T. Ongarello, G. Pirruccio, P. Zilio, G. Ruffato, M. Carli, D. Sammito, V. Giorgis, D. Garoli, R. Signorini, P. Schiavuta, R. Bozio, Design, fabrication and characterization of plasmonic gratings for SERS. Microelectron. Eng. **88**, 2717–2720 (2011). https://doi.org/10.1016/j.mee.2011.02.052
31. I. Ros, T. Placido, V. Amendola, C. Marinzi, N. Manfredi, R. Comparelli, M. Striccoli, A. Agostiano, A. Abbotto, D. Pedron, R. Pilot, R. Bozio, SERS properties of gold Nanorods at resonance with molecular, transverse, and longitudinal plasmon excitations. Plasmonics, 1–13 (2014). https://doi.org/10.1007/s11468-014-9669-4
32. R.A. Tripp, R.A. Dluhy, Y. Zhao, Novel nanostructures for SERS biosensing. Nano Today **3**, 31–37 (2008). https://doi.org/10.1016/S1748-0132(08)70042-2
33. S.D. Hudson, G. Chumanov, Bioanalytical applications of SERS (surface-enhanced Raman spectroscopy). Anal. Bioanal. Chem. **394**, 679–686 (2009). https://doi.org/10.1007/s00216-009-2756-2
34. L. Litti, V. Amendola, G. Toffoli, M. Meneghetti, Detection of low-quantity anticancer drugs by surface-enhanced Raman scattering. Anal. Bioanal. Chem. **408**, 1–9 (2016). https://doi.org/10.1007/s00216-016-9315-4
35. D.A. Stuart, K.B. Biggs, R.P. Van Duyne, Surface-enhanced Raman spectroscopy of half-mustard agent. Analyst **131**, 568 (2006). https://doi.org/10.1039/b513326b
36. J.M. Sylvia, J.A. Janni, J.D. Klein, K.M. Spencer, Surface-enhanced Raman detection of 2,4-dinitrotoluene impurity vapor as a marker to locate landmines. Anal. Chem. **72**, 5834–5840 (2000). https://doi.org/10.1021/ac0006573
37. R.S. Golightly, W.E. Doering, M.J. Natan, Surface-enhanced Raman spectroscopy and homeland security: A perfect match? ACS Nano **3**, 2859–2869 (2009). https://doi.org/10.1021/nn9013593
38. J. Kubackova, G. Fabriciova, P. Miskovsky, D. Jancura, S. Sanchez-Cortes, Sensitive surface-enhanced Raman spectroscopy (SERS) detection of organochlorine pesticides by alkyl dithiol-functionalized metal nanoparticles-induced plasmonic hot spots. Anal. Chem. **87**, 663–669 (2015). https://doi.org/10.1021/ac503672f
39. S. Sánchez-Cortés, C. Domingo, J.V. García-Ramos, J.A. Aznárez, Surface-enhanced vibrational study (SEIR and SERS) of Dithiocarbamate pesticides on gold films. Langmuir **17**, 1157–1162 (2001). https://doi.org/10.1021/la001269z
40. D. Lee, S. Lee, G.H. Seong, J. Choo, E.K. Lee, D.-G. Gweon, S. Lee, Quantitative analysis of methyl parathion pesticides in a polydimethylsiloxane microfluidic channel using confocal surface-enhanced Raman spectroscopy. Appl. Spectrosc. **60**, 373–377 (2006). https://doi.org/10.1366/000370206776593762
41. X. Li, G. Chen, L. Yang, Z. Jin, J. Liu, Multifunctional Au-coated TiO_2 nanotube arrays as recyclable SERS substrates for multifold organic pollutants detection. Adv. Funct. Mater. **20**, 2815–2824 (2010). https://doi.org/10.1002/adfm.201000792
42. J. Zheng, L. He, Surface-enhanced Raman spectroscopy for the chemical analysis of food. Compr. Rev. Food Sci. Food Saf. **13**, 317–328 (2014). https://doi.org/10.1111/1541-4337.12062
43. K. Chen, M. Leona, T. Vo-Dinh, Surface-enhanced Raman scattering for identification of organic pigments and dyes in works of art and cultural heritage material. Sens. Rev. **27**, 109–120 (2007). https://doi.org/10.1108/02602280710731678
44. F. Casadio, M. Leona, J.R. Lombardi, R.P. Van Duyne, Identification of organic colorants in fibers, paints, and glazes by surface enhanced Raman spectroscopy. Acc. Chem. Res. **43**, 782–791 (2010). https://doi.org/10.1021/ar100019q

45. Y. Yang, Z.-Y. Li, K. Yamaguchi, M. Tanemura, Z. Huang, D. Jiang, Y. Chen, F. Zhou, M. Nogami, Controlled fabrication of silver nanoneedles array for SERS and their application in rapid detection of narcotics. Nanoscale **4**, 2663–2669 (2012). https://doi.org/10.1039/c2nr12110g
46. B. Sägmüller, B. Schwarze, G. Brehm, S. Schneider, Application of SERS spectroscopy to the identification of (3,4-methylenedioxy) amphetamine in forensic samples utilizing matrix stabilized silver halides. Analyst **126**, 2066–2071 (2001). https://doi.org/10.1039/b105321n
47. V. Perazzolo, C. Durante, R. Pilot, A. Paduano, J. Zheng, G.A. Rizzi, A. Martucci, G. Granozzi, A. Gennaro, Nitrogen and sulfur doped mesoporous carbon as metal-free electrocatalysts for the in situ production of hydrogen peroxide. Carbon **95**, 949–963 (2015). https://doi.org/10.1016/j.carbon.2015.09.002
48. V. Perazzolo, E. Gradzka, C. Durante, R. Pilot, N. Vicentini, G.A. Rizzi, G. Granozzi, A. Gennaro, Chemical and electrochemical stability of nitrogen and sulphur doped mesoporous carbons. Electrochim. Acta **197**, 251–262 (2016). https://doi.org/10.1016/j.electacta.2016.02.025
49. Y.F. Huang, D.Y. Wu, A. Wang, B. Ren, S. Rondinini, Z.Q. Tian, C. Amatore, Bridging the gap between electrochemical and organometallic activation: Benzyl chloride reduction at silver cathodes. J. Am. Chem. Soc. **132**, 17199–17210 (2010). https://doi.org/10.1021/ja106049c
50. N.L. Gruenke, M.F. Cardinal, M.O. McAnally, R.R. Frontiera, G.C. Schatz, R.P. Van Duyne, Ultrafast and nonlinear surface-enhanced Raman spectroscopy. Chem. Soc. Rev. **45**, 2263 (2016). https://doi.org/10.1039/c5cs00763a
51. L. Orian, R. Pilot, R. Bozio, In silico stark effect: Determination of excited state polarizabilities of squaraine dyes. J. Phys. Chem. A **121**, 1587–1596 (2017). https://doi.org/10.1021/acs.jpca.6b12090
52. D.A. Long, *The Raman Effect a Unified Treatment of the Theory of Raman Scattering by Molecules* (Wiley, Chichester, 2002)
53. R. Aroca, *Surface-Enhanced Vibrational Spectroscopy* (Wiley, Hoboken, 2006)
54. R.L. McCreery, *Raman Spectroscopy for Chemical Analysis* (Wiley, New York, 2000)
55. S.A. Maier, *Plasmonics: Fundamentals and Applications* (Springer, New York, 2007)
56. V. Amendola, R. Pilot, M. Frasconi, O.M. Maragò, A.M. Iatì, Surface plasmon resonance in gold nanoparticles: A review. J. Phys. Condens. Matter (2017). https://doi.org/10.1088/1361-648X/aa60f3
57. C. Burda, X. Chen, R. Narayanan, M.A. El-Sayed, Chemistry and properties of nanocrystals of different shapes. Chem. Rev. (2005). https://doi.org/10.1021/cr030063a
58. S. Eustis, M.A. El-Sayed, Why gold nanoparticles are more precious than pretty gold: Noble metal surface plasmon resonance and its enhancement of the radiative and nonradiative properties of nanocrystals of different shapes. Chem. Soc. Rev. **35**, 209–217 (2006). https://doi.org/10.1039/b514191e
59. A. Poletti, G. Fracasso, G. Conti, R. Pilot, V. Amendola, Laser generated gold nanocorals with broadband plasmon absorption for photothermal applications. Nanoscale **7**, 13702–13714 (2015). https://doi.org/10.1039/c5nr03442f
60. L. Novotny, B. Hecht, *Principles of Nano-Optics* (Cambridge University Press, Cambridge, 2007)
61. M. Pelton, Modified spontaneous emission in nanophotonic structures. Nat. Photonics **9**, 427–435 (2015). https://doi.org/10.1038/nphoton.2015.103
62. E.M. Purcell, Spontaneous emission probabilities at radio frequencies. Phys. Rev. **69**, 681
63. K.H. Drexhage, H. Kuhn, F.P. Schafer, W. Sperling, Variation of the fluorescence decay time of a molecule in front of a mirror. Ber. Bunsenges. Phys. Chem. **20**, 1179 (1966)
64. K.H. Drexhage, *Progress in Optics XII, Edited* (North-Holland, Amsterdam, 1974)
65. K.H. Drexhage, Influence of a dielectric interface on fluorescence decay time. J. Lumin. **1**(2), 693–701 (1970)
66. P. Goy, J.M. Raimond, M. Gross, S. Haroche, Observation of cavity-enhanced single-atom spontaneous emission. Phys. Rev. Lett. **50**, 1903–1906 (1983). https://doi.org/10.1103/PhysRevLett.50.1903

67. P. Andrew, W.L. Barnes, Förster energy transfer in an optical microcavity. Science **290**, 785–788 (2000). https://doi.org/10.1126/science.290.5492.785
68. J.D. Jackson, *Classical Electrodynamics* (Wiley, Estados Unidos, 1998)
69. E.C. Le Ru, J. Grand, N. Félidj, J. Aubard, G. Lévi, A. Hohenau, J.R. Krenn, E. Blackie, P.G. Etchegoin, Experimental verification of the SERS electromagnetic model beyond the $|E|^4$ approximation: Polarization effects. J. Phys. Chem. C. Lett. **112**, 8117–8121 (2008). https://doi.org/10.1021/jp802219c
70. B. Fazio, C. D'Andrea, F. Bonaccorso, A. Irrera, G. Calogero, C. Vasi, P.G. Gucciardi, M. Allegrini, A. Toma, D. Chiappe, C. Martella, F. Buatier De Mongeot, Re-radiation enhancement in polarized surface-enhanced resonant raman scattering of randomly oriented molecules on self-organized gold nanowires. ACS Nano **5**, 5945–5956 (2011). https://doi.org/10.1021/nn201730k
71. M. Moskovits, Surface-enhanced spectroscopy. Rev. Mod. Phys. **57**, 783 (1985). https://doi.org/10.1103/RevModPhys.57.783
72. P.W. Atkins, *Physical Chemistry* (Oxford Univeristy Press, Oxford, 1994)
73. A.D. McFarland, M.A. Young, J.A. Dieringer, R.P. Van Duyne, Wavelength-scanned surface-enhanced Raman excitation spectroscopy. J. Phys. Chem. B **109**, 11279–11285 (2005). https://doi.org/10.1021/jp050508u
74. N. Michieli, R. Pilot, V. Russo, C. Scian, F. Todescato, R. Signorini, S. Agnoli, T. Cesca, R. Bozio, G. Mattei, Oxidation effects on the SERS response of silver nanoprism arrays. RSC Adv. **7**, 369–378 (2017). https://doi.org/10.1039/C6RA26307K
75. R. Pilot, A. Zoppi, S. Trigari, F.L. Deepak, E. Giorgetti, R. Bozio, Wavelength dispersion of the local field intensity in silver-gold nanocages. Phys. Chem. Chem. Phys. **17**, 7355–7365 (2015). https://doi.org/10.1039/C4CP04453C
76. M.V. Cañamares, C. Chenal, R.L. Birke, J.R. Lombardi, DFT, SERS, and single-molecule SERS of crystal violet. J. Phys. Chem. C **112**, 20295–20300 (2008). https://doi.org/10.1021/jp807807j
77. J.D. Jiang, E. Burstein, H. Kobayashi, Resonant Raman scattering by crystal-violet molecules adsorbed on a smooth gold surface: Evidence for a charge transfer excitation. Phys. Rev. Lett. **57**, 1793–1796 (1986)
78. J.R. Lombardi, R.L. Birke, A unified approach to surface-enhanced Raman spectroscopy. J. Phys. Chem. C **112**, 5605–5617 (2008)
79. J.R. Lombardi, R.L. Birke, Theory of surface-enhanced Raman scattering in semiconductors. J. Phys. Chem. C **118**, 11120–11130 (2014). https://doi.org/10.1063/1.3698292
80. L.A. Dick, A.D. McFarland, C.L. Haynes, R.P. Van Duyne, Metal film over nanosphere (MFON) electrodes for surface-enhanced Raman spectroscopy (SERS): Improvements in surface nanostructure stability and suppression of irreversible loss. J. Phys. Chem. B **106**, 853–860 (2002). https://doi.org/10.1021/jp013638l
81. E.C. Le Ru, C. Galloway, P.G. Etchegoin, On the connection between optical absorption/extinction and SERS enhancements. Phys. Chem. Chem. Phys. **8**, 3083–3087 (2006). https://doi.org/10.1039/b605292d
82. P.L. Stiles, J.A. Dieringer, N.C. Shah, R.P. Van Duyne, Surface-enhanced Raman spectroscopy. Annu. Rev. Anal. Chem. **1**, 601–626 (2008). https://doi.org/10.1146/annurev.anchem.1.031207.112814
83. G. Compagnini, C. Galati, S. Pignataro, Distance dependence of surface enhanced Raman scattering probed by alkanethiol self-assembled monolayers. Phys. Chem. Chem. Phys. **1**, 2351–2353 (1999). https://doi.org/10.1039/a901034c
84. B.J. Kennedy, S. Spaeth, M. Dickey, K.T. Carron, Determination of the distance dependence and experimental effects for modified SERS substrates based on self-assembled monolayers formed using Alkanethiols. J. Phys. Chem. B **103**, 3640–3646 (1999). https://doi.org/10.1021/jp984454i
85. G.J. Kovacs, R.O. Loutfy, P.S. Vincett, C. Jennings, R. Aroca, Distance dependence of SERS enhancement factor from Langmuir-Blodgett monolayers on metal island films: Evidence for the electromagnetic mechanism. Langmuir **2**, 689–694 (1986). https://doi.org/10.1021/la00072a001

86. S.S. Masango, R.A. Hackler, N. Large, A.I. Henry, M.O. McAnally, G.C. Schatz, P.C. Stair, R.P. Van Duyne, High-resolution distance dependence study of surface-enhanced Raman scattering enabled by atomic layer deposition. Nano Lett. **16**, 4251–4259 (2016). https://doi.org/10.1021/acs.nanolett.6b01276
87. N.E. Marotta, K.R. Beavers, L.A. Bottomley, Limitations of surface enhanced Raman scattering in sensing DNA hybridization demonstrated by label-free DNA oligos as molecular rulers of distance-dependent enhancement. Anal. Chem. **85**, 1440–1446 (2013). https://doi.org/10.1021/ac302454j
88. C.A. Murray, D.L. Allara, Measurement of the molecule–silver separation dependence of surface enhanced Raman scattering in multilayered structures. J. Chem. Phys. **76**, 1290 (1982). https://doi.org/10.1063/1.443101
89. S.L. Kleinman, R.R. Frontiera, A.-I. Henry, J.A. Dieringer, R.P. Van Duyne, Creating, characterizing, and controlling chemistry with SERS hot spots. Phys. Chem. Chem. Phys. **15**, 21–36 (2013). https://doi.org/10.1039/c2cp42598j
90. E.C. Le Ru, J. Grand, I. Sow, W.R.C. Somerville, P.G. Etchegoin, M. Treguer-Delapierre, G. Charron, N. Félidj, G. Lévi, J. Aubard, A scheme for detecting every single target molecule with surface-enhanced raman spectroscopy. Nano Lett. **11**, 5013–5019 (2011). https://doi.org/10.1021/nl2030344
91. M.A. Mahmoud, M.A. El-Sayed, Aggregation of gold nanoframes reduces, rather than enhances, SERS efficiency due to the trade-off of the inter- and intraparticle plasmonic fields. Nano Lett. **9**, 3025–3031 (2009). https://doi.org/10.1021/nl901501x
92. W. Zhu, K.B. Crozier, Quantum mechanical limit to plasmonic enhancement as observed by surface-enhanced Raman scattering. Nat. Commun. **5**, 5228 (2014). https://doi.org/10.1038/ncomms6228
93. Y. Fang, N.-H. Seong, D.D. Dlott, Measurement of the distribution of site enhancements in surface-enhanced Raman scattering. Science **321**, 388–392 (2008). https://doi.org/10.1126/science.1159499
94. B.J. Messinger, K.U. Von Raben, R.K. Chang, P.W. Barber, Local fields at the surface of noble-metal microspheres. Phys. Rev. B **24**, 649–657 (1981). https://doi.org/10.1103/PhysRevB.24.649
95. N. Félidj, J. Aubard, G. Levi, J.R. Krenn, A. Hohenau, G. Schider, A. Leitner, F.R. Aussenegg, Optimized surface-enhanced Raman scattering on gold nanoparticle arrays. Appl. Phys. Lett. **82**, 3095–3097 (2003). https://doi.org/10.1063/1.1571979
96. N. Guillot, H. Shen, B. Frémaux, O. Péron, E. Rinnert, T. Toury, M.L. de la Chapelle, Surface enhanced Raman scattering optimization of gold nanocylinder arrays: Influence of the localized surface plasmon resonance and excitation wavelength. Appl. Phys. Lett. **97**, 23113 (2010). https://doi.org/10.1063/1.3462068
97. C. D'Andrea, A. Irrera, B. Fazio, A. Foti, E. Messina, O.M. Maragò, S. Kessentini, P. Artoni, C. David, P.G. Gucciardi, Red shifted spectral dependence of the SERS enhancement in a random array of gold nanoparticles covered with a silica shell: Extinction versus scattering. J. Opt. **17**, 114016 (2015). https://doi.org/10.1088/2040-8978/17/11/114016
98. K.U. Von Raben, R.K. Chang, B.L. Laube, P.W. Barber, Wavelength dependence of surface-enhanced Raman scattering from Ag colloids with adsorbed CN- complexes, SO3, and pyridine. J. Phys. Chem. **88**, 5290–5296 (1984)
99. D. Fornasiero, F. Grieser, Analysis of the visible absorption and SERS excitation spectra of silver sols. J. Chem. Phys. **87**, 3213 (1987). https://doi.org/10.1063/1.453009
100. H. Feilchenfeld, O. Siiman, Surface Raman excitation and enhancement profiles for chromate, molybdate, and tungstate on colloidal silver. J. Phys. Chem. **90**, 2163–2168 (1986)
101. M. Kerker, O. Siiman, O.S. Wang, Effect of aggregates on extinction and surface-enhanced Raman scattering spectra of colloidal silver. J. Phys. Chem. **88**, 3168–3170 (1984). https://doi.org/10.1021/j150659a003
102. E.C. Le Ru, M. Dalley, P.G. Etchegoin, Plasmon resonances of silver colloids studied by surface enhanced Raman spectroscopy. Curr. Appl. Phys. **6**, 411–414 (2006). https://doi.org/10.1016/j.cap.2005.11.030

103. V. Weber, A. Feis, C. Gellini, R. Pilot, P.R. Salvi, R. Signorini, Far- and nearfield properties of gold nanoshells studied by photoacoustic and surface-enhanced Raman spectroscopies. Phys. Chem. Chem. Phys. **17**, 21190–21197 (2015). https://doi.org/10.1039/C4CP05054A
104. F. Colas, M. Cottat, R. Gillibert, N. Guillot, N. Djaker, N. Lidgi-Guigui, T. Toury, D. Barchiesi, A. Toma, E. Di Fabrizio, P.G. Gucciardi, M.L. de la Chapelle, Red-shift effects in surface enhanced Raman spectroscopy: Spectral or intensity dependence of the near-field? J. Phys. Chem. C (2016). https://doi.org/10.1021/acs.jpcc.6b01492
105. J. Zuloaga, P. Nordlander, On the energy shift between near-field and far-field peak intensities in localized plasmon systems. Nano Lett. **11**, 1280–1283 (2011). https://doi.org/10.1021/nl1043242
106. P.R. West, S. Ishii, G.V. Naik, N.K. Emani, V.M. Shalaev, A. Boltasseva, Searching for better plasmonic materials. Laser Photonics Rev. **4**, 795–808 (2010). https://doi.org/10.1002/lpor.200900055
107. N.W. Ashcroft, N.D. Mermin, *Solid State Physics* (Saunders College Publishing, Orlando, 1976)
108. E. Cottancin, G. Celep, J. Lermé, M. Pellarin, J.R. Huntzinger, J.L. Vialle, M. Broyer, Optical properties of noble metal clusters as a function of the size: Comparison between experiments and a semi-quantal theory. Theor. Chem. Accounts **116**, 514–523 (2006). https://doi.org/10.1007/s00214-006-0089-1
109. P.B. Johnson, R.W. Christy, Optical constants of the noble metals. Phys. Rev. B **6**, 4370–4379 (1972). https://doi.org/10.1103/PhysRevB.6.4370
110. E.D. Palik, *Handbook of Optical Constants of Solids* (Academic, 1985)
111. G.H. Chan, J. Zhao, E.M. Hicks, G.C. Schatz, R.P. Van Duyne, Plasmonic properties of copper nanoparticles fabricated by nanosphere lithography. Nano Lett. **7**, 1947–1952 (2007). https://doi.org/10.1021/nl070648a
112. M. Muniz-Miranda, C. Gellini, E. Giorgetti, Surface-enhanced Raman scattering from copper nanoparticles obtained by laser ablation. J. Phys. Chem. C **115**, 5021–5027 (2011). https://doi.org/10.1021/jp1086027
113. T. Dörfer, M. Schmitt, J. Popp, Deep-UV surface-enhanced Raman scattering. J. Raman Spectrosc. **38**, 1379–1382 (2007). https://doi.org/10.1002/jrs
114. A. Taguchi, N. Hayazawa, K. Furusawa, H. Ishitobi, S. Kawata, Deep-UV tip-enhanced Raman scattering. J. Raman Spectrosc. **40**, 1324–1330 (2009). https://doi.org/10.1002/jrs.2287
115. Z.-L. Yang, Q.-H. Li, B. Ren, Z.-Q. Tian, M. Fleischmann, Tunable SERS from aluminium nanohole arrays in the ultraviolet region. Chem. Commun. **47**, 3909–3911 (2011). https://doi.org/10.1039/c0cc05311b
116. G.V. Naik, V.M. Shalaev, A. Boltasseva, Alternative plasmonic materials: Beyond gold and silver. Adv. Mater. **25**, 3264–3294 (2013). https://doi.org/10.1002/adma.201205076
117. I. Alessandri, J.R. Lombardi, Enhanced Raman scattering with dielectrics. Chem. Rev. (2016). https://doi.org/10.1021/acs.chemrev.6b00365
118. M.J. Natan, Concluding Remarks: Surface enhanced Raman scattering. Faraday Discuss. **132**, 321 (2006). https://doi.org/10.1039/b601494c
119. E.C. Le Ru, E.J. Blackie, M. Meyer, P.G. Etchegoin, Surface enhanced Raman scattering enhancement factors: A comprehensive study. J. Phys. Chem. C **111**, 13794–13803 (2007). https://doi.org/10.1021/jp0687908
120. R.J.C. Brown, M.J.T. Milton, Nanostructures and nanostructured substrates for surface-enhanced Raman scattering (SERS). J. Raman Spectrosc. **39**, 1313–1326 (2008). https://doi.org/10.1002/jrs.2030
121. H. Ko, S. Singamaneni, V.V. Tsukruk, Nanostructured surfaces and assemblies as SERS media. Small **4**, 1576–1599 (2008). https://doi.org/10.1002/smll.200800337
122. S. Fateixa, H.I.S. Nogueira, T. Trindade, Hybrid nanostructures for SERS: Materials development and chemical detection. Phys. Chem. Chem. Phys. **17**, 21046–21071 (2015). https://doi.org/10.1039/C5CP01032B

123. J.F. Betz, Y. WW, Y. Cheng, I.M. White, G.W. Rubloff, Simple SERS substrates: Powerful, portable, and full of potential. Phys. Chem. Chem. Phys. **16**, 2224–2239 (2014). https://doi.org/10.1039/C3CP53560F
124. H. Liu, L. Yang, J. Liu, Three-dimensional SERS hot spots for chemical sensing: Towards developing a practical analyzer. Trends Anal. Chem. **80**, 364–372 (2016). https://doi.org/10.1016/j.trac.2015.08.012
125. X. Sun, H. Li, A review: Nanofabrication of surface-enhanced raman spectroscopy (SERS) substrates. Curr. Nanosci. **12**, 175–183 (2016). https://doi.org/10.2174/1573413711666150523001519
126. L. Guerrini, D. Graham, Molecularly-mediated assemblies of plasmonic nanoparticles for surface-enhanced Raman spectroscopy applications. Chem. Soc. Rev. **41**, 7085–7107 (2012). https://doi.org/10.1039/c2cs35118h
127. D. Graham, The next generation of advanced spectroscopy: Surface enhanced Raman scattering from metal nanoparticles. Angew. Chem. Int. Ed. **49**, 9325–9327 (2010). https://doi.org/10.1002/anie.201002838
128. D. Cialla, A. März, R. Böhme, F. Theil, K. Weber, M. Schmitt, J. Popp, Surface-enhanced Raman spectroscopy (SERS): Progress and trends. Anal. Bioanal. Chem. **403**, 27–54 (2012). https://doi.org/10.1007/s00216-011-5631-x
129. Y. Cao, D. Li, F. Jiang, Y. Yang, Z. Huang, Engineering metal nanostructure for SERS application. J. Nanomater. (2013). https://doi.org/10.1155/2013/123812
130. M. Jahn, S. Patze, I.J. Hidi, R. Knipper, A.I. Radu, A. Mühlig, S. Yüksel, V. Peksa, K. Weber, T. Mayerhöfer, D. Cialla-May, J. Popp, Plasmonic nanostructures for surface enhanced spectroscopic methods. Analyst **141**, 756–793 (2015). https://doi.org/10.1039/C5AN02057C
131. P. Gao, D. Gosztola, L.W.H. Leung, M.J. Weaver, Surface-enhanced Raman scattering at gold electrodes: Dependence on electrochemical pretreatment conditions and comparisons with silver. J. Electroanal. Chem. **233**, 211–222 (1987). https://doi.org/10.1016/0022-0728(87)85017-9
132. G. Giallongo, R. Pilot, C. Durante, G.A. Rizzi, R. Signorini, R. Bozio, A. Gennaro, G. Granozzi, Silver nanoparticle arrays on a DVD-derived template: An easy&cheap SERS substrate. Plasmonics **6**, 725–733 (2011). https://doi.org/10.1007/s11468-011-9256-x
133. X.M. Lin, Y. Cui, Y.H. Xu, B. Ren, Z.-Q. Tian, Surface-enhanced raman spectroscopy: Substrate-related issues. Anal. Bioanal. Chem. **394**, 1729–1745 (2009). https://doi.org/10.1007/s00216-009-2761-5
134. K.C. Grabar, R.G. Freeman, M.B. Hommer, M.J. Natan, Preparation and characterization of Au colloid monolayers. Anal. Chem. **67**, 735–743 (1995). https://doi.org/10.1021/ac00100a008
135. R.G. Freeman, K.C. Grabar, K.J. Allison, R.M. Bright, J.A. Davis, A.P. Guthrie, M.B. Hommer, M.A. Jackson, P.C. Smith, D.G. Walter, M.J. Natan, Self-assembled metal colloid monolayers: An approach to SERS substrates. Science **267**, 1629–1632 (1995)
136. K.C. Grabar, P.C. Smith, M.D. Musick, J.A. Davis, D.G. Walter, M.A. Jackson, A.P. Guthrie, M.J. Natan, Kinetic control of interparticle spacing in Au colloid-based surfaces: Rational nanometer-scale architecture. J. Am. Chem. Soc. **118**, 1148–1153 (1996). https://doi.org/10.1021/ja952233+
137. K.R. Brown, M.J. Natan, Hydroxylamine seeding of colloidal Au nanoparticles in solution and on surfaces. Langmuir **14**, 726–728 (1998). https://doi.org/10.1021/la970982u
138. B.-B. Xu, Z.-C. Ma, L. Wang, R. Zhang, L.-G. Niu, Z. Yang, Y.-L. Zhang, W.-H. Zheng, B. Zhao, Y. Xu, Q.-D. Chen, H. Xia, H.-B. Sun, Localized flexible integration of high-efficiency surface enhanced Raman scattering (SERS) monitors into microfluidic channels. Lab Chip **11**, 3347 (2011). https://doi.org/10.1039/c1lc20397e
139. I. Izquierdo-Lorenzo, S. Jradi, P.-M. Adam, Direct laser writing of random Au nanoparticle three-dimensional structures for highly reproducible micro-SERS measurements. RSC Adv. **4**, 4128–4133 (2014). https://doi.org/10.1039/C3RA46220J
140. M.L. Tseng, Y.W. Huang, M.K. Hsiao, H.W. Huang, H.M. Chen, Y.L. Chen, C.H. Chu, N.N. Chu, Y.J. He, C.M. Chang, W.C. Lin, D.W. Huang, H.P. Chiang, R.S. Liu, G. Sun,

D.P. Tsai, Fast fabrication of a Ag nanostructure substrate using the femtosecond laser for broad-band and tunable plasmonic enhancement. ACS Nano **6**, 5190–5197 (2012). https://doi.org/10.1021/nn300947n
141. H. Masuda, K. Fukuda, Ordered metal nanohole arrays made by a two-step replication of honeycomb structures of anodic alumina. Science **268**, 1466 (1995). https://doi.org/10.1126/science.268.5216.1466
142. H.H. Wang, C.Y. Liu, W.S. Bin, N.W. Liu, C.Y. Peng, T.H. Chan, C.F. Hsu, J.K. Wang, Y.L. Wang, Highly raman-enhancing substrates based on silver nanoparticle arrays with tunable sub-10 nm gaps. Adv. Mater. **18**, 491–495 (2006). https://doi.org/10.1002/adma.200501875
143. G. Giallongo, C. Durante, R. Pilot, D. Garoli, R. Bozio, F. Romanato, A. Gennaro, G.A. Rizzi, G. Granozzi, Growth and optical properties of silver nanostructures obtained on connected anodic aluminum oxide templates. Nanotechnology **23**, 325604 (2012). https://doi.org/10.1088/0957-4484/23/32/325604
144. D.H. Jeong, Y.X. Zhang, M. Moskovits, Polarized surface enhanced Raman scattering from aligned silver nanowire rafts. J. Phys. Chem. B **108**, 12724–12728 (2004). https://doi.org/10.1021/jp037973g
145. G. Das, N. Patra, A. Gopalakrishnan, R.P. Zaccaria, A. Toma, S. Thorat, E. Di Fabrizio, A. Diaspro, M. Salerno, Fabrication of large-area ordered and reproducible nanostructures for SERS biosensor application. Analyst **137**, 1785 (2012). https://doi.org/10.1039/c2an16022f
146. C. Toccafondi, R.P. Zaccaria, S. Dante, M. Salerno, Fabrication of gold-coated ultra-thin anodic porous alumina substrates for augmented SERS. Materials (Basel) **9**, 403 (2016). https://doi.org/10.3390/ma9060403
147. C.L. Haynes, R.P. Van Duyne, Nanosphere lithography: A versatile nanofabrication tool for studies of size-dependent nanoparticle optics. J. Phys. Chem. B **105**, 5599–5611 (2001). https://doi.org/10.1021/jp010657m
148. X. Zhang, J. Zhao, A.V. Whitney, J.W. Elam, R.P. Van Duyne, Ultrastable substrates for surface-enhanced Raman spectroscopy: Al_2O_3 overlayers fabricated by atomic layer deposition yield improved anthrax biomarker detection. J. Am. Chem. Soc. **128**, 10304–10309 (2006). https://doi.org/10.1021/JA0638760
149. C.R. Yonzon, D.A. Stuart, X. Zhang, A.D. McFarland, C.L. Haynes, R.P. Van Duyne, Towards advanced chemical and biological nanosensors – An overview. Talanta **67**, 438–448 (2005). https://doi.org/10.1016/j.talanta.2005.06.039
150. L. Baia, M. Baia, J. Popp, S. Astilean, Gold films deposited over regular arrays of polystyrene nanospheres as highly effective SERS substrates from visible to NIR. J. Phys. Chem. B **110**, 23982–23986 (2006). https://doi.org/10.1021/jp064458k
151. C. Forestiere, A.J. Pasquale, A. Capretti, G. Miano, A. Tamburrino, S.Y. Lee, B.M. Reinhard, L. Dal Negro, Genetically engineered plasmonic nanoarrays. Nano Lett. **12**, 2037–2044 (2012). https://doi.org/10.1021/nl300140g
152. Y. Chu, M.G. Banaee, K.B. Crozier, Double-resonance plasmon substrates for surface-enhanced raman scattering with enhancement at excitation and Stokes frequencies. ACS Nano **4**, 2804–2810 (2010). https://doi.org/10.1021/nn901826q
153. B. Yan, A. Thubagere, W.R. Premasiri, L.D. Ziegler, L.D. Negro, B.M. Reinhard, Engineered SERS substrates with multiscale signal enhancement: Nanoparticle cluster arrays. ACS Nano **3**, 1190–1202 (2009). https://doi.org/10.1021/nn800836f
154. F. De Angelis, F. Gentile, F. Mecarini, G. Das, M. Moretti, P. Candeloro, M.L. Coluccio, G. Cojoc, A. Accardo, C. Liberale, R.P. Zaccaria, G. Perozziello, L. Tirinato, A. Toma, G. Cuda, R. Cingolani, E. Di Fabrizio, Breaking the diffusion limit with super-hydrophobic delivery of molecules to plasmonic nanofocusing SERS structures. Nat. Photonics **5**, 682–687 (2011). https://doi.org/10.1038/nphoton.2011.222
155. T. Siegfried, Y. Ekinci, H.H. Solak, O.J.F. Martin, H. Sigg, Fabrication of sub-10 nm gap arrays over large areas for plasmonic sensors. Appl. Phys. Lett. **99**, 263302 (2011). https://doi.org/10.1063/1.3672045
156. Y. Xia, G.M. Whitesides, Soft lithography. Annu. Rev. Mater. Sci. **28**, 153–184 (1998). https://doi.org/10.1146/annurev.matsci.28.1.153

157. D. Qin, Y. Xia, G.M. Whitesides, Soft lithography for micro- and nanoscale patterning. Nat. Protoc. **5**, 491–502 (2010). https://doi.org/10.1038/nprot.2009.234
158. J.A. Rogers, R.G. Nuzzo, Recent progress in soft lithography. Mater. Today **8**, 50–56 (2005). https://doi.org/10.1016/S1369-7021(05)00702-9
159. G.L. Liu, L.P. Lee, Nanowell surface enhanced Raman scattering arrays fabricated by soft-lithography for label-free biomolecular detections in integrated microfluidics. Appl. Phys. Lett. **87**, 74101 (2005). https://doi.org/10.1063/1.2031935
160. M. Cottat, N. Lidgi-Guigui, I. Tijunelyte, G. Barbillon, F. Hamouda, P. Gogol, A. Aassime, J.-M. Lourtioz, B. Bartenlian, M.L. de la Chapelle, Soft UV nanoimprint lithography-designed highly sensitive substrates for SERS detection. Nanoscale Res. Lett. **9**, 623 (2014). https://doi.org/10.1186/1556-276X-9-623
161. S. Picciolini, D. Mehn, C. Morasso, R. Vanna, M. Bedoni, P. Pellacani, G. Marchesini, A. Valsesia, D. Prosperi, C. Tresoldi, F. Ciceri, F. Gramatica, Polymer nanopillar – Gold arrays as surface-enhanced Raman spectroscopy substrate for the simultaneous detection of multiple genes. ACS Nano **8**, 10496–10506 (2014). https://doi.org/10.1021/nn503873d
162. M. Kahraman, P. Daggumati, O. Kurtulus, E. Seker, S. Wachsmann-Hogiu, Fabrication and characterization of flexible and tunable plasmonic nanostructures. Sci. Rep. **3**, 3396 (2013). https://doi.org/10.1038/srep03396
163. A.C. Ferrari, J. Robertson, Interpretation of Raman spectra of disordered and amorphous carbon. Phys. Rev. B **61**, 14095–14107 (2000). https://doi.org/10.1103/PhysRevB.61.14095
164. B.S. Yeo, T. Schmid, W. Zhang, R. Zenobi, A strategy to prevent signal losses, analyte decomposition, and fluctuating carbon contamination bands in surface-enhanced Raman spectroscopy. Appl. Spectrosc. **62**, 708–713 (2008). https://doi.org/10.1366/000370208784658165
165. J. Ramsey, S. Ranganathan, R.L. McCreery, J. Zhao, Performance comparisons of conventional and line-focused surface Raman spectrometers. Appl. Spectrosc. **55**, 767–773 (2001). https://doi.org/10.1366/0003702011952460
166. D. Cialla, S. Pollok, C. Steinbrücker, K. Weber, J. Popp, SERS-based detection of biomolecules. Nano **3**, 383–411 (2014). https://doi.org/10.1515/nanoph-2013-0024
167. J.A. Huang, Y.L. Zhang, H. Ding, H.B. Sun, SERS-enabled lab-on-a-chip systems. Adv. Opt. Mater. **3**, 618–633 (2015). https://doi.org/10.1002/adom.201400534
168. A. Bonifacio, S. Cervo, V. Sergo, Label-free surface-enhanced Raman spectroscopy of biofluids: Fundamental aspects and diagnostic applications. Anal. Bioanal. Chem. **407**, 8265–8277 (2015). https://doi.org/10.1007/s00216-015-8697-z
169. A.S.D.S. Indrasekara, S. Meyers, S. Shubeita, L.C. Feldman, T. Gustafsson, L. Fabris, Gold nanostar substrates for SERS-based chemical sensing in the femtomolar regime. Nanoscale **6**, 8891–8899 (2014). https://doi.org/10.1039/c4nr02513j
170. L. Fabris, M. Schierhorn, M. Moskovits, G.C. Bazan, Aptatag-based multiplexed assay for protein detection by surface-enhanced Raman spectroscopy. Small **6**, 1550–1557 (2010). https://doi.org/10.1002/smll.201000262
171. L. Fabris, SERS tags: The next promising tool for personalized cancer detection? Chem. Nano. Mat. **2**, 249–258 (2016). https://doi.org/10.1002/cnma.201500221
172. N.H. Kim, S.J. Lee, M. Moskovits, Reversible tuning of SERS hot spots with aptamers. Adv. Mater. **23**, 4152–4156 (2011). https://doi.org/10.1002/adma.201101847
173. A. Hakonen, T. Rindzevicius, M.S. Schmidt, P.O. Andersson, L. Juhlin, M. Svedendahl, A. Boisen, M. Käll, Detection of nerve gases using surface-enhanced Raman scattering substrates with high droplet adhesion. Nanoscale **8**, 1305–1308 (2016). https://doi.org/10.1039/c5nr06524k
174. J.Y. Xu, J. Wang, L.T. Kong, G.C. Zheng, Z. Guo, J.H. Liu, SERS detection of explosive agent by macrocyclic compound functionalized triangular gold nanoprisms. J. Raman Spectrosc. **42**, 1728–1735 (2011). https://doi.org/10.1002/jrs.2932
175. A. Hakonen, P.O. Andersson, M. Stenbæk Schmidt, T. Rindzevicius, M. Käll, Explosive and chemical threat detection by surface-enhanced Raman scattering: A review. Anal. Chim. Acta **893**, 1–13 (2015). https://doi.org/10.1016/j.aca.2015.04.010

176. M. Yilmaz, E. Senlik, E. Biskin, M.S. Yavuz, U. Tamer, G. Demirel, Combining 3-D plasmonic gold nanorod arrays with colloidal nanoparticles as a versatile concept for reliable, sensitive, and selective molecular detection by SERS. Phys. Chem. Chem. Phys. **16**, 5563–5570 (2014). https://doi.org/10.1039/c3cp55087g
177. D.-W. Li, W.-L. Zhai, Y.-T. Li, Y.-T. Long, Recent progress in surface enhanced Raman spectroscopy for the detection of environmental pollutants. Microchim. Acta **181**, 23–43 (2014). https://doi.org/10.1007/s00604-013-1115-3
178. P.A. Mosier-Boss, S.H. Lieberman, Detection of nitrate and sulfate anions by normal Raman spectroscopy and SERS of cationic-coated, silver substrates. Appl. Spectrosc. **54**, 1126–1135 (2000). https://doi.org/10.1366/0003702001950922
179. P.A. Mosier-Boss, S.H. Lieberman, Detection of anions by normal Raman spectroscopy and surface-enhanced Raman spectroscopy of cationic-coated substrates. Appl. Spectrosc. **57**, 1129–1137 (2003). https://doi.org/10.1366/00037020360695991
180. B. Gu, J. Tio, W. Wang, Y.-K. Ku, S. Dai, Raman spectroscopic detection for perchlorate at low concentrations. Appl. Spectrosc. **58**, 741–744 (2004). https://doi.org/10.1366/000370204872890
181. A. Eshkeiti, B.B. Narakathu, A.S.G. Reddy, A. Moorthi, M.Z. Atashbar, E. Rebrosova, M. Rebros, M. Joyce, Detection of heavy metal compounds using a novel inkjet printed surface enhanced Raman spectroscopy (SERS) substrate. Sensors Actuators B **171–172**, 705–711 (2012). https://doi.org/10.1016/j.snb.2012.05.060
182. J. Du, J. Cui, C. Jing, Rapid in situ identification of arsenic species using a portable Fe_3O_4@Ag SERS sensor. Chem. Commun. **50**, 347–349 (2014). https://doi.org/10.1039/c3cc46920d
183. W. Ji, Y. Wang, I. Tanabe, X. Han, B. Zhao, Y. Ozaki, Semiconductor-driven "turn-off" surface-enhanced Raman scattering spectroscopy: Application in selective determination of chromium(vi) in water. Chem. Sci. **6**, 342–348 (2015). https://doi.org/10.1039/C4SC02618G
184. S. Dutta, C. Ray, S. Sarkar, M. Pradhan, Y. Negishi, T. Pal, Silver nanoparticle decorated reduced graphene oxide (rGO) nanosheet: A platform for SERS based low-level detection of uranyl ion. ACS Appl. Mater. Interfaces **5**, 8724–8732 (2013). https://doi.org/10.1021/am4025017
185. O. Péron, E. Rinnert, T. Toury, M.L. de la Chapelle, C. Compère, Quantitative SERS sensors for environmental analysis of naphthalene. Analyst **136**, 1018–1022 (2011). https://doi.org/10.1039/c0an00797h
186. M. Mueller, M. Tebbe, D.V. Andreeva, M. Karg, R.A.A. Puebla, N.P. Perez, A. Fery, Platforms for polycyclic aromatic hydrocarbons sensing in gas. Langmuir **28**, 9168–9173 (2012)
187. X. Gu, J.P. Camden, Surface-enhanced Raman spectroscopy-based approach for ultrasensitive and selective detection of hydrazine. Anal. Chem. **87**, 6460–6464 (2015). https://doi.org/10.1021/acs.analchem.5b01566
188. M. Leona, J. Stenger, E. Ferloni, Application of surface-enhanced Raman scattering techniques to the ultrasensitive identification of natural dyes in works of art. J. Raman Spectrosc. **37**, 981–992 (2007). https://doi.org/10.1002/jrs.1582
189. D. Kurouski, S. Zaleski, F. Casadio, R.P. Van Duyne, N.C. Shah, Tip-enhanced Raman spectroscopy (TERS) for in situ identification of indigo and iron gall ink on paper. J. Am. Chem. Soc. **136**, 8677–8684 (2014). https://doi.org/10.1021/ja5027612
190. F. Pozzi, M. Leona, Surface-enhanced Raman spectroscopy in art and archaeology. J. Raman Spectrosc. **47**, 67–77 (2016). https://doi.org/10.1002/jrs.4827
191. F. Casadio, C. Daher, L. Bellot-Gurlet, Raman spectroscopy of cultural heritage materials: Overview of applications and new Frontiers in instrumentation, sampling modalities, and data processing. Top. Curr. Chem. **374**, 62 (2016). https://doi.org/10.1007/s41061-016-0061-z
192. S. Feng, F. Gao, Z. Chen, E. Grant, D.D. Kitts, S. Wang, X. Lu, Determination of α-tocopherol in vegetable oils using a molecularly imprinted polymers-surface-enhanced Raman spectroscopic biosensor. J. Agric. Food Chem. **61**, 10467–10475 (2013). https://doi.org/10.1021/jf4038858

193. B. Peng, G. Li, D. Li, S. Dodson, Q. Zhang, J. Zhang, Y.H. Lee, H.V. Demir, X. Yi Ling, Q. Xiong, Vertically aligned gold nanorod monolayer on arbitrary substrates: Self-assembly and femtomolar detection of food contaminants. ACS Nano **7**, 5993–6000 (2013). https://doi.org/10.1021/nn401685p
194. X. Zhou, F. Zhou, H. Liu, L. Yang, J. Liu, Assembly of polymer-gold nanostructures with high reproducibility into a monolayer film SERS substrate with 5 nm gaps for pesticide trace detection. Analyst **138**, 5832 (2013). https://doi.org/10.1039/c3an00914a
195. X. Wang, Y. Du, H. Zhang, Y. Xu, Y. Pan, T. Wu, H. Hu, Fast enrichment and ultrasensitive in-situ detection of pesticide residues on oranges with surface-enhanced Raman spectroscopy based on Au nanoparticles decorated glycidyl methacrylate-ethylene dimethacrylate material. Food Control **46**, 108–114 (2014). https://doi.org/10.1016/j.foodcont.2014.04.035
196. Y. Zhu, L. Zhang, L. Yang, Designing of the functional paper-based surface-enhanced Raman spectroscopy substrates for colorants detection. Mater. Res. Bull. **63**, 199–204 (2015). https://doi.org/10.1016/j.materresbull.2014.12.004
197. P. Li, R. Dong, Y. Wu, H. Liu, L. Kong, L. Yang, Polystyrene/Ag nanoparticles as dynamic surface-enhanced Raman spectroscopy substrates for sensitive detection of organophosphorus pesticides. Talanta **127**, 269–275 (2014). https://doi.org/10.1016/j.talanta.2014.03.075
198. Y. Zhu, M. Li, D. Yu, L. Yang, A novel paper rag as "D-SERS" substrate for detection of pesticide residues at various peels. Talanta **128**, 117–124 (2014). https://doi.org/10.1016/j.talanta.2014.04.066
199. X. Hu, P. Zheng, G. Meng, Q. Huang, C. Zhu, F. Han, Z. Huang, Z. Li, Z. Wang, N. Wu, An ordered array of hierarchical spheres for surface-enhanced Raman scattering detection of traces of pesticide. Nanotechnology **27**, 384001 (2016). https://doi.org/10.1088/0957-4484/27/38/384001
200. A.S. De Silva Indrasekara, L. Fabris, SERS-based approaches toward genetic profiling. Bioanalysis **7**, 263–278 (2015). https://doi.org/10.4155/bio.14.295
201. L. Fabris, M. Dante, G. Braun, S.J. Lee, M. Moskovits, T.-Q. Nguyen, G.C. Bazan, N.O. Reich, Communication a heterogeneous PNA-based SERS method for DNA detection a heterogeneous PNA-based SERS method for DNA detection. Society **129**, 6086–6087 (2007). https://doi.org/10.1021/ja0705184
202. G. Braun, J.L. Seung, M. Dante, T.Q. Nguyen, M. Moskovits, N. Reich, Surface-enhanced Raman spectroscopy for DNA detection by nanoparticle assembly onto smooth metal films Gary. J. Am. Chem. Soc. **129**, 6378–6379 (2007). https://doi.org/10.1021/ja070514z
203. S. He, K.K. Liu, S. Su, J. Yan, X. Mao, D. Wang, Y. He, L.J. Li, S. Song, C. Fan, Graphene-based high-efficiency surface-enhanced Raman scattering-active platform for sensitive and multiplex DNA detection. Anal. Chem. **84**, 4622–4627 (2012). https://doi.org/10.1021/ac300577d
204. R. Huang, H.T. Yang, L. Cui, W. DY, B. Ren, Z.Q. Tian, Structural and charge sensitivity of surface-enhanced Raman spectroscopy of adenine on silver surface: A quantum chemical study. J. Phys. Chem. C **117**, 23730–23737 (2013). https://doi.org/10.1021/jp407615r
205. J.L. Abell, J.M. Garren, J.D. Driskell, R.A. Tripp, Y. Zhao, Label-free detection of micro-RNA hybridization using surface-enhanced Raman spectroscopy and least-squares analysis. J. Am. Chem. Soc. **134**, 12889–12892 (2012). https://doi.org/10.1021/ja3043432
206. L. Bi, Y. Rao, Q. Tao, J. Dong, T. Su, F. Liu, W. Qian, Fabrication of large-scale gold nanoplate films as highly active SERS substrates for label-free DNA detection. Biosens. Bioelectron. **43**, 193–199 (2013). https://doi.org/10.1016/j.bios.2012.11.029
207. S. Xu, B. Man, S. Jiang, J. Wang, J. Wei, S. Xu, H. Liu, S. Gao, H. Liu, Z. Li, H. Li, H. Qiu, Graphene/Cu nanoparticle hybrids fabricated by chemical vapor deposition as surface-enhanced Raman scattering substrate for label-free detection of adenosine. ACS Appl. Mater. Interfaces **7**, 10977–10987 (2015). https://doi.org/10.1021/acsami.5b02303
208. N. Guarrotxena, B. Liu, L. Fabris, G.C. Bazan, Antitags: Nanostructured tools for developing SERS-based ELISA analogs. Adv. Mater. **22**, 4954–4958 (2010). https://doi.org/10.1002/adma.201002369

209. L. Wu, Z. Wang, K. Fan, S. Zong, Y. Cui, A SERS-assisted 3D barcode Chip for high-throughput biosensing. Small **11**, 2798–2806 (2015). https://doi.org/10.1002/smll.201403474
210. A. Kamińska, E. Witkowska, K. Winkler, I. Dzięcielewski, J.L. Weyher, J. Waluk, Detection of Hepatitis B virus antigen from human blood: SERS immunoassay in a microfluidic system. Biosens. Bioelectron. **66**, 461–467 (2015). https://doi.org/10.1016/j.bios.2014.10.082
211. F. Sun, J.R. Ella-Menye, D.D. Galvan, T. Bai, H.C. Hung, Y.N. Chou, P. Zhang, S. Jiang, Q. Yu, Stealth surface modification of surface-enhanced Raman scattering substrates for sensitive and accurate detection in protein solutions. ACS Nano **9**, 2668–2676 (2015). https://doi.org/10.1021/nn506447k
212. J. Yan, S. Su, S. He, Y. He, B. Zhao, D. Wang, H. Zhang, Q. Huang, S. Song, C. Fan, Nano rolling-circle amplification for enhanced SERS hot spots in protein microarray analysis. Anal. Chem. **84**, 9139–9145 (2012). https://doi.org/10.1021/ac301809e
213. P. Negri, Z.D. Schultz, Online SERS detection of the 20 proteinogenic l-amino acids separated by capillary zone electrophoresis. Analyst **139**, 5989 (2014). https://doi.org/10.1039/c4an01177e
214. M.L. Cheng, B.C. Tsai, J. Yang, Silver nanoparticle-treated filter paper as a highly sensitive surface-enhanced Raman scattering (SERS) substrate for detection of tyrosine in aqueous solution. Anal. Chim. Acta **708**, 89–96 (2011). https://doi.org/10.1016/j.aca.2011.10.013
215. A. Virga, P. Rivolo, E. Descrovi, A. Chiolerio, G. Digregorio, F. Frascella, M. Soster, F. Bussolino, S. Marchiò, F. Geobaldo, F. Giorgis, SERS active Ag nanoparticles in mesoporous silicon: Detection of organic molecules and peptide-antibody assays. J. Raman Spectrosc. **43**, 730–736 (2012). https://doi.org/10.1002/jrs.3086
216. P. Negri, G. Chen, A. Kage, A. Nitsche, D. Naumann, B. Xu, R.A. Dluhy, Direct optical detection of viral nucleoprotein binding to an anti-influenza aptamer. Anal. Chem. **84**, 5501 (2012)
217. Z. Fan, R. Kanchanapally, P.C. Ray, Hybrid graphene oxide based ultrasensitive SERS probe for label-free biosensing. J. Phys. Chem. Lett. **4**, 3813–3818 (2013). https://doi.org/10.1021/jz4020597
218. Y.-Y. Lin, J.-D. Liao, Y.-H. Ju, C.-W. Chang, A.-L. Shiau, Focused ion beam-fabricated Au micro/nanostructures used as a surface enhanced Raman scattering-active substrate for trace detection of molecules and influenza virus. Nanotechnology **22**(18), 185308 (2011). https://doi.org/10.1088/0957-4484/22/18/185308
219. F. Shao, Z. Lu, C. Liu, H. Han, K. Chen, W. Li, Q. He, H. Peng, J. Chen, Hierarchical Nanogaps within bioscaffold arrays as a high- performance SERS substrate for animal virus biosensing. ACS Appl. Mater. Interfaces **6**, 6281–6289 (2014). https://doi.org/10.1021/am4045212
220. K. Chen, H. Han, Z. Luo, Streptococcus suis II immunoassay based on thorny gold nanoparticles and surface enhanced Raman scattering. Analyst **137**, 1259 (2012). https://doi.org/10.1039/c2an15997j
221. T.-Y. Liu, K.-T. Tsai, H.-H. Wang, Y. Chen, Y.-H. Chen, Y.-C. Chao, H.-H. Chang, C.-H. Lin, J.-K. Wang, Y.-L. Wang, Functionalized arrays of Raman-enhancing nanoparticles for capture and culture-free analysis of bacteria in human blood. Nat. Commun. **2**, 538 (2011). https://doi.org/10.1038/ncomms1546
222. A. Sivanesan, E. Witkowska, W. Adamkiewicz, Ł. Dziewit, A. Kamińska, J. Waluk, Nanostructured silver-gold bimetallic SERS substrates for selective identification of bacteria in human blood. Analyst **139**, 1037–1043 (2014). https://doi.org/10.1039/c3an01924a
223. X. Wu, C. Xu, R.A. Tripp, Y. Huang, Y. Zhao, Detection and differentiation of foodborne pathogenic bacteria in mung bean sprouts using field deployable label-free SERS devices. Analyst **138**, 3005 (2013). https://doi.org/10.1039/c3an00186e
224. J. Chen, X. Wu, Y.W. Huang, Y. Zhao, Detection of *E. coli* using SERS active filters with silver nanorod array. Sensors Actuators B **191**, 485–490 (2014). https://doi.org/10.1016/j.snb.2013.10.038

225. C. Fan, Z. Hu, A. Mustapha, M. Lin, Rapid detection of food- and waterborne bacteria using surface-enhanced Raman spectroscopy coupled with silver nanosubstrates. Appl. Microbiol. Biotechnol. **92**, 1053–1061 (2011). https://doi.org/10.1007/s00253-011-3634-3
226. W.R. Premasiri, J.C. Lee, L.D. Ziegler, Surface-enhanced Raman scattering of whole human blood, blood plasma, and red blood cells: Cellular processes and bioanalytical sensing. J. Phys. Chem. B **116**, 9376–9386 (2012). https://doi.org/10.1021/jp304932g
227. F. Gentile, M.L. Coluccio, N. Coppede, F. Mecarini, G. Das, C. Liberale, L. Tirinato, M. Leoncini, G. Perozziello, P. Candeloro, F. De Angelis, E. Di Fabrizio, Superhydrophobic surfaces as smart platforms for the analysis of diluted biological solutions. ACS Appl. Mater. Interfaces **4**, 3213–3224 (2012). https://doi.org/10.1021/am300556w
228. R. Stosch, F. Yaghobian, T. Weimann, R.J. Brown, M.J. Milton, B. Güttler, Lithographical gap-size engineered nanoarrays for surface-enhanced Raman probing of biomarkers. Nanotechnology **22**, 105303 (2011). https://doi.org/10.1088/0957-4484/22/10/105303
229. L. Zhao, J. Blackburn, C.L. Brosseau, Quantitative detection of uric acid by electrochemical-surface enhanced Raman spectroscopy using a multilayered Au/Ag substrate. Anal. Chem. **87**, 441–447 (2015). https://doi.org/10.1021/ac503967s
230. H.-Y. Wu, B.T. Cunningham, Point-of-care detection and real-time monitoring of intravenously delivered drugs via tubing with an integrated SERS sensor. Nanoscale **6**, 5162–5171 (2014). https://doi.org/10.1039/c4nr00027g
231. M. Lee, S. Lee, J.H. Lee, H.W. Lim, G.H. Seong, E.K. Lee, S.I. Chang, C.H. Oh, J. Choo, Highly reproducible immunoassay of cancer markers on a gold-patterned microarray chip using surface-enhanced Raman scattering imaging. Biosens. Bioelectron. **26**, 2135–2141 (2011). https://doi.org/10.1016/j.bios.2010.09.021
232. H.-N. Wang, A. Dhawan, Y. Du, D. Batchelor, D.N. Leonard, V. Misra, T. Vo-Dinh, Molecular sentinel-on-chip for SERS-based biosensing. Phys. Chem. Chem. Phys. **15**, 6008 (2013). https://doi.org/10.1039/c3cp00076a
233. J.H. Granger, M.C. Granger, M.A. Firpo, S.J. Mulvihill, M.D. Porter, Toward development of a surface-enhanced Raman scattering (SERS)-based cancer diagnostic immunoassay panel. Analyst **138**, 410–416 (2013). https://doi.org/10.1039/c2an36128k
234. C. Toccafondi, R. La Rocca, A. Scarpellini, M. Salerno, G. Das, S. Dante, Thin nanoporous alumina-based SERS platform for single cell sensing. Appl. Surf. Sci. **351**, 738–745 (2015). https://doi.org/10.1016/j.apsusc.2015.05.169
235. M. Manikandan, H. Nasser Abdelhamid, A. Talib, H.F. Wu, Facile synthesis of gold nanohexagons on graphene templates in Raman spectroscopy for biosensing cancer and cancer stem cells. Biosens. Bioelectron. **55**, 180–186 (2014). https://doi.org/10.1016/j.bios.2013.11.037
236. G. Zito, G. Rusciano, G. Pesce, A. Dochshanov, A. Sasso, Surface-enhanced Raman imaging of cell membrane by a highly homogeneous and isotropic silver nanostructure. Nanoscale **7**, 8593–8606 (2015). https://doi.org/10.1039/c5nr01341k
237. P. Zhang, R. Zhang, M. Gao, X. Zhang, Novel nitrocellulose membrane substrate for efficient analysis of circulating tumor cells coupled with surface-enhanced Raman scattering imaging. ACS Appl. Mater. Interfaces **6**, 370–376 (2014)
238. C. Lee, R.P. Carney, S. Hazari, Z.J. Smith, A. Knudson, C.S. Robertson, K.S. Lam, S. Wachsmann-Hogiu, 3D plasmonic nanobowl platform for the study of exosomes in solution. Nanoscale **7**, 9290–9297 (2015). https://doi.org/10.1039/c5nr01333j
239. X. Jiang, Z. Jiang, T. Xu, S. Su, Y. Zhong, F. Peng, Y. Su, Y. He, Surface-enhanced Raman scattering-based sensing in vitro: Facile and label-free detection of apoptotic cells at the single-cell level. Anal. Chem. **85**, 2809–2816 (2013). https://doi.org/10.1021/ac303337b
240. S. Yamazoe, M. Naya, M. Shiota, T. Morikawa, A. Kubo, T. Tani, T. Hishiki, T. Horiuchi, M. Suematsu, M. Kajimura, Large-area surface-enhanced Raman spectroscopy imaging of brain ischemia by gold nanoparticles grown on random nanoarrays of transparent boehmite. ACS Nano **8**, 5622–5632 (2014). https://doi.org/10.1021/nn4065692
241. A. Lorén, C. Eliasson, M. Josefson, K.V.G.K. Murty, M. Käll, J. Abrahamsson, K. Abrahamsson, Feasibility of quantitative determination of doxorubicin with surface-enhanced Raman spectroscopy. J. Raman Spectrosc. **32**, 971–974 (2001). https://doi.org/10.1002/jrs.783

242. C. Yuen, W. Zheng, Z. Huang, Low-level detection of anti-cancer drug in blood plasma using microwave-treated gold-polystyrene beads as surface-enhanced Raman scattering substrates. Biosens. Bioelectron. **26**, 580–584 (2010). https://doi.org/10.1016/j.bios.2010.07.030
243. C. Eliasson, A. Lorén, K.V.G.K. Murty, M. Josefson, M. Käll, J. Abrahamsson, K. Abrahamsson, Multivariate evaluation of doxorubicin surface-enhanced Raman spectra. Spectrochim. Acta A Mol. Biomol. Spectrosc. **57**, 1907–1915 (2001). https://doi.org/10.1016/S1386-1425(01)00453-X
244. K.R. Ackermann, T. Henkel, J. Popp, Quantitative online detection of low- concentrated drugs via a SERS microfluidic system. Chem. Phys. Chem. **8**, 2665–2670 (2007). https://doi.org/10.1002/cphc.200700554
245. C. Mc Laughlin, D. Mac Millan, C. Mc Cardle, W.E. Smith, Quantitative analysis of mitoxantrone by surface-enhanced resonance Raman scattering. Anal. Chem. **74**, 3160–3167 (2002)
246. A. Vicario, V. Sergo, G. Toffoli, A. Bonifacio, Surface-enhanced Raman spectroscopy of the anti-cancer drug irinotecan in presence of human serum albumin. Colloids Surf. B Biointerfaces **127**, 41–46 (2015). https://doi.org/10.1016/j.colsurfb.2015.01.023
247. L.F. Sallum, F.L.F. Soares, J.A. Ardila, R.L. Carneiro, Determination of acetylsalicylic acid in commercial tablets by SERS using silver nanoparticle-coated filter paper. Spectrochim. Acta A Mol. Biomol. Spectrosc. **133**, 107–111 (2014). https://doi.org/10.1016/j.saa.2014.04.198
248. R.Y. Mirsafavi, K. Lai, N.D. Kline, A.W. Fountain, C.D. Meinhart, M. Moskovits, Detection of papaverine for the possible identification of illicit opium cultivation. Anal. Chem. (2017). https://doi.org/10.1021/acs.analchem.6b03797
249. W.W. Yu, I.M. White, Inkjet-printed paper-based SERS dipsticks and swabs for trace chemical detection. Analyst **138**, 1020–1025 (2013). https://doi.org/10.1039/c2an36116g
250. Z. Han, H. Liu, J. Meng, L. Yang, J. Liu, J. Liu, Portable kit for identification and detection of drugs in human urine using surface-enhanced Raman spectroscopy. Anal. Chem. **87**, 9500–9506 (2015). https://doi.org/10.1021/acs.analchem.5b02899
251. K.J. Si, P. Guo, Q. Shi, W. Cheng, Self-assembled nanocube-based plasmene nanosheets as soft surface-enhanced Raman scattering substrates toward direct quantitative drug identification on surfaces. Anal. Chem. **87**, 5263–5269 (2015). https://doi.org/10.1021/acs.analchem.5b00328
252. S. Mabbott, A. Eckmann, C. Casiraghi, R. Goodacre, 2p or not 2p: Tuppence-based SERS for the detection of illicit materials. Analyst **138**, 118–122 (2013). https://doi.org/10.1039/c2an35974j
253. Z. Xu, J. Jiang, X. Wang, K. Han, A. Ameen, I. Khan, T.-W. Chang, G.L. Liu, Large-area, uniform and low-cost dual-mode plasmonic naked-eye colorimetry and SERS sensor with handheld Raman spectrometer. Nanoscale **8**, 6162–6172 (2016). https://doi.org/10.1039/C5NR08357E
254. D. Kurouski, R.P. Van Duyne, In situ detection and identification of hair dyes using surface- enhanced Raman spectroscopy (SERS). Anal. Chem. **87**, 2901–2906 (2015). https://doi.org/10.1021/ac504405u
255. A.G. Ryder, Surface enhanced Raman scattering for narcotic detection and applications to chemical biology. Curr. Opin. Chem. Biol. **9**, 489–493 (2005). https://doi.org/10.1016/j.cbpa.2005.07.001
256. C. Muehlethaler, M. Leona, J.R. Lombardi, Review of surface enhanced Raman scattering applications in forensic science. Anal. Chem. **88**, 152–169 (2015). https://doi.org/10.1021/acs.analchem.5b04131
257. R. Dong, S. Weng, L. Yang, J. Liu, Detection and direct readout of drugs in human urine using dynamic surface-enhanced Raman spectroscopy and support vector machines. Anal. Chem. **87**, 2937–2944 (2015). https://doi.org/10.1021/acs.analchem.5b00137
258. N.G. Greeneltch, A.S. Davis, N.A. Valley, F. Casadio, G.C. Schatz, R.P. Van Duyne, N.C. Shah, Near-infrared surface-enhanced raman spectroscopy (NIR-SERS) for the identification of eosin Y: Theoretical calculations and evaluation of two different nanoplasmonic substrates. J. Phys. Chem. A **116**, 11863–11869 (2012). https://doi.org/10.1021/jp3081035

259. M. Gühlke, Z. Heiner, J. Kneipp, Combined near-infrared excited SEHRS and SERS spectra of pH sensors using silver nanostructures. Phys. Chem. Chem. Phys. **17**, 26093–26100 (2015). https://doi.org/10.1039/C5CP03844H
260. N.G. Greeneltch, M.G. Blaber, G.C. Schatz, R.P. Van Duyne, Plasmon-sampled surface-enhanced raman excitation spectroscopy on silver immobilized nanorod assemblies and optimization for near infrared (ex = 1064 nm) studies. J. Phys. Chem. C **117**, 2554–2558 (2013). https://doi.org/10.1021/jp310846j
261. X.Y. Ling, R. Yan, S. Lo, D.T. Hoang, C. Liu, M.A. Fardy, S.B. Khan, A.M. Asiri, S.M. Bawaked, P. Yang, Alumina-coated Ag nanocrystal monolayers as surface enhanced Raman spectroscopy platforms for the direct spectroscopic detection of water splitting reaction intermediates. Nano Res. **7**, 132–143 (2014). https://doi.org/10.1007/s12274-013-0380-0
262. Z.Y. Bao, X. Liu, J. Dai, Y. Wu, Y.H. Tsang, D.Y. Lei, In situ SERS monitoring of photocatalytic organic decomposition using recyclable TiO_2-coated Ag nanowire arrays. Appl. Surf. Sci. **301**, 351–357 (2014). https://doi.org/10.1016/j.apsusc.2014.02.078
263. Q. Cao, R. Che, N. Chen, Facile and rapid growth of Ag_2S microrod arrays as efficient substrates for both SERS detection and photocatalytic degradation of organic dyes. Chem. Commun. **50**, 4931–4933 (2014). https://doi.org/10.1039/c4cc00107a
264. Q. Cao, K. Yuan, Q. Liu, C. Liang, X. Wang, Y.F. Cheng, Q. Li, M. Wang, R. Che, Porous Au-Ag alloy particles inlaid AgCl membranes as versatile Plasmonic catalytic interfaces with simultaneous, in situ SERS monitoring. ACS Appl. Mater. Interfaces **7**, 18491–18500 (2015). https://doi.org/10.1021/acsami.5b04769
265. R. Liu, J.F. Liu, Z.M. Zhang, L.Q. Zhang, J.F. Sun, M.T. Sun, G.B. Jiang, Submonolayer-Pt-coated ultrathin Au nanowires and their self-organized nanoporous film: SERS and catalysis active substrates for operando SERS monitoring of catalytic reactions. J. Phys. Chem. Lett. **5**, 969–975 (2014). https://doi.org/10.1021/jz500238z